CRACKING ON THE UNHEATED SIDE
during
A FIRE IN AN IMMERSED TUNNEL

BEN NIEMAN

MASTER'S THESIS
TU DELFT
AUGUST 2008

Delft University of Technology
Faculty of Civil Engineering and Geosciences

TU Delft

The committee for this master's thesis consisted of:

- Prof.dr.ir. K. van Breugel (professor)
- Dr.ir. P.C.J. Hoogenboom
- Dr.ir. E.A.B. Koenders
- Dr.ir. E. Schlangen
- Prof.dr. Ye G.
- Ir. L.J.M. Houben (coordinator)

The subject of this master's thesis resulted from a project running at Efectis Nederland B.V., and the thesis was largely performed using their facilities. I would like to thank the employees of Efectis Nederland, in particular Kees Both, Arnoud Breunese and George Scholten, for their support and cooperation.

Table of contents

1. Introduction

Immersed tunnels (sometimes called immersed tubes) have been used since the 1910s to connect opposing banks of rivers or large canals. The main aspect of this type of tunnel is that the tunnel segments are built in a dry dock, then transported by river to the tunnel site, where they are sunk into place. In the Netherlands, it is the most frequently used tunnel type, but immersed tunnels are also used in for example the United States, Hong Kong, Australia and the United Kingdom.

There are different ways of constructing an immersed tunnel, the choice of which will depend on local factors. Most American immersed tunnels are round in shape, consisting of a composite steel and reinforced concrete ring, whereas most European immersed tunnels are rectangular in shape, made only of thick reinforced concrete. This thesis will focus on the European type of immersed tunnel.

Like all road constructions, tunnels are prone to accidents that include fire, a particular problem being leaking oil from vehicles. This can cause a rise in temperature of about 1000 ºC in only a few minutes, which may last for several hours. Obviously, this will have a detrimental effect on the tunnel construction, but exactly *how* detrimental is difficult to determine.

In the Netherlands, the need for fire safety engineering with regards to concrete tunnels was first understood in 1978, after the fire in the Velsertunnel. A year later, Rijkswaterstaat (an executive agency of the Dutch Ministry of Transportation and Water Management) published its Rijkswaterstaat curve, describing the temperature-time relation of a fire in a tunnel with oil leaking out of a truck. Its accompanying design method was based on preventing the concrete to reach higher temperatures than 380 ºC by applying fire-resistant plates (in addition to general fire-safety aspects such as providing emergency exits, but these non-construction aspects are not discussed here).

After a fire, structural damage is usually assessed primarily by visual observation. Concrete exposed to temperatures of roughly 300 ºC and higher will turn pink, and since this roughly corresponds to the onset of the main strength loss, the rule of thumb is to look for any pink concrete, remove this by force, and replace it with new concrete (shotcrete). Although in principle valid, this practice ignores the structural damage that may have been done to the rest of the tunnel.

It was not until 2000 that Rijkswaterstaat commissioned a further study into the *repairability* of immersed tunnels after fire, resulting in (TNO, 2004). This study looked into the possibility of permanent damage to the construction in terms of deformations and cracks, which may cause leakage and thereby lead to corrosion of the reinforcement. The report concluded that although deformations may be negligibly small and cracks will not form on the heated side of the tunnel, it is possible that cracks will develop on the *unheated* side of the tunnel, due to thermal incompatibility over the thickness of the wall.

However, the finite element simulation that was used in the TNO study was not detailed enough on this point to definitely confirm or deny this possibility, nor could be predicted whether such cracks, if they would appear, would close during cooling-down or grow further. The notion of cracks developing on the unheated side is, however, an important one, because it can be neither seen nor repaired when assessing damage from the inside of the tunnel. It is possible that tunnels are deemed to be repaired after a fire, while in fact a crack remains open on the unheated side, causing slow corrosion of the reinforcement.

In recent years, however, the focus fire safety engineering has moved in a different direction. Explosive spalling has become a major problem, with concrete mixtures becoming more and more high-grade. When concrete is heated, moisture or water vapour will expand more than the surrounding concrete, and escape through the pores. However, when the permeability is small (as is typically the case in high-grade concretes), the water vapour cannot escape and internal pressure will build. This will eventually lead to an explosive spalling of pieces of the concrete on the heated side.

The solution to this problem is usually found in the application of polypropylene (PP) fibres, which are then mixed through the concrete. These fibres will melt at 160 ºC, creating voids and channels through which water vapour can escape, which alleviates the internal pressure. A lot of recent research into fire safety has concerned itself with the problems of explosive spalling and the working of PP fibres, and a growing number of people seem to think of PP fibres as an alternative to fire-resistant plates.

This has only increased the necessity of further research into the problem of cracking on the unheated side, because unlike fire-resistant plates, the application of PP fibres does not reduce the temperatures in the concrete, which means that the concrete can easily reach temperatures well in excess of 1000 ºC. This also means that the thermal incompatibility between the heated side of a tunnel wall, and the unheated side of the wall, will become much larger, which could cause far larger cracks on the unheated side.

Therefore, this master's thesis will take a more in-depth look at the problem of cracking on the unheated side. The aim of this study is to determine whether this phenomenon is an actual risk, and if so, what parameters influence it. A finite element model of a tunnel cross section has been built in DIANA which calculates the differences in thermal expansion, and the degradation of concrete properties with higher temperatures. In chapter 2, the material model behind this simulation will be described, as well as some general aspects of the finite element method and meshing aspects.

In the following chapter, attempts to further 'zoom in' on a crack to assess its size and depth using the lattice model will be described, as well as the problems regarding the implementation of the lattice model in DIANA. Chapter 4 will concern a number of fire tests that have been performed at Efectis. These tests concern tunnel elements that have been built on a scale 1:10 (i.e. roughly two meters wide and roughly 75 cm high), that have been subjected to a fire.

The crack patterns were then observed and, where possible, crack sizes assessed. Both tunnels with fire-resistant plates and tunnels with PP fibres have been tested (as well as unprotected tunnels for reference). The chapter will describe both the test setup as well as a comparison with the results from the finite element simulation. In chapter 5 a sensitivity analysis will be performed, and in the concluding chapter the main results drawn from this research will be summarised, its implications discussed, and recommendations for further research and programming will be given.

2. The finite element simulation

2.1 Nature of the problem

The phenomenon of cracking on the unheated side is supposedly caused by thermal incompatibility over the thickness of the tunnel wall (or roof). Like most materials, concrete expands upon heating (until it reaches temperatures over 700 ºC, when the shrinkage of the cement becomes so large that no net expansion takes place anymore). However, since the thermal conductivity of concrete is very low (and tunnel walls are relatively thick), the heated side of a tunnel wall can easily reach temperatures well in excess of 700 ºC, while the unheated side can still be 20 or 30 ºC.

This thermal gradient over the thickness causes a huge difference in thermal expansion, which can only be accommodated by the bending of the walls and roof (inwards, so that the heated side can elongate more than the unheated side). This, however, presents a problem for the corners of the structure, which cannot possibly accommodate the inward bending of both walls and roof. The hypothesis is therefore that cracks will develop here in case of a fire.

In order to check whether this is actually the case, and if so, to what extent, and which parameters influence this, a numerical simulation seems the most likely method. In particular, a finite element simulation can be used to model the temperature flow in the cross-section and the resulting strains and stresses. The program DIANA has been chosen for this purpose. In a so-called staggered analysis it performs two consecutive finite element simulations, the first being a heat flow analysis to calculate the temperature field, the second being a structural analysis to calculate the stresses and strains.

Because the focus of this master's thesis is on the phenomenon of cracking on the unheated side during a fire in an immersed tunnel, the material model will be optimised for that purpose, and disregard a number of aspects that pertain to (heated) concrete in general, but are inessential to the problem at hand. In particular, this model will disregard:

- time-dependent effects, such as creep, because the fire only has a limited duration, and such effects are presupposed to be negligible on this time scale
- (explosive) spalling on the heated side (a topic extensively discussed in other publications, that has little bearing on the cracking on the unheated side)
- moisture transport and pore pressure (this is the driving force behind explosive spalling, but since that effect is not considered here, it would be needlessly complicated to include a moisture transport model in the FEM simulation. At the same time, moisture content and transport does have an influence on the material properties and the resulting stresses, but this is implicitly taken into account
- the cooling down phase of a fire. This aspect is beyond the scope of this master's thesis, but nevertheless, the simulation will be set up in such a way that this aspect can easily be added at a later stage. This means that considerations regarding cooling down phase will still dictate a number of aspects of the model, a topic that will be more extensively discussed in section 2.4.2.4.

In the next section, some general concepts of the finite element method will be described first, before the aspect of meshing is discussed. It is, however, not possible to give a comprehensive description of the theory behind the finite element method in this report; interested readers are referred to literature such as (Zienkiewicz & Taylor, 1989; 1991) or (Bathe, 1996), as well as to the DIANA manual (TNO DIANA, 2007).

2.2 General aspects of the finite element method

The finite element method (FEM) is a numerical method for finding solutions to (a system of) differential equations, by discretisation of these equations using so-called shape functions. For linear elastic problems the system of equations can be described as:

$$\boldsymbol{K}\vec{u}=\vec{f}$$

Here, $\boldsymbol{K}$ is the system stiffness matrix, $\vec{u}$ is a vector containing the unknown nodal degrees of freedom (displacements and/or rotations) and $\vec{f}$ is the vector of nodal forces that correspond with the respective degrees of freedom.

The structure (a line, plane or volume) to be analysed is divided into small elements with a finite length (whence the name), bounded by nodes. For each node i, a shape function N_i exists that is equal to unity at that node, and equal to zero at all others. For a one-dimensional bar, the approximated displacement field can then be expressed as:

$$u^h=\sum_{i=1}^{n} N_i \cdot a_i$$

Here, a_i is the nodal degree of freedom under consideration, which in this case would be the displacement in the x-direction. In the more general case, this can be formulated as:

$$u^h=\boldsymbol{N}\vec{u}_e$$

The derivative of this function is the strain field. If $\boldsymbol{B}$ is a matrix that contains the derivatives of the shape functions, this can be expressed as:

$$\vec{\varepsilon}=\boldsymbol{B}\vec{u}_e$$

The relation between stresses and strains can in general be written as:

$$\vec{\sigma}=\boldsymbol{D}(\vec{\varepsilon}-\vec{\varepsilon}_0)+\vec{\sigma}_0$$

Here $\boldsymbol{D}$ represents some stress-strain relation, for example the Young's modulus in Hooke's law. The element nodal displacement vector $\vec{u}_e$ (expressed on the local coordinate system of the element) can be related to the system degrees of freedom (in the global coordinate system), by invoking an element transformation matrix, which shall be denoted $\boldsymbol{T}_e$.

$$\vec{u}_e=\boldsymbol{T}_e\vec{u}$$

For each element, the local equilibrium equation is:

$$\boldsymbol{K}_e\vec{u}_e+\vec{f}_e=\vec{r}_e$$

The subscript e here denotes 'element', so $\boldsymbol{K}_e$ signifies the element stiffness matrix, as opposed to $\boldsymbol{K}$, the system stiffness matrix. The extra vector $\vec{r}$ signifies the internal forces (i.e. those between the elements), which are of course not present in the global formulation. The element stiffness matrix is calculated from:

$$\boldsymbol{K}_e = \int_{V_e} \boldsymbol{B}^T \boldsymbol{D} \boldsymbol{B} \, dV$$

Or rather, if the transformation from a global to the local coordinate system is taken into account:

$$\boldsymbol{K}_e = \boldsymbol{T}^T \left(\int_{V_e} \boldsymbol{B}^T \boldsymbol{D} \boldsymbol{B} \, dV \right) \boldsymbol{T}$$

The right-hand vector $\vec{f}_e$ is calculated from (with the vector $\vec{g}_e$ being the body force per unit area):

$$\vec{f}_e = \int_{V_e} \boldsymbol{N}^T \vec{g}_e \, dV - \int_{V_e} \boldsymbol{B}^T \boldsymbol{D} \vec{\varepsilon}_0 \, dV + \int_{V_e} \boldsymbol{B}^T \vec{\sigma}_0 \, dV$$

The main function of a finite element program is now to assemble the element stiffness matrices into a large system stiffness matrix, and to assemble the global right-hand vector from the element right-hand vectors, so that only the displacements are unknown. In an entirely linear system, the solution can be calculated from inverting the global equation:

$$\vec{u} = \boldsymbol{K}^{-1} \vec{f}$$

However, in a non-linear system, this is not possible, because the matrix $\boldsymbol{K}$ is dependent the current displacement field (i.e. the strain history). In that case, an incremental-iterative solution is needed, which means that problems are not only discrete in space (the finite elements), but also in time (time steps). When incrementing a time step, the finite element program calculates the new external load $\vec{f}_{ext}$. The difference between the external load and the internal load, i.e. the summation of the nodal loads from the previous step, is called the 'out-of-balance force', and denoted by the letter $\vec{g}$.

$$\vec{g} = \vec{f}_{ext} - \vec{f}_{int}$$

Note that all these 'loads' are vectors, because there are components for the different directions (e.g. x and y). From the out-of-balance force, the displacement field is estimated:

$$\delta \vec{u}_i = \boldsymbol{K}_i^{-1} \vec{g}_i$$

The subscript *i* here denotes 'iteration', because these variables can change per iteration. The resulting internal force can then be calculated from:

$$\vec{f}_{int,updated} = \boldsymbol{K} \vec{u}_{total}$$

After which a new out-of-balance force can be calculated:

$$\vec{g}_{updated} = \vec{f}_{ext} - \vec{f}_{int,updated}$$

If the out-of-balance force is smaller than a certain limit $\vec{g}_{max}$, the solution is deemed correct and the simulation can proceed with the next time step. If not, the finite element program will calculate a new iteration by calculating a new displacement field, calculate the resulting internal force, and compare that updated value with the external force, etcetera, until the out-of-balance force has become small enough.

Because $\vec{g}$ is a vector, DIANA actually computes the (Euclidean) norm, and compares it with the norm of the initial out-of-balance force, so that the required accuracy is automatically scaled for the step size. This is convenient, because it means the user can simply give a constant as the required accuracy ratio, without having to estimate the order of magnitude of the values in $\vec{f}$ first.

$$r_f = \frac{\|\vec{g}_i\|}{\|\vec{g}_0\|} \leq r_{f,max}$$

This is called a 'force norm'. An alternative to this is the 'displacement norm', which does not compare the out-of-balance forces but the resulting displacements $\delta\vec{u}_i$, or the 'energy norm', which takes into account both the forces and the displacements (the 'energy' being the area under the curve).

$$r_d = \frac{\|\delta\vec{u}_i\|}{\|\Delta\vec{u}_0\|} \leq r_{d,max}$$

$$r_e = \left\| \frac{\delta\vec{u}_i^T\left(\vec{f}_{int,i+1} + \vec{f}_{int,i}\right)}{\Delta\vec{u}_0^T\left(\vec{f}_{int,1} + \vec{f}_{int,0}\right)} \right\|$$

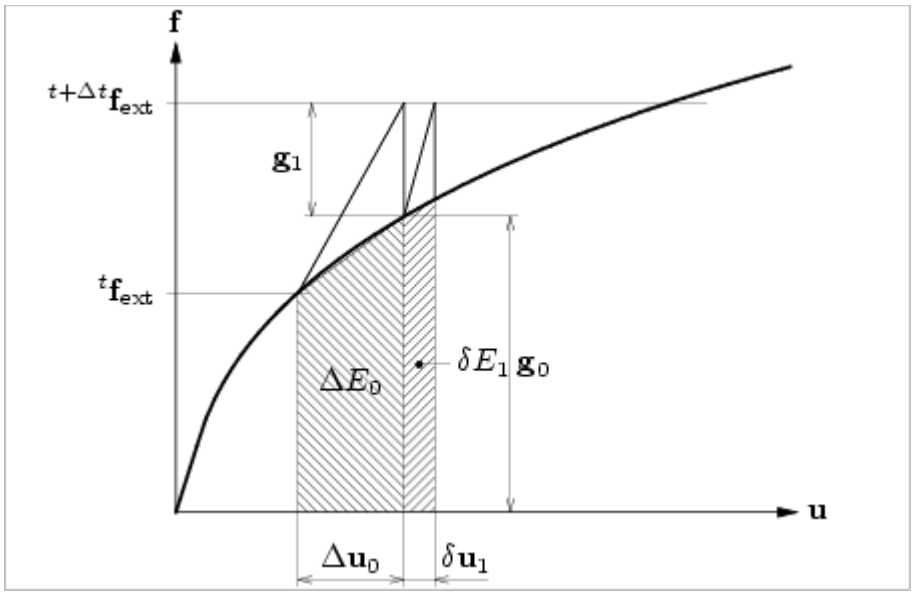

The different norm items; image reproduced from the DIANA manual (TNO DIANA, 2007)

The choice of convergence norm is usually determined by the boundary conditions. In systems where displacements are fixed, the force norm should be used, because this is the critical parameter (whereas the displacement norm would not be too interesting). On the other hand, when a structure can expand freely, the stresses will not be very high, so the force norm is less useful, and displacements should be taken as the critical parameter.

This presents a problem for the analysis at hand, because the external boundary conditions do not play a major role, but the interplay between the displacements (thermal expansion of the concrete) and stresses (restrictions from neighbouring elements) is the critical factor. Therefore, it would not be right to focus on only displacements or stresses, which is the energy norm has been used for all simulations in this thesis.

As a side note, it is also possible to use both the force norm and the displacement norm, but experience shows that this leads to a larger number of required iterations, because the simulation cannot optimise a single function. Also note that both the displacement norm and the energy norm require an extra iteration, because the displacements $\delta\vec{u}_i = \boldsymbol{K}_i^{-1}\vec{g}_i$ have to be calculated from the final out-of-balance force, which makes the simulation somewhat slower.

An aspect that has not yet been discussed is which values to take for $\boldsymbol{K}_i$. The relation between $\vec{u}$ and $\vec{f}$ is typically non-linear (else discretisation in time would not be needed), so the exact value of $\boldsymbol{K}$ is dependent on $\vec{u}$. This poses no problem for the relation $\vec{f}_{int,updated} = \boldsymbol{K}\vec{u}$, but for estimating the displacement field, $\delta\vec{u}_i = \boldsymbol{K}_i^{-1}\vec{g}_i$, there are several options.

The first and simplest option is the linear stiffness method, where the stiffness matrix is only evaluated once, at the start of the first step, and kept constant throughout the entire simulation. This gives estimations of the displacement field that are typically inaccurate, which often leads to a very large number of iterations before the calculation reaches convergence.

The second, more advanced option is Newton-Raphson, which takes the tangential stiffness as K for every iteration. This means that convergence is reached is only a few iterations, but each iteration requires more computation time, because the stiffness matrix has to be calculated again for every iteration. DIANA also supplies some in between options, such as modified Newton-Raphson, which calculates the stiffness matrix once per time step, but keeps it constant over all iterations.

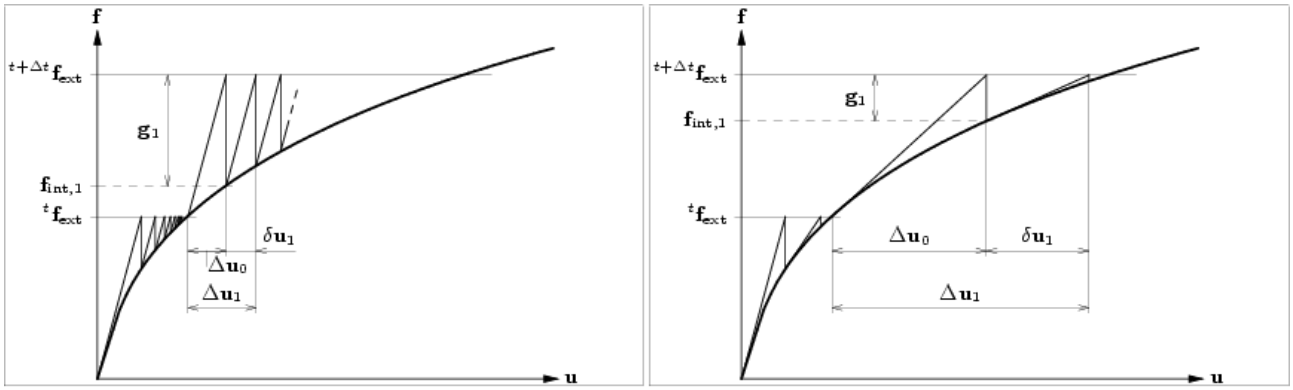

A comparison of the linear stiffness method (left) a and the Newton-Raphson method (right)
Both images are reproduced from the DIANA manual (TNO DIANA, 2007)

In the analyses in this thesis both Newton-Raphson and the linear stiffness model have been used. Especially after the user-supplied material model became more advanced, it took DIANA a lot of time to calculate the stiffness matrix each iteration, so that the linear stiffness method became significantly faster than the Newton-Raphson method, even if it needed 200 to 300 iterations per time step. It is also more robust, since it is not as sensitive to the smoothness of the $\vec{f}$ - $\vec{u}$ relation as Newton-Raphson is (which easily fails if the derivative is not continuous).

The linear stiffness method gets into trouble, however, when the tangential stiffness matrix changes sign, i.e. the $\vec{f}$ - $\vec{u}$ relation becomes negative, as would happen during softening in plasticity, where deformations (and therefore displacements) may increase while the external load decreases. In that case the linear stiffness method only gives good convergence if the the ascending slope is significantly steeper than the descending slope, because it the method cannot take smaller steps. If the descending slope is steeper than the ascending, the linear stiffness method can never find a solution.

The Newton-Raphson method should have no problem with descending slopes in general, but is very sensitive to spurious kinetic modes during the softening phase, as demonstrated by Rots (1988). Also, this iteration mechanism will fail on the transition between ascent and descent if this is not smooth enough, because then the derivatives will not point toward the correct solution. In practice, this will therefore mean that the Newton-Raphson method will in a number of cases also fail at the onset of a descending slope.

Another factor to be reckoned with is that the initial estimation of the displacement field should be close enough to correct solution, especially if the $\vec{f}$ - $\vec{u}$ relation is irregularly shaped (which is most likely the case when plasticity is involved). Because the initial estimation is calculated from the internal force vector of the previous step, this means that no major changes in the system between two time steps may occur. For the first step DIANA estimates the force vector using a simple linear-elastic calculation, which is the reason why it is always necessary to supply some 'dummy-values' such as a Young's modulus, even when these parameters are taken care of by user-supplied subroutines.

Obviously, the initial estimation will be too far off if the step size is too large, but this can be somewhat mitigated by invoking a line search mechanism. This method scales the estimated displacement increment by a factor η , and minimises the energy potential Π in the line search direction.

$$s = \frac{\delta \Pi}{\delta \eta} = \frac{\delta \Pi}{\delta u} \frac{\delta u}{\delta \eta} = 0$$

Because the line search method is only used to 'guide' the global iteration method (Newton-Raphson or linear stiffness) to the proper region on the $\vec{f}$ - $\vec{u}$ curve, the method can be stopped if s is sufficiently close to zero, typically defined as:

$$s \leq \Psi s_0$$

Where s_0 is the initial derivative of the energy potential before the line search method is applied, and Ψ is a constant during the entire simulation. Invoking a line search method aids convergence, but it cannot overcome local extrema, and the simulation will still fail if the initial estimation is too far off.

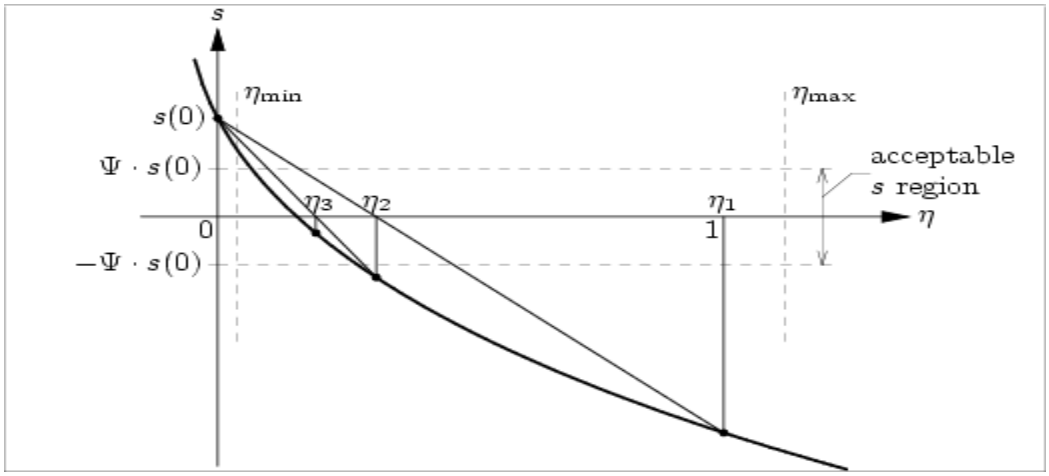

A graphical representation of the line search technique. Image reproduced from the DIANA manual (TNO DIANA, 2007)

Therefore, it can be summarised that in order for the calculation to converge, there are two requirements to the $\vec{f}$ - $\vec{u}$ relation:

1. There should be continuity of the $\vec{f}$ - $\vec{u}$ curve during a time step, with preferably also the derivative function continuous.
2. There should be continuity of the $\vec{f}$ - $\vec{u}$ curve between the time steps, i.e. the position of the curve may not change.

The second point is compensated by the fact that the $\vec{f}$ - $\vec{u}$ curve is only evaluated as discrete intervals in time (i.e. the time steps), which means that *small* changes in the position of the curve are possible. As long as the initial assumption is reasonably close to the actual solution, calculations can continue on the new curve as normal. This is fortunate, because otherwise the temperature dependence of material properties could not have been programmed. Still, continuity within a time step is important, as the solution-finding mechanism (linear stiffness or Newton-Raphson) is dependent on this.

For the thermal analysis roughly the same procedures apply, although with a different main equation:

$$\boldsymbol{K}\,\phi + \boldsymbol{C}\,\dot{\phi} = \boldsymbol{Q}$$

In this equation, $\boldsymbol{K}$ represents the conduction matrix, $\boldsymbol{C}$ is the capacity matrix and $\boldsymbol{Q}$ represents the external flux. The equations are solved using the Newton-Raphson method, with the aid of a line search.

2.3 Meshing aspects

For a structure to be analysed in a finite elements analysis, it needs to be meshed, i.e. subdivided into elements, which involves a number of important decisions. The first, which has actually already been implicitly taken in the previous chapter, is the dimensionality of the model. It is technically possible to analyse a three-dimensional structure in FEM, although it would of course involve longer computation times and a more difficult pre- and post-processing.

The real question, however, is how useful a third dimension would be. Granted, any tunnel fire has a finite length in all three dimensions, and the two-dimensional effect of bending inwards will happen in the third dimension (the length of the tunnel as well). However, in this direction there are no corners impede rotation, but the bending can be accommodated gradually. Therefore the problem of cracking on the unheated side will always be far larger in the width-direction of the tunnel, than in its length-direction of the tunnel.

If the simulation can therefore show that no cracking occurs in the cross section, it can safely be assumed that no cracking will occur over the length either, so a two-dimensional analysis should be sufficient. However, if the simulation shows that the cracking *is* a problem, taking measures against longitudinal cracks is not necessarily sufficient, because there might still be (smaller) perpendicular cracks.

The next important decision is the shape of the elements, which can be either quadrilateral or triangular. To avoid the mesh shape producing a bias for a specific crack shape, triangular elements, randomly distributed using a Delaunay algorithm, have been chosen (see Rots, 1988). This way, all local axes are oriented differently, and all elements are of (slightly) different sizes. From a three-dimensional perspective, plane strain elements would seem to be the logical choice, because there will be no deformations in the third dimension, but stresses will develop. However, after experiencing stability problems with these elements, the choice was made to switch to plane stress elements. Because of the simplifications made in the material model (see section 2.4.2.3), this makes no difference to the end result.

Because the thermal expansion of concrete depends non-linearly on the temperature, the elements in the structural analysis should be of a higher order than those in the thermal analysis. DIANA allows for this in the form of a so-called staggered analysis, which automatically reduces the order of the element for the thermal analysis, and then continues the structural analysis with the full-order element type. For triangular element plane stress elements this pair is called T3HT and CT12M, a three-node and a six-node triangle respectively.

The three-node T3HT uses the following polynomial for the temperature (referred to as potential in DIANA):

$$\phi = a_0 + a_1 \xi + a_2 \eta$$

This polynomial yields a temperature distribution which varies linearly in both directions, and a flux which is constant over the element. Therefore, three integration points are required. Note however that not the temperature field, but only the temperature values in the nodes are used as input for the structural model.

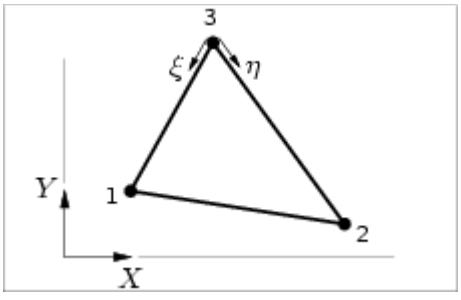

A T3HT element. Image from the DIANA manual (TNO DIANA, 2007)

The six-node CT12M uses the following polynomial for the displacements:

$$u_i = a_0 + a_1\xi + a_2\eta + a_3\xi\eta + a_4\xi^2 + a_5\eta^2$$

This polynomial yields displacements that vary quadratically in both directions, and therefore a linear strain distribution. Three-point Gauss integration is used to calculate this strain field.

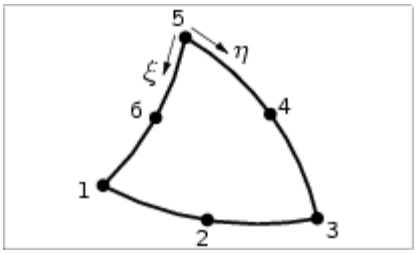

A CT12M element. Image taken from the DIANA manual (TNO DIANA, 2007)

The stress and strain vectors are:

$$\varepsilon = \begin{bmatrix} \varepsilon_{xx} \\ \varepsilon_{yy} \\ \gamma_{xy} \end{bmatrix} \qquad \sigma = \begin{bmatrix} \sigma_{xx} \\ \sigma_{yy} \\ \sigma_{xy} \end{bmatrix}$$

For the reinforcement special 'embedded reinforcement'-elements have been used, which are defined as lines in the pre-processing. DIANA then calculates which (CT12M) the reinforcements intersect, the so-called mother elements, and adds the reinforcement properties to the properties of the mother element. An embedded reinforcement element has no degrees of freedom of its own, instead the displacements are calculated from the strain field in the mother element. The reinforcement lines (bars) are subdivided into elements to match the element distribution of the CT12M's.

The stress and strain vectors are:

$$\varepsilon = \begin{bmatrix} \varepsilon_{\hat{x}\hat{x}} \end{bmatrix} \qquad \sigma = \begin{bmatrix} \sigma_{\hat{x}\hat{x}} \end{bmatrix}$$

Both can vary linearly over the element length ($\hat{x}$ here representing the local bar axis), so two-point Gauss integration is needed for the calculation. The resulting forces are added to the nodal forces of the mother element, and only there taken into account. The downside of this element type is that it automatically assumes a perfect bond between the reinforcement and the mother element; slipping is not facilitated. The mother elements are not reduced in area or weight on account of the reinforcement, and, conversely, reinforcement elements have no weight. The embedded reinforcements are ignored in the thermal analysis, because their area is negligibly small compared to the concrete area, so that the reinforcement will hardly influence heat flow.

The last type of element used is a boundary element (B2HT) for the thermal analysis. It is a two-node line element, applied on the concrete edge. Its division into elements is set to match the T3HT element distribution. Its temperature polynomial is:

$$\phi = a_0 + a_1\xi$$

This means the heat flux over the element (which, by definition, is the flux perpendicular to the element axis, because it is a boundary) can vary linearly along this boundary, so two-point Gauss integration is used. The primary purpose of these boundary elements to is to calculate the concrete surface temperature from the air temperatures in the tunnel. These air temperatures are time dependent, and supplied using a table in an external file.

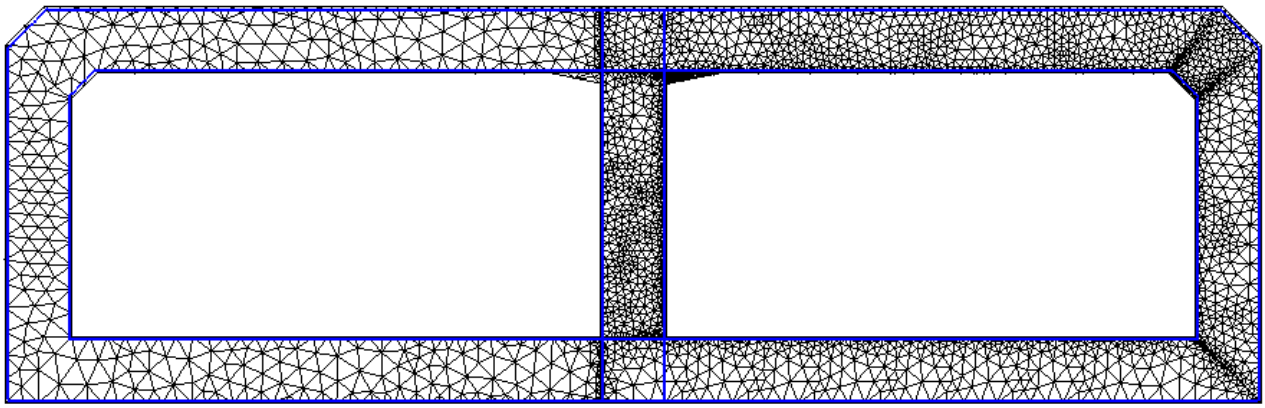

The resulting mesh, with the fire assumed to be in the right hand side tube. The solid lines adjacent to the surfaces represent the embedded reinforcements.

In the picture below the resulting mesh is shown. There is one tube where the fire breaks out (on this and all other pictures in this report, the fire-loaded tube is to be understood to be the one on the right hand side), and an unaffected tube. The large temperature gradient that is to be expected will of course not have a constant slope over the wall thickness. Instead, the gradient will be very high near the fire, and then gently become lower to approach zero near the unheated side of the wall. Because the T3HT elements only support a linear temperature field, the element distribution needs to be sufficiently dense in order to accurately model this phenomenon.

However, it would take far too much computation time to continue this dense distribution throughout the cross section. On the unheated side, the temperature gradient does not vary that much, and larger elements can be used. Around the unaffected tube, temperatures hardly rise, and elements here can be larger still. Hence the skewed element distribution that can be seen in the picture.

Note that even with a very dense mesh, the linear approximation of the temperature curve will still cause temperatures to temporarily drop below the initial value of 20 °C. This temperature dip occurs on the unheated side of the major temperature peak, and because the peak itself reaches temperatures in excess of 1000 °C, values of the dip of about -100 °C should not be seen as extreme. In the material model all temperatures below 20 °C are treated as *being* 20 °C, so the influence on the structural analysis is marginal.

In an actual tunnel the number of tubes may vary depending on its purpose: there may be separate tubes for pedestrians and/or cyclists, for trams or for trains, and in a road tunnel there is typically an emergency tube as well (which is smaller and located in the middle). Yet it is unlikely that the number of unaffected tubes has any influence on the behaviour of the fire-loaded tube, so one unaffected tube should be sufficient for the purpose of this simulation.

2.4 Material model

2.4.1 Thermal analysis

The main equations of the heat flow in the thermal analysis are:

$$q = -k \nabla \phi$$
$$q_v = c_v \dot{\phi}$$

Here, q represents the heat flux, ϕ represents the temperature, k is the conductivity and c_v is the capacitance, i.e. the volumetric specific heat of the concrete. The latter is calculated from:

$$c_v = c_p \rho$$

With c_p designating the specific heat of concrete and ρ representing the density. Both factors change with temperature, and the resulting c_v-T curve is shown below, based on the values in Eurocode 2, part 1-2 (CEN, 2004). The curve has a peak between 100 and 115 °C, representing the evaporation of free water. For this purpose, a moisture content of 3% by weight has been assumed, although it is doubtful whether all water would actually evaporate: it could move to a colder region of the concrete instead, although it is difficult to predict how this would influence the curve.

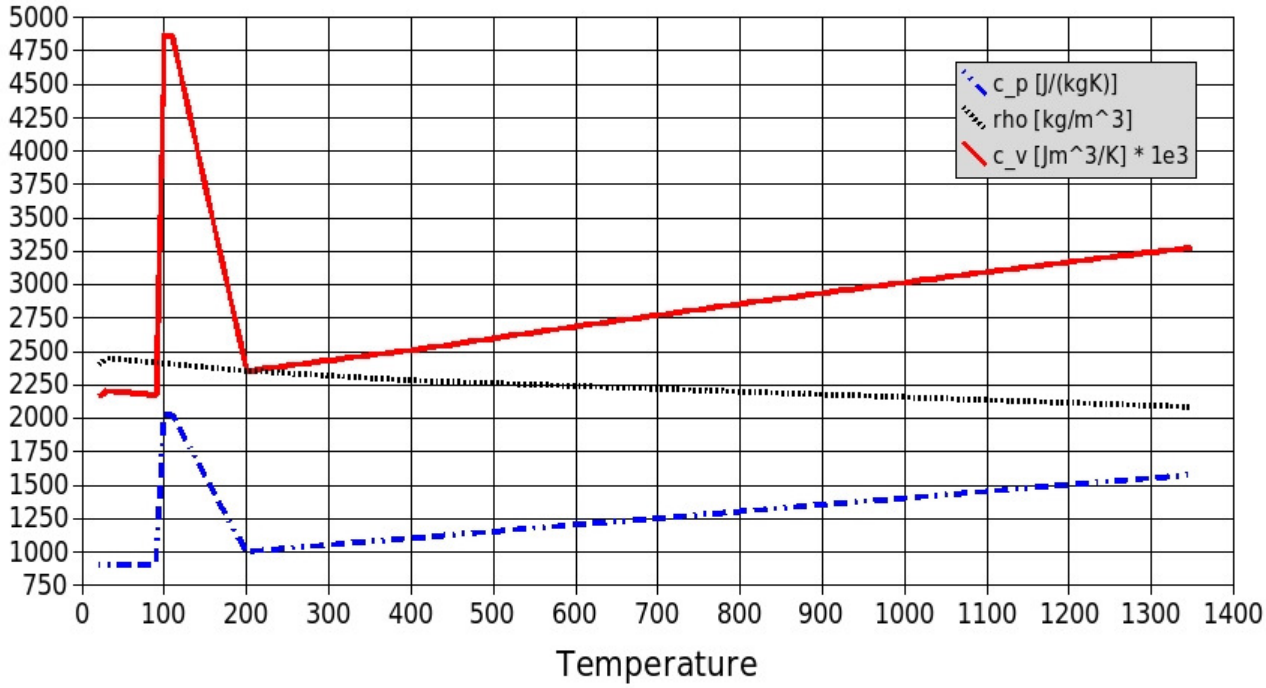

The change in specific heat (dash-dotted line), density (dotted line) and the resulting volumetric specific heat (continuous line) with temperature

The thermal conductivity k is also dependent on the temperature. The Eurocode provides both an upper limit and a lower limit, and for this material model, the exact middle of the two has arbitrarily been chosen. The curve is displayed on the next page.

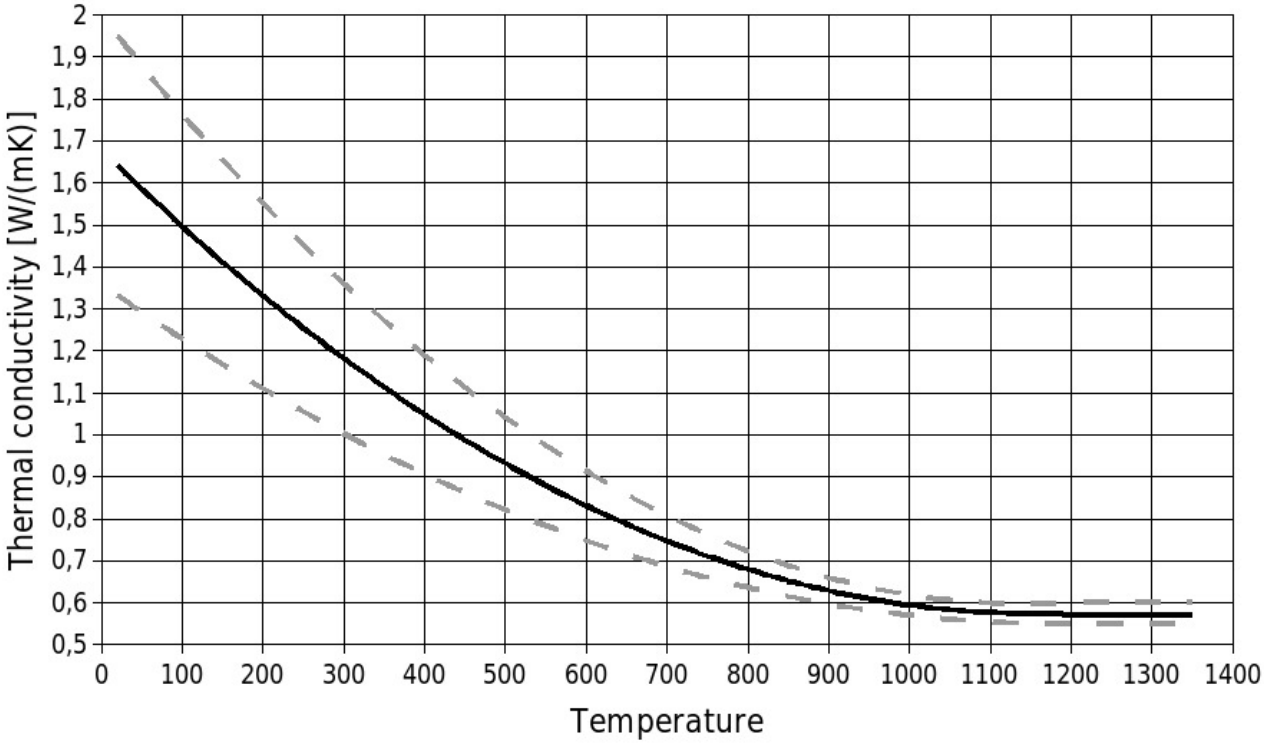

The change of thermal conductivity (continuous line) with temperature, presumed to be the exact mean of the upper and lower limits specified in the Eurocode (dashed lines).

For the boundary elements, a distinction has to be made between convection and radiation. The convective discharge is calculated from:

$$q_c = -k_c(\phi_{surface} - \phi_{external})$$

The radiative discharge is calculated from:

$$q_r = -\varepsilon_r \sigma(\phi^4_{surface} - \phi^4_{external})$$

Here, k_c is the convection factor, taken to be a constant of 25 W/(m^{2}K), ε_r is the emission coefficient, taken to be a constant of 0.7 (dimensionless), and σ is the Stefan-Boltzmann constant, which is equal to 5.67×10^{-8} W/(m^{2}K^4). The values for the convection factor and the emission coefficient are both taken from the Eurocode.

For the external temperatures, the Rijkswaterstaat curve is used, which reaches temperatures of 1350 ºC and lasts for two hours. A visual representation of the curve is given next to this text.

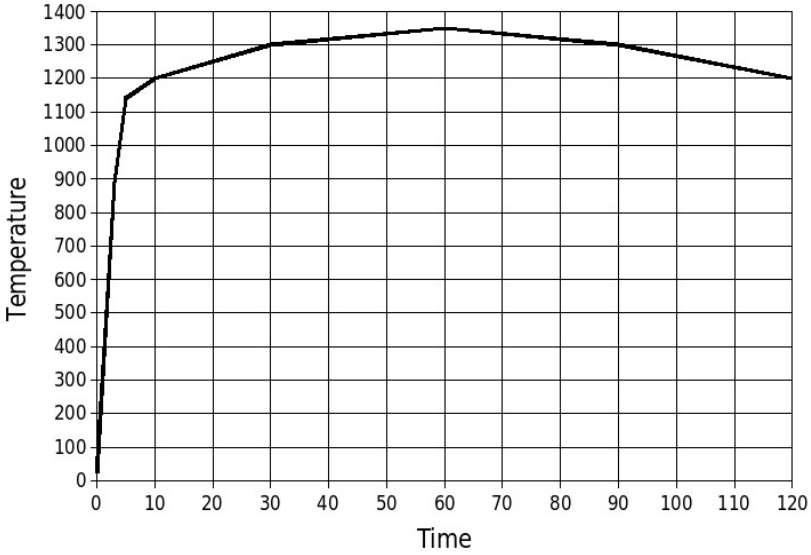

2.4.2 Structural analysis

2.4.2.1 General

DIANA offers several pre-supplied material models, which are in itself often quite advanced, but they give erroneous results when applied in broader context than intended. For example, Anderberg & Thelandersson's (1976) formula for the load induced thermal strain is correctly modelled in DIANA as:

$$\dot{\varepsilon}_{lits} = \alpha k \frac{\sigma}{f_c} \dot{T}$$

Here, ε_{lits} represents the load induced thermal strain (LITS), α is the normal thermal expansion, k is a factor (assumed to be equal to 2), σ is the stress, f_c the strength and T the temperature. Because the stress is negative in compression, this formula gives negative strains for rising temperatures. This is in itself correct, but DIANA also applies the same formula when the material is in tension (producing positive strains) or when the temperature is decreasing (also producing positive strains), neither of which is realistic. This also means that the entire effect becomes reversible, which makes modelling the cooling-down phase not very interesting.

One of the most frustrating aspects of DIANA is the impossibility to change the workings of such formulae. Because some elements will still be warming up during the cooling-down phase, it is not possible to turn the effect off after a certain number of steps. Nor does DIANA offer any possibility to make the parameter k dependent on σ or $\dot{T}$, which also could have solved the problem.

The only option which gives complete freedom is the user-supplied material model (USRMAT), which has the strain vector as input and needs the stress vector as output. The user can construct any relation between the two at will, but at the same time, this means having to build an entire material model from scratch, which, especially for two-dimensional plasticity, is not easy.

Therefore, the focus will be on the essentials in this material model, structuring it in such a way that it can easily be expanded by other people at a later stage. The descriptions in this section will be limited to mathematical formulations and textual elaborations; for those familiar with the Fortran programming language, the actual USRMAT code can be found in appendix A.

For the yield line, a simple Rankine criterion will be assumed for both tension and compression, which means that the two principal directions are independent of each other. As mentioned in chapter 2.3, the strain and stress vectors are of the shape:

$$\vec{\varepsilon} = \begin{bmatrix} \varepsilon_{xx} \\ \varepsilon_{yy} \\ \gamma_{xy} \end{bmatrix} \qquad \vec{\sigma} = \begin{bmatrix} \sigma_{xx} \\ \sigma_{yy} \\ \sigma_{xy} \end{bmatrix}$$

These need to be converted to principal directions:

$$\vec{\varepsilon}_{princ}=\begin{bmatrix}\varepsilon_1\\ \varepsilon_2\end{bmatrix}=\begin{bmatrix}\frac{1}{2}(\varepsilon_{yy}+\varepsilon_{xx}+r)\\ \frac{1}{2}(\varepsilon_{yy}+\varepsilon_{xx}-r)\end{bmatrix} \qquad \vec{\sigma}=\begin{bmatrix}\sigma_{xx}\\ \sigma_{yy}\\ \sigma_{xy}\end{bmatrix}=\begin{bmatrix}\frac{1}{2}(\sigma_1+\sigma_2)-\frac{1}{2}(\sigma_1-\sigma_2)\cos(\theta)\\ \frac{1}{2}(\sigma_1+\sigma_2)+\frac{1}{2}(\sigma_1-\sigma_2)\cos(\theta)\\ \frac{1}{2}(\sigma_1-\sigma_2)\sin(\theta)\end{bmatrix}$$

with $r=\sqrt{(\varepsilon_{yy}-\varepsilon_{xx})^2+\gamma_{xy}^2}$ and $\theta=\arcsin\left(\frac{\gamma_{xy}}{r}\right)$

From the above formulae it follows that ε_1 is the largest of the two principal values, and ε_2 is the smallest. Because compression strains are negative, however, under compression ε_2 is the largest value and ε_1 the smallest. The strains can be decomposed according to the following equation:

$$\vec{\varepsilon}=\vec{\varepsilon}_{thermal}+\vec{\varepsilon}_{mechanical}$$

2.4.2.2 Thermal strains

The thermal component of the strain, $\vec{\varepsilon}_{thermal}$, consists of the thermal expansion and the load induced thermal strain. The normal thermal expansion is calculated according to the Eurocode (for siliceous aggregates):

$$\alpha=9\cdot10^{-6}+0.77\cdot10^{-11}T^2 \quad \text{for } T\le700\,°C$$
$$\alpha=0 \quad \text{for } T>700\,°C$$

These are actually the derivatives of the formulae given in the Eurocode, because those formulae give the total thermal strain compared to the reference length at 20 °C. The load induced thermal strain (LITS), sometimes misleadingly called transient creep, is the effect that a concrete which is under a compressive load during heating undergoes a smaller expansion than what would be expected (according to the above formulae). For larger loads, the result may be a net shrinkage.

This effect was extensively described by Anderberg & Thelandersson (1976), who proposed the following formula, which was already briefly mentioned at the start of this chapter:

$$\dot{\varepsilon}_{lits}=\alpha k\frac{\sigma}{f_c}\dot{T}$$

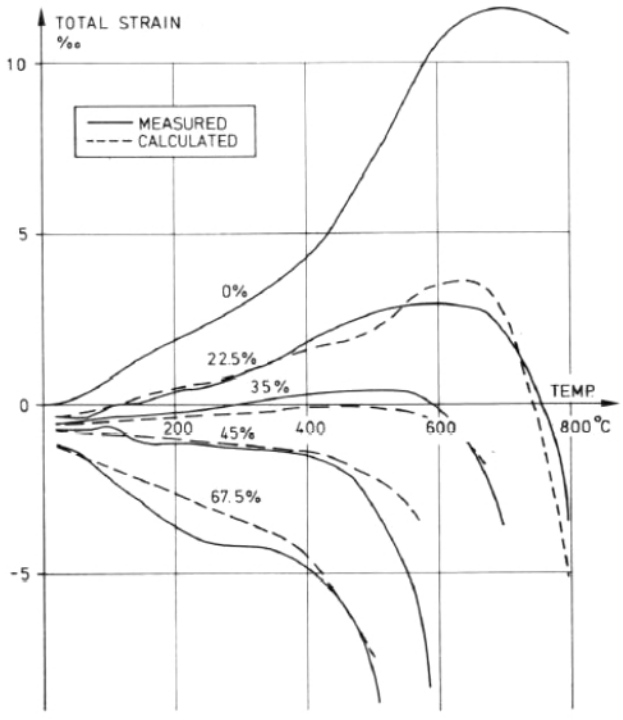

Image reproduced from (Anderberg & Thelandersson, 1976)

The problem when applying this formula, however, is that most experiments on this topic (see for example also Fischer (1967) and Khoury *et al.* (1985; 1986)), have been performed on either heating a pre-loaded concrete, or loading a pre-heated concrete: there seems to be no data for LITS caused by compressive stresses that are, in turn, caused by thermal expansion, which is what is happening on the heated side of the tunnel wall. It is only during heating will large compressive stresses develop here (because the deformations are restricted) and therefore not a true pre-loading, yet the compressive stresses from lower temperatures is already there before the temperature rises further.

Therefore, it seems a reasonable assumption to calculate the change in LITS at every time step based on its current stress level (although note that 'current' here implies the stress level that was calculated the previous step, because the stress vector of the current time step has not yet been calculated). This incremental formulation, however, necessitates the storage of the accumulated thermal strain each step. Because the direction of the principal stresses may change during the process, this means that thermal strains can only be calculated for the global directions, and not for the principal directions.

This in itself would not be a problem, if the formula mentioned above would be valid for every direction. Unfortunately, this formula only describes the behaviour in the direction of principal compression, the stress in the other direction assumed to be zero. Experiments by Ehm (1985), however, show that the unloaded directions develop positive strains in the range of 0.5 to 0.75 times the (negative) strain in the loaded direction. Because the normal thermal expansion still has to be added to these values, the total strain in the unloaded axis can an expansion that is two times as large as the contraction in the loaded axis.

Ehm has also derived a different graphs for the situation where the stress in the secondary axis is not equal to zero, but set to 40% of σ_2 or equal to σ_2, which show quite different strain situations altogether. Unfortunately it is not possible to work these graphs into the material model, because:

1. The three graphs provide too little information to create a full curve, given that the strain situation is clearly non-linear with respect to σ_1, σ_2 and *T*.
2. The graphs define a multi-axial strain situation dependent on a multi-axial stress situation (and temperature), whereas USRMAT requires the calculation of a multi-axial stress state based on a multi-axial strain state and temperature (i.e. the other way round). It is quite possible that the combination of the multi-axial strain state and temperature given as input do not fit the graphs for any stress state.
3. As mentioned before, the accumulated strains need to be stored, which can not be done for the principal directions, because these the angle of these directions may change during the simulation.

The third is actually the least of the problems, because it could be worked around with a few assumptions (either assume that the change in direction of the principal axes is negligibly small, or use linear interpolation between the two accumulated strains of the previous step to calculate the accumulated strain for any new angle), but that is futile as long as the first two problems remain.

Therefore the material model calculates the the thermal strains in the global directions; the mechanical strains (see next section) are then obtained by subtracting these thermal strains from the total strains.

$$\varepsilon_{thermal,i} = \varepsilon_{accumulated} + \alpha \dot{T} \left(1 + k \frac{\sigma_i}{f_c} \right) \qquad \text{if } \sigma_i < 0 \text{ and } \dot{T} > 0$$

$$\varepsilon_{thermal,i} = \varepsilon_{accumulated} + \alpha \dot{T} \qquad \text{if } \sigma_i \geq 0 \text{ or } \dot{T} \leq 0$$

(with *i* representing the directions *xx* and *yy*; for γ_{xy} thermal strains do not apply)

An unrelated problem that has not been addressed yet is the validity for higher temperatures. Anderberg & Thelandersson have only measured up to 800 ºC, and Khoury and Fischer up to 600 ºC. Ehm has heated his specimens up to failure, which in the best case occurred at roughly 800 ºC; his load-controlled tests at constant temperature go up to 750 ºC. Note that f_c represents the strength at 20 ºC, so on increasing temperatures failure might be reached when the nominal load level is still, for example, 0.5.

Above 700 ºC, the shrinkage of the cement becomes so large that the net thermal expansion α becomes roughly zero. At higher temperatures this may also be attributable to the decomposition of the CSH phases (see Schneider, 1982) . If the strain due to LITS is made linearly dependent on α , this means that LITS will also stop above 700 ºC. The graphs by Ehm, however, show that the LITS will start to deviate from this linear relation at roughly 600 ºC, and there is no sign of diminishment between 700 and 800 ºC.

A more practical approach to this problem lies in the realisation that high (nominal) stress levels simply cannot be attained at high temperatures, and would lead to local failure (spalling, which is explicitly not considered in this simulation). Nevertheless, since the strains on the heated side are the driving mechanism behind the studied phenomenon of cracking on the unheated side, misestimation could have an influence on the result (although the thickness of the concrete zone that is exposed to temperatures over 700 ºC is relatively small, and might be too small to change the outcome).

2.4.2.3 Mechanical strains

When the thermal strains are known, the remaining mechanical strains can be computed from:

$$\vec{\varepsilon}_{mechanical} = \vec{\varepsilon} - \vec{\varepsilon}_{thermal}$$

This vector $\vec{\varepsilon}_{mechanical}$ is then converted into the principal directions as described in section 2.4.2.1, after which ε_1 and ε_2 can both be independently subjected to the same stress-strain relation (because no interaction was assumed between the directions). The elastic part of the compressive domain is modelled as a parabola, following the formulation of Anderberg & Thelandersson (1976):

$$\sigma_i = f_{max,c} \frac{\varepsilon_i}{\varepsilon_{max,c}} \left(2 - \frac{\varepsilon_i}{\varepsilon_{max,c}} \right)$$

Here, *i* represents the indices 1 and 2, $f_{max,c}$ is the maximum compressive strength, and $\varepsilon_{max,c}$ is the strain at maximum stress (and therefore not the the maximum strain, because there is also softening). For the tensile domain a completely linear behaviour will be assumed:

$$\sigma_i = E \varepsilon_i$$

Because the tensile part and the compressive part should be connected smoothly, the value of the Young's modulus should be equal to the derivative of the compressive parabola at $\varepsilon_i = 0$; hence:

$$E = 2 \frac{f_{max,c}}{\varepsilon_{max,c}}$$

For softening under compression, a simple linear relation will be assumed. To ensure a smooth connection, the elastic parabola is followed past its peak at $\varepsilon_{max,c}$ to a certain point designated $\varepsilon_{sof,c}$, beyond which the softening starts. The stress at that point is equal to $f_{sof,c}$.

$$\sigma_i = E_{sof}(\varepsilon_i - \varepsilon_{sof,c}) + f_{sof,c}$$

with $\varepsilon_{sof} = \varepsilon_{max,c}\left(1 - \frac{E_{sof}}{E}\right)$ and $f_{sof} = f_{max,c}\left(1 - \frac{E_{sof}^2}{E^2}\right)$

The softening stiffness E_{sof} can essentially be arbitrarily chosen, but it is convenient to express it in terms of the fracture energy G_c, scaled for the element length L_{el} (which, for the triangular elements as described in section 2.3, is taken be equal to the diameter of its circumscribed circle).

$$E_{sof} = \frac{-f_{sof,c}}{\varepsilon_{ult,c} - \varepsilon_{sof,c}}$$

with $\varepsilon_{ult,c} = 2\frac{G_c}{f_{sof,c} L_{el}} + \varepsilon_{sof,c}$

$\varepsilon_{ult,c}$ signifies the point where the stress-strain curve reaches zero, and beyond which the stress will remain zero. To avoid the need for iteration (because $\varepsilon_{sof,c}$ and $f_{sof,c}$ are calculated from E_{sof}, see above), $\varepsilon_{sof,c}$ and $f_{sof,c}$ have been interchanged with $\varepsilon_{ult,c}$ and $f_{ult,c}$ respectively. Because these values are typically very close together, this will not have a notable influence on the derivative.

$$E_{sof} = \frac{-f_{max,c}}{\varepsilon_{ult,c} - \varepsilon_{max,c}}$$

$$\varepsilon_{ult,c} = 2\frac{G_c}{f_{max,c} L_{el}} + \varepsilon_{max,c}$$

For softening in tension, a non-linear relation according to Hordijk (1991) has been used:

$$\frac{\sigma_i}{\sigma_{sof,t}} = \left[1 + \left(c_1 \frac{w}{w_c}\right)^3\right] e^{-c_2 \frac{w}{w_c}} - \frac{w}{w_c}\left(1 + c_1^3\right) e^{-c_2}$$

Here, c_1, c_2 and w_c are model parameters, for which Hordijk advises the values:

$c_1 = 3 \quad c_2 = 6.93 \quad w_c = 160\,\mu m$

In the Hordijk formula, w designates the crack width, but since this model presupposes smeared cracking (that is, the cracks are 'smeared out' over several adjacent elements), in this case w should be seen as a fictitious crack width. These cracks are assumed to rotate with the principal directions (rotating crack model), which means that the angle of the crack does not need be stored. The fictitious crack width relates to the strain as:

$w = (\varepsilon_i - \varepsilon_{sof,t}) L_{el}$

The Hordijk curve starts at a point designated $\varepsilon_{sof,t}$, at which point the stress equals $\sigma_{sof,t}$. These values have to be related to the ascending branch of the tensile domain. As explained in section 2.2, the stress-strain relation needs to be sufficiently smooth to ensure convergence, which cannot be achieved by simply joining a linear elastic branch and a Hordijk curve (which starts with a relatively steep descent) together. Therefore, a small parabola to join the two branches has been added. Theoretically this will increase the fracture energy of an element, but because the area below the parabola is very small compared to the softening branch, this influence is negligible.

The ascending branch will end a point designated ε_{lin}, at which point the stress equals:

$$\sigma_{lin} = E\,\varepsilon_{lin}$$

The parabola should fulfil three requirements:

1. It should start at ε_{lin}, at which point its derivative should be equal to E.
2. Its maximum value should be equal to $\sigma_{max,t}$ (the strain at which point shall be labelled $\varepsilon_{max,t}$)
3. It should end at $\varepsilon_{sof,t}$, at which point its derivative should be equal to the initial derivative of the Hordijk curve.

The derivative of the Hordijk curve at $\varepsilon_i = \varepsilon_{sof,t}$, or $w = 0$, is equal to:

$$E_{hor} = \sigma_{sof,t}\frac{L_{el}}{w_c}\left[-c_2 - \left(1 + c_1^3\right)\right]e^{-c_2}$$

As with E_{sof}, it is desirable to interchange $\sigma_{sof,t}$ with $\sigma_{max,t}$, to avoid having to iterate.

$$E_{hor} = \sigma_{max,t}\frac{L_{el}}{w_c}\left[-c_2 - \left(1 + c_1^3\right)\right]e^{-c_2}$$

The resulting parabola is given by:

$$\sigma_i = \sigma_{max,t} + \left[\frac{-E^2}{4\,p_t\,\sigma_{max,t}}\right]\left(\varepsilon_i - \varepsilon_{max,t}\right)^2$$

with p_t being the relative height of the parabola:

$$p_t = \frac{\sigma_{max,t} - \sigma_{lin}}{\sigma_{max,t}}$$

It is now a matter of choice which of these parameters one wants to make external. To ease comparison with literature when including the temperature dependence $\sigma_{max,t}$ and p_t have been chosen (in addition to the Hordijk parameters c_1, c_2 and w_c), which gives for the internal parameters:

$$\sigma_{lin} = (1 - p_t)\,\sigma_{max,t}$$

$$\varepsilon_{lin} = \frac{\sigma_{lin}}{E}$$

$$\sigma_{sof,t} = \sigma_{max,t} - p_t\,\sigma_{max,t}\frac{E_{hor}^2}{E^2}$$

$$\varepsilon_{sof,t} = \varepsilon_{max,t} - 2\,p_t\,\sigma_{max,t}\frac{E_{hor}}{E^2}$$

$$\varepsilon_{max,t} = \varepsilon_{lin} + 2\,p_t\frac{\sigma_{max,t}}{E}$$

The point at which the Hordijk curve reaches zero is $w = w_c$. Hordijk points out that w_c (the critical crack width) is merely a fitting parameter, and should not be seen as a real value for the actual crack width at which no more stresses can be transmitted (which is likely to be much higher). Nevertheless, it is impractical to take any other approach here than to declare the stresses zero beyond this point.

In terms of strain this point will be designated $\varepsilon_{ult,t}$, with the formula:

$$\varepsilon_{ult,t} = \varepsilon_{sof,t} + \frac{w_c}{L_{el}}$$

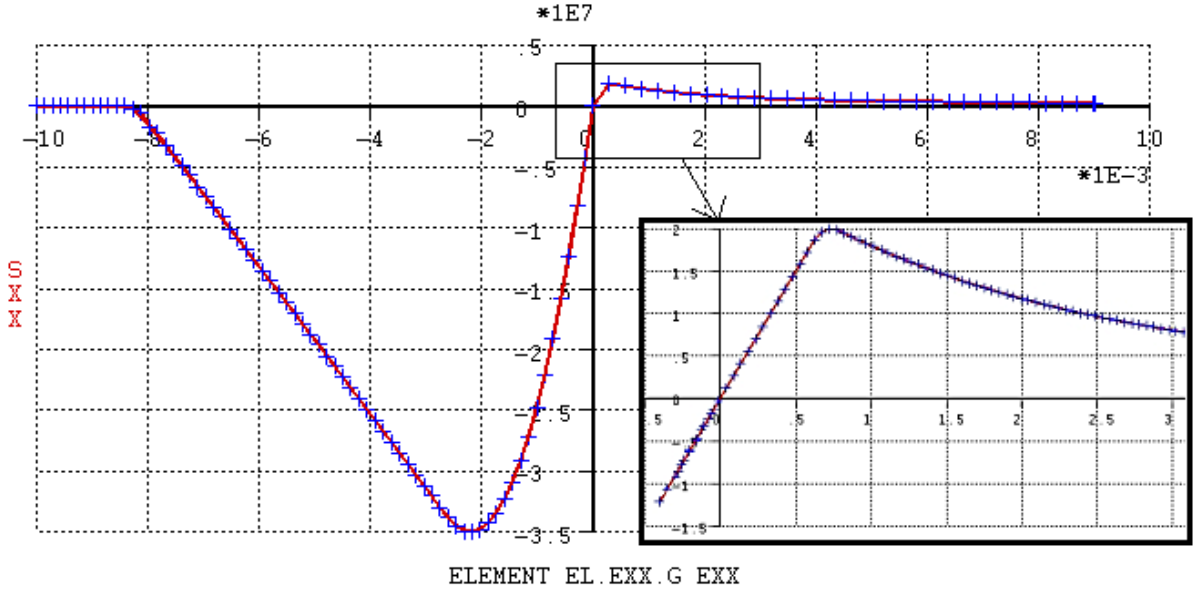

The stress-strain curve used in the material model, with inset of a closeup of the linear elastic tensile domain, showing the continuity between the compressive and the tensile branch, as well as the parabola that joins the linear elastic curve and the Hordijk curve.

The full stress-strain curve is depicted above. For your convenience, below is an overview of the different equations and the regions within which they are used (note that $\varepsilon_i < 0$ for the compression domain).

$\sigma_i = 0$	$\varepsilon_i \le \varepsilon_{ult,c}$
$\sigma_i = E_{sof}(\varepsilon_i - \varepsilon_{sof,c}) + f_{sof,c}$	$\varepsilon_{ult,c} < \varepsilon_i \le \varepsilon_{sof,c}$
$\sigma_i = f_{max,c} \frac{\varepsilon_i}{\varepsilon_{max,c}} \left(2 - \frac{\varepsilon_i}{\varepsilon_{max,c}}\right)$	$\varepsilon_{sof,c} < \varepsilon_i \le 0$
$\sigma_i = E\,\varepsilon_i$	$0 < \varepsilon_i \le \varepsilon_{lin}$
$\sigma_i = \sigma_{max,t} + \left[\frac{-E^2}{4\,p_t\,\sigma_{max,t}}\right](\varepsilon_i - \varepsilon_{max,t})^2$	$\varepsilon_{lin} < \varepsilon_i \le \varepsilon_{sof,t}$
$\sigma_i = \sigma_{sof,t}\left[\left[1 + \left(c_1 \frac{w}{w_c}\right)^3\right] e^{-c_2 \frac{w}{w_c}} - \frac{w}{w_c}\left(1 + c_1^3\right) e^{-c_2}\right]$ with $w = (\varepsilon_i - \varepsilon_{sof,t}) L_{el}$	$\varepsilon_{sof,t} < \varepsilon_i \le \varepsilon_{ult,t}$
$\sigma_i = 0$	$\varepsilon_{ult,t} < \varepsilon_i$

For the regions marked here as $\sigma_i=0$, in fact a very slight descent was programmed with a slope of 1×10^{-12} N/mm^2, because DIANA has immense problems with convergence on completely horizontal sections, especially when Newton-Raphson is used as iterative method (because it uses the derivative to calculate its estimations; see section 2.2).

The external parameters are then:

$\varepsilon_{max,c}$ $\sigma_{max,c}$ $\sigma_{max,t}$ p_t G_c c_1 c_2 w_c

The first four parameters relate to the peak stresses in both compression and tension, and completely define the ascending branches. The last four parameters define the descending slopes. It might appear more logical to take $\varepsilon_{max,t}$ instead of p_t as the fourth parameter, but that would be highly inconvenient, because the top of the parabola should join smoothly to the ascending branch, which is governed by E (an internal parameter calculated from $\varepsilon_{max,c}$ and $\sigma_{max,c}$).

The parabola needs to be sufficiently small compared to the linear elastic branch, which means that there should be certain limitation to $\varepsilon_{max,t}$ compared to E, which is very difficult to estimate, especially when temperature influence is accounted for. Overestimating $\varepsilon_{max,t}$ would lead to an extremely large parabola (and hardly a linear branch), but underestimating would make the system of equations unsolvable (because ε_{lin} would become larger than $\varepsilon_{max,t}$). Therefore, it is preferable to keep p_t a fixed value, for example 0.9, so that $\varepsilon_{max,t}$ automatically scales with E, which scales with $\varepsilon_{max,c}$ and $\sigma_{max,c}$.

The mentioned external parameters can now be made dependent on temperature and on the (nominal) load level, i.e. the ratio between current (compressive) stress and the maximum (compressive) strength at 20 ºC. The concept of load level does not apply to tensile stresses. Because the stress vector of the current step has not been calculated yet, the 'current' stress' is actually the stress vector that was output the previous step. This is then calculated into principal stresses using the angle of the current step size, because this is the angle for which the stress level needs to be calculated. The resulting load level is then:

$$\eta_{i,k}=\frac{-\sigma_{i,k-1}}{\sigma_{max,c,ref}} \qquad \text{for} \quad \sigma_{i,k-1}<0$$

$$\eta_{i,k}=0 \qquad \text{for} \quad \sigma_{i,k-1}\geq 0$$

Here, i represents the principal directions 1 and 2, k is the step number, and *ref* indicates that the reference value (i.e. at 20 ºC) should be taken here.

For the calculation of $\varepsilon_{max,c}$ a formulation developed by Fellinger (2004) based on experiments by Schneider (1982; 1988) has been used:

$$\varepsilon_{max,c}=-1e^{-3}\left[2.2+\frac{T}{140}-\frac{\eta^{0.3}T}{100}\right]$$

Schneider concludes that although aggregate type influences the general shape of the stress-strain relation, the strain at peak stress is nearly independent of it. The same can be said for the type of cement, as well as for the original strength (i.e. at 20 ºC) and water/cement ratio (within the range of 'practical application'). Therefore, it seems safe to 'hard-code' this formula into the material model (making it, strictly speaking, another internal parameter), as opposed to other aspects such as the thermal expansion, which are redirected to a table in DIANA's data file, where material properties can be input per simulation.

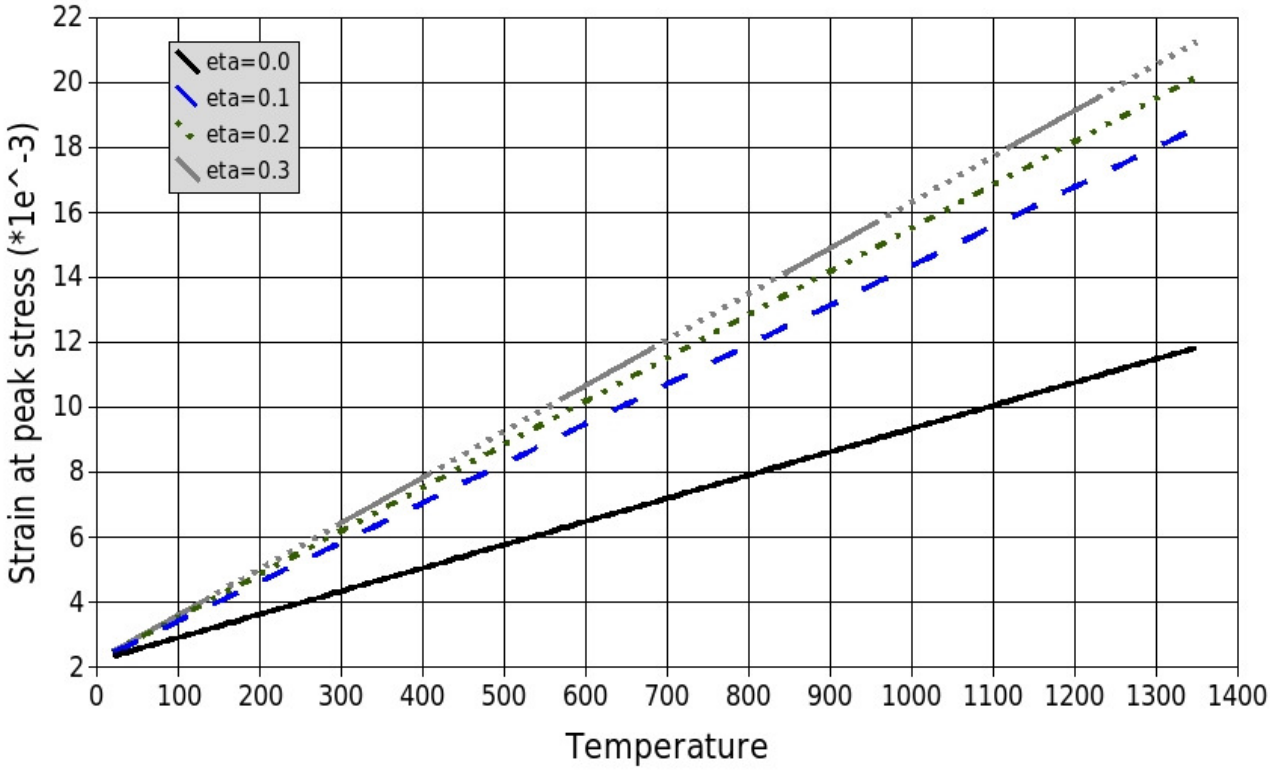

The relationship between temperature and strain at peak (compressive) stress for various load levels.

The formula mentioned on the previous page was based on experiments that reached temperatures up to 700 ºC, and for load levels up to 0.3, so application of the formula outside that range is problematic. As with the load induced thermal strain (see section 2.4.1), data for high temperatures is lacking, yet it is important to correctly estimate the strain development on the heated side (because it is the driving mechanism behind the cracking on the unheated side). It would be best if more research were carried out in this area, but that is beyond the scope of this master's thesis.

Extrapolating the curve to all temperatures is probably the most justifiable solution given the limited data available. Extrapolating the load level, however, is more difficult, because assessing the load level in the first place is problematic. In the above equation, the load level was set equal to the stress level of the previous step, but for a curve at room temperature, the stress level is per definition equal to unity at peak stress. In the quoted experiments, the load level is the stress level during heating, after which the concrete is unloaded, and then re-loaded until failure.

In the intended simulation, however, the temperature increases during the loading, which makes a clear distinction between load level and stress level impossible. During heating, the stress-strain curve changes with every step, and it is clear that the then-present load also has an influence on this change, but is is unclear to what extent. Taking the entire stress level as load level is an upper bound estimation, integration over the temperature domain a lower bound. Since the latter requires extra assumptions to implement, the former has been chosen. For the unheated side this may be a particular overestimation, but since the load level has hardly any influence at temperatures below 100 ºC (see formula), this is not a problem.

The matter of load levels larger than 0.3 (which may still exist in either case) is more difficult. The curve is fitted on only three different load levels (0, 0.1 and 0.3), which makes extrapolation very dangerous. It is, in any case, not likely that the observed trend continues beyond 0.3, because this would lead to extremely small strains at peak stress for high load levels, and in some cases less than zero. The safest solution is therefore to treat any load level higher than 0.3 as if it were equal to 0.3. This also compensates somewhat for the possible over-estimation of the load level as mentioned above. In general, more research is needed in this area.

$$\varepsilon_{max,c,i} = -1e^{-3}\left[2.2 + \frac{T}{140} - \frac{\eta_i^{0.3} T}{100}\right] \quad \text{for} \quad 0 < \eta_i \leq 0.3$$

$$\varepsilon_{max,c,i} = -1e^{-3}\left[2.2 + \frac{T}{140} - \frac{0.3^{0.3} T}{100}\right] \quad \text{for} \quad \eta_i > 0.3$$

Here, *i* denotes the principal directions 1 or 2. Note that internal parameters derived from $\varepsilon_{max,c,i}$, such as E, E_{sof} and $\varepsilon_{max,t}$, can also differ between the two principal directions because of the above. Strictly speaking, they should therefore also be marked with an index *i*, but these subscripts have been omitted from the formulations earlier in this chapter for clarity. Experiments by Ehm (1985) show that the strain at peak stress is also mildly influenced by the load level in the perpendicular direction, but it would be very difficult to implement this (more so because the effect is clearly non-linear, with $\eta_{3-i} = 0.4$ giving higher values than either $\eta_{3-i} = 0$ or $\eta_{3-i} = 1$, regardless of temperature).

The second parameter that should be made dependent on temperature is the maximum compressive stress $\sigma_{max,c}$. Schneider (1982) states that original strength has little influence on the strength-temperature characteristics, so the strength degradation with temperature is best expressed as a relative factor:

$$\sigma_{max,c} = k_c(T)\,\sigma_{max,c,ref}$$

Schneider also concludes that while the maximum stress under load is somewhat higher than the unloaded strength, the height of the stress matters very little. Anderberg & Thelandersson (1976) also concluded that the influence of load level on maximum strength is present but very small compared to the uncertainties inherent to the estimation of high-temperature strength, and they suggest making $\sigma_{max,c}$ a function of temperature only, which is done here.

Graphs by Ehm (1985) show an influence of the stress in the perpendicular direction as well, but this is an effect that is typically well described by a Drucker-Prager yield criterion (see Kupfer & Gerstle, 1973). Since a simplified Rankine criterion has been chosen, this is not accounted for in the current material model. Yet, with the idea of later expansion of the model in mind, it would not be right to introduce an extra parameter for this here, as it is much better described by changing the yield contour.

The actual values of k_c are rather dependent on the type of cement and aggregate, so these will be redirected to a table in the data file, rather than coded it into the material model. The standard values, with which the simulations mentioned in this report have been obtained, were taken from the Eurocode (CEN, 2004), the values being for siliceous aggregates.

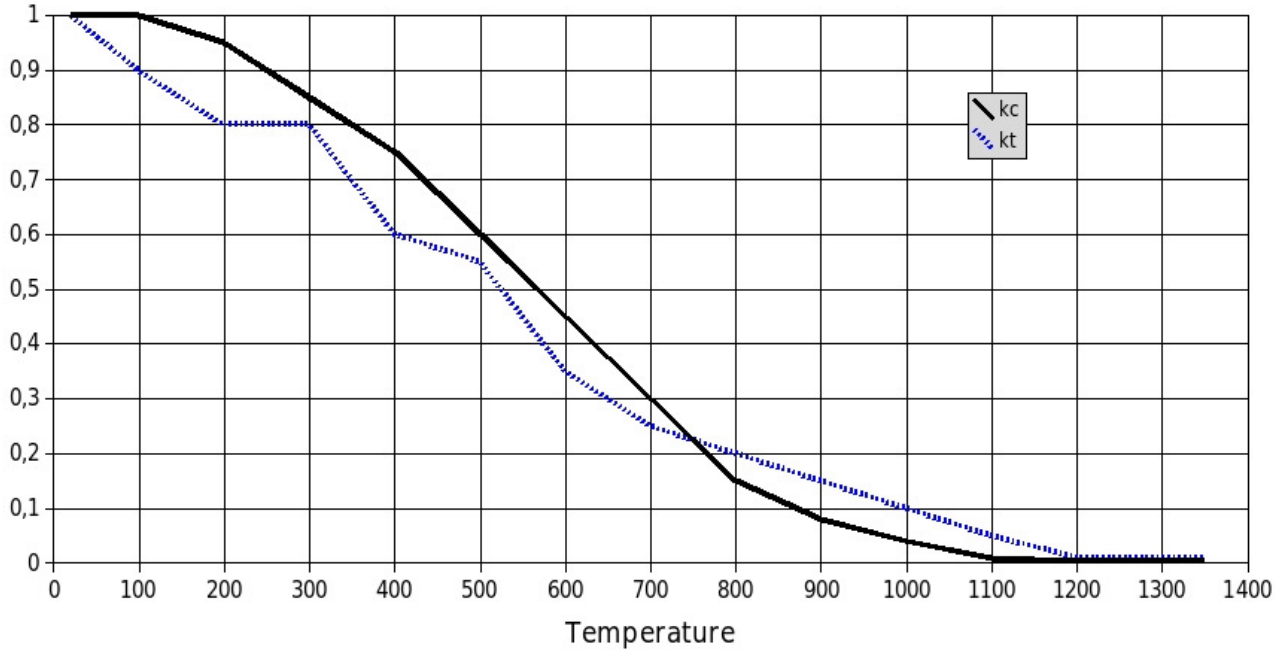

The degradation of compressive (continuous line) and tensile (dotted line) strength with temperature.

Compared to the compressive strength, only a limited amount of data concerning the tensile strength is available, and most test results in this area only refer to the residual strength after cooling the specimens down, in which case a different strengths are obtained. From the little data available, however, it can be clearly seen that the degradation of strength with temperature is more pronounced for tension than for compression.

The Eurocode has simplified this into a linear relation that reaches zero at 600 ºC, but a comparison with experimental results by Thelandersson (1972) show that the steep descent does not continue beyond 600 ºC, at which point there is still 30 to 40 percent of the strength left. Between 600 and 800 ºC, there is only a mild decrease; data for temperatures over 800 ºC is unfortunately lacking. At the same time, Thelandersson points out that the split-cylinder test used to (indirectly) determine the tensile strength seem to overestimate the strength if it has a low magnitude.

The choice of type of aggregate appears to have a large influence, as can be seen from the graphs by Harada (quoted in Schneider, 1982), therefore it is best to redirect this value to a table in the data file. Ignoring a possible influence of the original strength, this value will be reduced to a factor k_t. In the simulations the values from Thelandersson's curve (for siliceous aggregates) have been used as standard values, with extrapolation of the 600 - 800 ºC zone to higher temperatures.

$$\sigma_{max,t} = k_t(T)\,\sigma_{max,t,ref}$$

The next parameter to be considered is the relative height of the parabola p_t. Since data on tensile stress-strain relations at high temperatures is scarce, it is difficult to assess the influence of temperature on it. Based on the little information available, an particular influence of the temperature is not too be expected. Because p_t is expressed as a ratio, σ_{lin} will automatically scale with $\sigma_{max,t}$ and $\varepsilon_{max,t}$ will automatically scale with E when the temperature increases, which is the intended behaviour. The factor p_t can then be made a constant.

The remaining external parameters all concern the softening behaviour. In general, very little is known about temperature influence on the softening behaviour; some researchers (see for example Zhang, 2007) have attempted to relate the fracture energy to the temperature, but the results are conflicting and no clear relations can be indicated. Softening is also very sensitive to the triaxial stress state, as shown by Jamet *et al.* (1984), but for biaxiality this effect is probably less pronounced. Given the convergence problems relating to the softening domain (see section 2.5), it is probably not worthwhile to spend too much time to model these effects accurately.

Therefore, the four softening parameters will be treated as constants, independent of temperature or load level. The resulting softening curves, however, will still be dependent on temperature because they are scaled by $\sigma_{max,t}$ and $\sigma_{max,c}$. The choice of external parameter influences the way in which this scaling takes place. In compression, the fracture energy is the constant, which means that the ultimate strain will increase with rising temperature. In tension, on the other hand, the ultimate strain is a constant, and therefore the fracture energy will decrease with rising temperature. Since neither can be deemed unrealistic, this should not be considered a problem.

For your convenience, below is an overview of the external parameters that should be input in a DIANA data file (where material properties are input per simulation).

Constant material properties	Temperature dependent material properties
• $\sigma_{max,c,ref}$ [force/area] • $\sigma_{max,t,ref}$ [force/area] • c_1 [-] (Hordijk parameter) • c_2 [-] (Hordijk parameter) • w_c [length] (Hordijk parameter) • p_t [-] (parabola height) • G_c [force/area] (compr. fracture energy) • k [-] (LITS parameter)	• $k_c(T)$ [-] • $k_t(T)$ [-] • $\alpha(T)$ [1/temperature]

The table also displays the type of unit per parameter. The actual units (for example, the choice between meters, millimetres or inches) can be made in the data file itself. Input properties for the thermal analysis are not shown in this table. Note that DIANA always needs certain 'dummy' values in its data file (such as the Young's modulus) even if they are not used in the material model. For more information reference is made to the DIANA manual (TNO DIANA, 2007).

After the stresses have been calculated in the principal directions, they can be converted back to the global coordinates.

$$\vec{\sigma}=\begin{bmatrix}\sigma_{xx}\\ \sigma_{yy}\\ \sigma_{xy}\end{bmatrix}=\begin{bmatrix}\frac{1}{2}(\sigma_1+\sigma_2)-\frac{1}{2}(\sigma_1-\sigma_2)\cos(\theta)\\ \frac{1}{2}(\sigma_1+\sigma_2)+\frac{1}{2}(\sigma_1-\sigma_2)\cos(\theta)\\ \frac{1}{2}(\sigma_1-\sigma_2)\sin(\theta)\end{bmatrix}$$

with $\theta=\arcsin\left(\frac{\gamma_{xy}}{r}\right)$ and $r=\sqrt{(\varepsilon_{yy}-\varepsilon_{xx})^2+\gamma_{xy}^2}$

DIANA also requires the user-supplied material model to output the tangent stiffness matrix, which contains the derivatives of the stresses to the strains. This is needed for the iteration mechanism.

$$\boldsymbol{E}_{tangent}=\begin{bmatrix}\frac{\partial\sigma_{xx}}{\partial\varepsilon_{xx}} & \frac{\partial\sigma_{xx}}{\partial\varepsilon_{yy}} & \frac{\partial\sigma_{xx}}{\partial\gamma_{xy}}\\ \frac{\partial\sigma_{yy}}{\partial\varepsilon_{xx}} & \frac{\partial\sigma_{yy}}{\partial\varepsilon_{yy}} & \frac{\partial\sigma_{yy}}{\partial\gamma_{xy}}\\ \frac{\partial\sigma_{xy}}{\partial\varepsilon_{xx}} & \frac{\partial\sigma_{xy}}{\partial\varepsilon_{yy}} & \frac{\partial\sigma_{xy}}{\partial\gamma_{xy}}\end{bmatrix}$$

The required values are obtained using differential calculus, for example:

$$\frac{\partial\sigma_{xx}}{\partial\varepsilon_{xx}}=\frac{\partial\left[\frac{1}{2}(\sigma_1+\sigma_2)-\frac{1}{2}(\sigma_1-\sigma_2)\cos(\theta)\right]}{\partial\varepsilon_{xx}}$$
$$=\frac{1}{2}\left[\frac{\partial\sigma_1}{\partial\varepsilon_{xx}}+\frac{\partial\sigma_2}{\partial\varepsilon_{xx}}\right]-\frac{1}{2}\left[\frac{\partial\sigma_1}{\partial\varepsilon_{xx}}-\frac{\partial\sigma_2}{\partial\varepsilon_{xx}}\right]\cos(\theta)-(\sigma_1-\sigma_2)\frac{\partial\cos(\theta)}{\partial\varepsilon_{xx}}$$

with $\frac{\partial\sigma_1}{\partial\varepsilon_{xx}}=\frac{\partial\sigma_1}{\partial\varepsilon_1}\frac{\partial\varepsilon_1}{\partial\varepsilon_{xx}}$ and $\frac{\partial\sigma_2}{\partial\varepsilon_{xx}}=\frac{\partial\sigma_2}{\partial\varepsilon_2}\frac{\partial\varepsilon_2}{\partial\varepsilon_{xx}}$

Because $\cos(\theta)=\frac{\varepsilon_{yy}-\varepsilon_{xx}}{r}=\frac{\varepsilon_{yy}-\varepsilon_{xx}}{\sqrt{(\varepsilon_{yy}-\varepsilon_{xx})^2+\gamma_{xy}^2}}$, it follows that

$$\frac{\partial\cos(\theta)}{\partial\varepsilon_{xx}}=\frac{-\sqrt{(\varepsilon_{yy}-\varepsilon_{xx})^2+\gamma_{xy}^2}-\frac{(\varepsilon_{yy}-\varepsilon_{xx})(2\varepsilon_{xx}-\varepsilon_{yy})}{2\sqrt{(\varepsilon_{yy}-\varepsilon_{xx})^2+\gamma_{xy}^2}}}{(\varepsilon_{yy}-\varepsilon_{xx})^2+\gamma_{xy}^2}$$

And because $\begin{bmatrix}\varepsilon_1\\ \varepsilon_2\end{bmatrix}=\begin{bmatrix}\frac{1}{2}(\varepsilon_{yy}+\varepsilon_{xx}+r)\\ \frac{1}{2}(\varepsilon_{yy}+\varepsilon_{xx}-r)\end{bmatrix}$, it follows that:

$$\frac{\partial\varepsilon_1}{\partial\varepsilon_{xx}}=\frac{1}{2}+\frac{(2\varepsilon_{xx}-\varepsilon_{yy})}{4\sqrt{(\varepsilon_{yy}-\varepsilon_{xx})^2+\gamma_{xy}^2}}\quad\text{and}\quad\frac{\partial\varepsilon_1}{\partial\varepsilon_{yy}}=\frac{1}{2}-\frac{(2\varepsilon_{yy}-\varepsilon_{xx})}{4\sqrt{(\varepsilon_{yy}-\varepsilon_{xx})^2+\gamma_{xy}^2}}$$

The only remaining unknowns are then $\frac{\partial \sigma_1}{\partial \varepsilon_1}$ and $\frac{\partial \sigma_2}{\partial \varepsilon_2}$. This was only the derivation for $\frac{\partial \sigma_{xx}}{\partial \varepsilon_{xx}}$, but the other eight terms in the tangent stiffness matrix can be expressed in terms of ε_{xx}, ε_{yy}, γ_{xy}, $\frac{\partial \sigma_1}{\partial \varepsilon_1}$ and $\frac{\partial \sigma_2}{\partial \varepsilon_2}$ in the same way. The values for $\frac{\partial \sigma_i}{\partial \varepsilon_i}$ are simply the derivatives of the stress-strain curve, as summarised in the table below.

Stress-strain relation	Derivative	Domain
$\sigma_i = 0$	$\frac{\partial \sigma_i}{\partial \varepsilon_i} = 0$	$\varepsilon_i \leq \varepsilon_{ult,c}$
$\sigma_i = E_{sof}(\varepsilon_i - \varepsilon_{sof,c}) + f_{sof,c}$	$\frac{\partial \sigma_i}{\partial \varepsilon_i} = E_{sof}$	$\varepsilon_{ult,c} < \varepsilon_i \leq \varepsilon_{sof,c}$
$\sigma_i = f_{max,c} \frac{\varepsilon_i}{\varepsilon_{max,c}} \left(2 - \frac{\varepsilon_i}{\varepsilon_{max,c}}\right)$	$\frac{\partial \sigma_i}{\partial \varepsilon_i} = 2 \frac{\sigma_{max,c}}{\varepsilon_{max,c}} \left(1 - \frac{\varepsilon_i}{\varepsilon_{max,c}}\right)$	$\varepsilon_{sof,c} < \varepsilon_i \leq 0$
$\sigma_i = E\, \varepsilon_i$	$\frac{\partial \sigma_i}{\partial \varepsilon_i} = E$	$0 < \varepsilon_i \leq \varepsilon_{lim}$
$\sigma_i = \sigma_{max,t} + \left[\frac{-E^2}{4 p_t \sigma_{max,t}}\right] \left(\varepsilon_i - \varepsilon_{max,t}\right)^2$	$\frac{\partial \sigma_i}{\partial \varepsilon_i} = \frac{-E^2 (\varepsilon_i - \varepsilon_{max,t})}{2 p_t \sigma_{max,t}}$	$\varepsilon_{lim} < \varepsilon_i \leq \varepsilon_{sof,t}$
$\sigma_i = \sigma_{sof,t} \left[\left[1 + \left(c_1 \frac{w}{w_c}\right)^3\right] e^{-c_2 \frac{w}{w_c}} - \frac{w}{w_c}(1 + c_1^3) e^{-c_2}\right]$ with $w = (\varepsilon_i - \varepsilon_{sof,t}) L_{el}$	$\frac{\partial \sigma_i}{\partial \varepsilon_i} = \frac{\sigma_{sof,t}}{w_c} \left[\left(3 - \frac{c_2 w}{w_c}\right) \frac{c_1^3 w^2}{w_c^2} - c_2\right] e^{\frac{-c_2 w}{w_c}} - (1 + c_1^3) e^{-c_2}$	$\varepsilon_{sof,t} < \varepsilon_i \leq \varepsilon_{ult,t}$
$\sigma_i = 0$	$\frac{\partial \sigma_i}{\partial \varepsilon_i} = 0$	$\varepsilon_{ult,t} < \varepsilon_i$

As can be seen in the tangent stiffness matrix, there is no Poisson's ratio in this system. This is not caused by the decision to use a Rankine yield criterion, because the Poisson's ratio is usually applied within the linear elastic region, the common formulation being (with ν designating the Poisson's ratio):

$$\varepsilon_i = \frac{\sigma_i}{E} - \nu \frac{\sigma_{3-i}}{E}$$

This stress-strain relationship does not have a clear distinction between elasticity and plasticity because there is no internal damage parameter (which would be superfluous for Rankine), but, as Feenstra (1993) points out, it would be more realistic to apply the Poisson's ratio throughout the whole stress-strain spectrum anyway. Feenstra also gives pointers on how to do this, but this is difficult to implement.

The biggest problem with the Poisson's ratio, however, is its dependence on stress level. The Poisson's ratio is usually thought of as a constant, but even at room temperature this is only valid for stress levels up to roughly 80% (in the σ_{3-i} direction). For stress levels higher than that, the Poisson's ratio increases to roughly 0.5 at peak stress. As the temperature increases, the stress level at which the ratio starts to deviate from its initial value decreases: at 150 ºC for example, the deviation already starts at a stress level of 50%. At 750 ºC, the Poisson's ratio reaches values of 0.9 at stress levels of less than 20%.

Unfortunately, this effect is non-linear with respect to both temperature and stress level, as can be observed in the graphs by Ehm (1985), but the information is insufficient to derive a non-linear relation for the Poisson's ratio. This means that the Poisson's ratio cannot be properly estimated, and therefore overcoming the technical difficulties regarding its implementation should not be the focus of this master's thesis. However, it should be noted that the Poisson's ratio *is* an important factor, and hopefully this aspect can be added to the material model after further research in a different project.

2.4.2.4 Unloading and the cooling down phase

The cooling down phase is beyond the scope of this master's thesis, but nonetheless some general remarks should be made about this phase, because the material model should be coded in a way to allow for a later addition of this aspect. The warming up phase can be modelled properly without an unloading curve (because no unloading takes place), but in an actual fire there is also a cooling down phase. If corrosion of the reinforcement is taken to be the primary consequence (rather than immediate structural failure), it is important to know whether the cracks will close or widen during the cooling down phase.

When concrete is unloaded hysteresial effects take place, and the original stress-strain relation is no longer followed. This effect takes place as soon as the stress-strain curve starts to deviate from its linear relation (which in compression is almost immediately in the current material model), but of course most noticeable (and important) in the softening regime. This alternate unloading curve should then be modelled explicitly in the material model, so that the stresses do not again increase when the strains are reduced.

The actual unloading curve is highly non-linear and dependent on its point of origin. For unloading in tension Hordijk (1991) has developed the formula:

$$\frac{\sigma_i}{\sigma_{max,t}} = \frac{\sigma_{eu}}{\sigma_{max,t}} + \frac{1}{3\frac{w_{eu}}{w_c} + 0.4}\left[0.014\left[\ln\left(\frac{w}{w_{eu}}\right)\right]^5 - 0.57\sqrt{1-\frac{w}{w_{eu}}}\right]$$

Here, σ_{eu} is the stress that was present when unloading started, and w_{eu} is the crack at that point. Note that this formula produces compressive stresses for values $w > 0$, which is in accordance with test results. Unfortunately, it is rather difficult to work temperature dependence into this formula: if both σ_{eu} and w_{eu} are stored as damage parameters once the unloading starts, the curve is fixed throughout the unloading, even if the main stress-strain relation changes drastically (in case of a temperature increase this might even lead to the unloading curve obtaining higher stresses than the main stress-strain curve).

One possible solution is to take only w_{eu} as the damage parameter, and use the main stress-strain relation to calculate a new σ_{eu} every time step. This would introduce some temperature dependence, but it is very doubtful whether this would even remotely represent the actual influence. After all, the history of the unloading curve is not changed by a temperature change, only its current direction. Note also that σ_{eu} only moves the unloading curve vertically, without affecting the shape. Storing σ_{eu} and calculating w_{eu} would change the shape (as well as its starting point), but in rather drastic way. It is probably not realistic, and also doubtful whether continuity between the time steps could be observed (which is required for convergence - see section 2.2).

Since there is a lack of data regarding the temperature influence on the softening curve, it is probably safest to ignore this influence completely by keeping the Hordijk curve fixed. Another possibility is to take a different curve. An elastic unloading curve takes the Young's modulus and uses that as linear relationship. This agrees well with the initial slope of the non-linear unloading, and it is easy to account for the temperature influence, because the Young's modulus already changes with temperature. As this modifies only the current direction of the unloading curve, and not its history, this is the most correct approach, but still, without test data, one cannot assess how realistic this is.

In the case of fire in the tunnel it is possible that elements that yielded in tension during heating develop compressive stresses during cooling. In this case the elastic unloading curve is problematic, because it deviates significantly from reality, predicting compression at too large crack openings, and overestimating the compressive stresses that occur at a certain strain level.

Yet another option is a secant unloading curve, which simply connects the start point of unloading with the origin. This is the least realistic, but the simplest to apply because it can easily be connected to compression part of the main stress-strain curve. Because of the continuity requirements (see section 2.2), it is always necessary to define a full stress-strain relation, especially if the linear stiffness model is used, whose initial estimations may be severely off. The full curve should then properly 'lead' the iteration mechanism to the correct region. For elastic unloading this can be done by extending the curve to infinite compression, but for the Hordijk curve, this is not possible.

For unloading in compression, no clear mathematical formulation such as the Hordijk formula seems to exist, the general choice being between elastic unloading and secant unloading, or some linear relation in between. Since it is probable that elements that have yielded in compression will not only develop tensile stresses during cooling, but also yield in tension, it is important to attach the existing tension curve of the main stress-strain relation to the unloading curve. This is done most easily when using secant unloading, although horizontally moving the tension curve to match the point where the unloading curve reaches zero strain is also an option.

It should also be realised that when an element starts to yield, neighbouring elements (which were still in the ascending branches of their stress-strain relations) will briefly unload, before reloading again. Then when the next element starts to yield, the neighbouring elements will unload again, before subsequently reloading. This essentially elastic process may repeat itself a number of times, both in compression and in tension. If the unloading curve is modelled to start as soon as the stress-strain relation deviates from a straight line (which is realistic), the reloading branch should also be modelled.

Since this pertains only to small unloadings, the reloading curve can be taken to be equal to the unloading curve (in reality reloading curves have a different shape, see Hordijk (1991), but for small values this will not have an influence). The curve should then smoothly reconnect to the main stress-strain curve, which at constant temperature should be no problem. Temperature changes however, might cause the peak stress to move (both horizontally and vertically) between two steps, which may lead to the reloading curve connecting at a different point, possibly past the peak. This will still create a new peak of course (at the point of connection), but this peak may be too pointed to allow proper convergence.

The above problem can be avoided, however, by assuming the whole pre-peak behaviour to be linear, and only applying unloading to the actual softening. In that case, the reloading curve needs not be programmed, because 'true' reloading will not occur during the fire (at least not with the same sign). The unloading curve can then just be extended towards infinity in the reloading direction, to help convergence (which will only be aided by not having an extra peak).

A bigger problem that will occur if unloading is to be modelled, is that a damage parameter can only be stored for the principal directions (and whichever unloading curve is chosen, at least the fact that unloading is taking place should be stored). However, in the cracks that will emerge on the unheated side, the strain in the direction parallel to the surface will unload while the shear strain remains constant (the strain perpendicular to the surface being close or equal to zero). This means that the principal directions will rotate *because of* the unloading, and eventually swap. Therefore, it is not possible to describe an unloading process using a damage parameter bound to a principal direction.

As a side note, in reality the shear stress in a crack would decrease during crack opening (because cracks cannot transmit shear stresses), which would also cause the shear strains to decrease (and the shear force would be transmitted by a smaller remaining cross section). If the crack subsequently closes, the shear strains and stresses would increase again. This effect is currently not implemented in the model, but if it had been, the principal directions would still rotate because of the unloading (only a decrease of the shear strain could prevent this).

Besides unloading, there are a number of different hysteresial effects that need to be considered to properly simulate the cooling down phase. In the material model thermal expansion and material degradation was described as dependent on temperature, but this is only valid for the warming up phase; for cooling down these effects cannot simply be assumed to be fully reversible.

Fischer (1967) has performed extensive measurements on concrete during heating and cooling. His graphs show that (for siliceous concretes) the thermal contraction is somewhat less than its corresponding thermal expansion, especially for the lower temperatures, resulting in a remaining positive strain after the temperature has returned to its initial value. There may be a time effect involved here as well, since the graphs also show an ongoing thermal expansion when the temperature is kept constant. The cooling down curve may be different if such a period of constant temperature is not present in between, or when the cooling is done more rapidly than in Fischer's tests.

At the same time, there seems to be no influence of the load level at all: the thermal contraction appears to be a constant regardless of the amount of load induced thermal strain that was built up during heating. This means for high load levels that contraction will take place during heating and during cooling, resulting in very large compressive strains. It is vital that this is modelled correctly in the material model, if the cooling down phase is to be simulated.

Interestingly, Bažant *et al.* (2004) conclude that load induced thermal strain *does* apply to the cooling down phase, but with an opposite sign (i.e. it is an additional contraction, not an expansion to counter the thermal contraction), which is clearly incompliant with the graphs by Fischer. However, in a different publication, Bažant and Chern (1987) equate the transitional thermal creep to the normal drying creep, coupling the creep on cooling to the increase of the moisture content. This suggests that the observed difference in conclusion might be caused by the different time scales observed: the moisture content might not have increased again during the cooling phase in Fischer's tests.

While it seems reasonable to presume a fixed moisture content decrease with increasing temperatures, this is not so easy for the cooling down phase, as the moisture has migrated through the cross section. Clearly, it would be easiest to assume no influence of the moisture level and follow Fischer's graphs, yet it would be more correct to at least assess the time scale of the return of the moisture content compared to the time scale of cooling down after a fire. Only if the time scale of the moisture content is clearly larger than the duration of the cooling, can this effect be safely ignored.

No data appears to exist for cooling from temperatures above 600 ºC. Since above these temperatures concrete deteriorates quickly, it is doubtful whether the thermal contraction would be the same if even higher temperatures have been reached. It is possible that the thermal strains would then become completely irreversible, but on the other hand the deterioration might also be (partly) reversible; it is likely that the rate of cooling plays a dominant role here.

With regards to the stress-strain relation it should be noted that multiple researchers, such as Malhotra (1956), Fischer (1967) and Khoury (1986), have observed that the compressive strength after cooling is lower than the compressive strength at high temperatures. In the graphs by Fischer, the difference is more pronounced if higher temperatures have been reached, with as much as 25% of the high temperature strength being lost during cooling. Malhotra, on the other hand, finds a more or less constant loss of 20% regardless of the temperature reached. Khoury concludes that the strength reduction is less when the concrete is under compressive load during cooling, something that can also be seen in Fischer's graphs.

Fischer has also derived stress-strain relations for concretes after cooling, although he has only measured up to a limited strain level. From these graphs it would appear that, for lower temperatures, the strain at peak stress is reduced on cooling (implying some reversibility), but the same cannot be said for higher temperatures, where the strain appears to be either constant or, possibly, to increase. Further (strain rate controlled) measurements would be required to analyse this phenomenon more accurately.

From results by Thelandersson (1972) it can be determined that the tensile strength also decreases during the cooling down phase if temperatures over roughly 350 ºC have been reached, but that some reversibility exists if the temperature has remained below that level. Both effects are, however, very small compared to the major strength loss under compression.

The hysteresial effects of the cooling down phase could be modelled by introducing an additional parameter T_{max}, which would represent the highest temperature reached by an element. If the initial dip below 20 ºC is ignored (which it should be), any element will have only one warming up phase and one subsequent cooling down phase. Throughout the warming up phase, the material properties and thermal strains could be calculated as in section 2.4.2.3; in the cooling down phase, on the other hand, the material properties and thermal strains can be calculated from a combination of T and T_{max}. The primary difficulty that remains, however, is to find mathematical expressions for the observed effects.

2.4.2.5 Reinforcing steel

The previous sections all concerned the material properties of the concrete, but of course there is reinforcing steel as well. As mentioned in section 2.3, the reinforcement is ignored in the thermal analysis, but it plays an important role in the structural analysis. Like concrete, the reinforcing steel has thermal strains and mechanical strains, the only difference being that in this case the strains are not vectors, but scalar values.

$$\varepsilon = \varepsilon_{thermal} + \varepsilon_{mechanical}$$

Because the concept of LITS does not apply to reinforcing steel, the thermal strain is simply calculated from:

$$\dot{\varepsilon}_{thermal} = \alpha \dot{T}$$

The thermal expansion α is temperature dependent; the formulation is taken from the Eurocode.

$\alpha = 1.2 \cdot 10^{-5} + 0.8 \cdot 10^{-8} T$	for $T \leq 750\,°C$
$\alpha = 0$	for $750\,°C < T \leq 860\,°C$
$\alpha = 2 \cdot 10^{-5}$	for $T > 860\,°C$

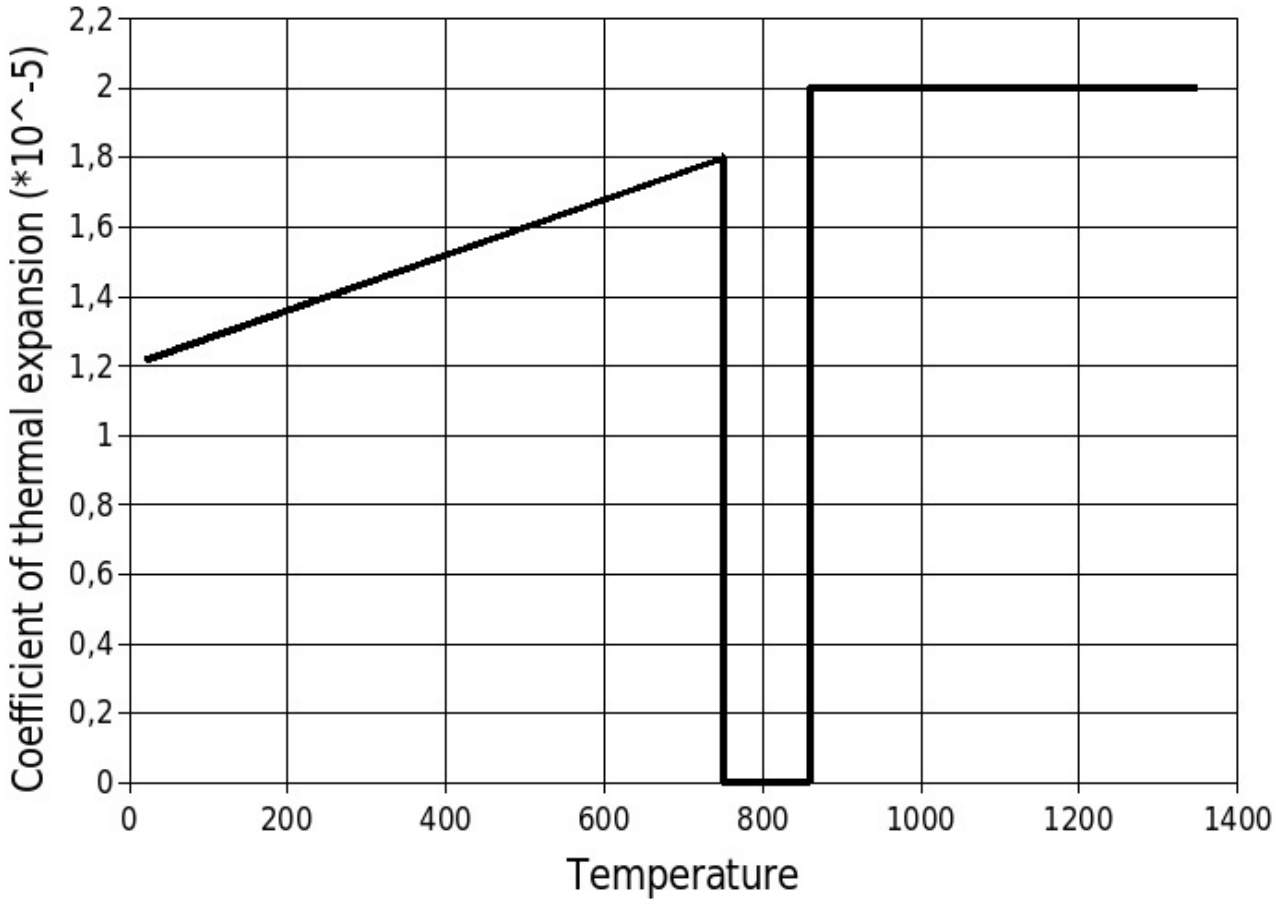

The stress-strain relation is also taken from the Eurocode, although the softening part has been omitted, and ideal plasticity has been assumed instead (i.e. $\varepsilon_{st}=\infty$)

Stress-strain relation	**Derivative**	**Domain**
$\sigma=E\,\varepsilon$	$\frac{\sigma}{\varepsilon}=E$	$0<\varepsilon\leq\varepsilon_{sp}$
$\sigma=\sigma_{sp}-c+\frac{b}{a}\sqrt{a^2-(\varepsilon_{sy}-\varepsilon)^2}$	$\frac{\sigma}{\varepsilon}=\frac{b(\varepsilon_{sy}-\varepsilon)}{a\sqrt{a^2-(\varepsilon-\varepsilon_{sy})^2}}$	$\varepsilon_{sp}<\varepsilon\leq\varepsilon_{sy}$
$\sigma=\sigma_{sy}$	$\frac{\sigma}{\varepsilon}=0$	$\varepsilon_{sy}>\varepsilon$

With the following functions:

$$a^2=(\varepsilon_{sy}-\varepsilon_{sp})\left(\varepsilon_{sy}-\varepsilon_{sp}+\frac{c}{E}\right)$$

$$b^2=c(\varepsilon_{sy}-\varepsilon_{sp})E+c^2$$

$$c=\frac{(\sigma_{sy}-\sigma_{sp})^2}{(\varepsilon_{sy}-\varepsilon_{sp})E-2(\sigma_{sy}-\sigma_{sp})}$$

$$\varepsilon_{sp}=\frac{\sigma_{sp}}{E}$$

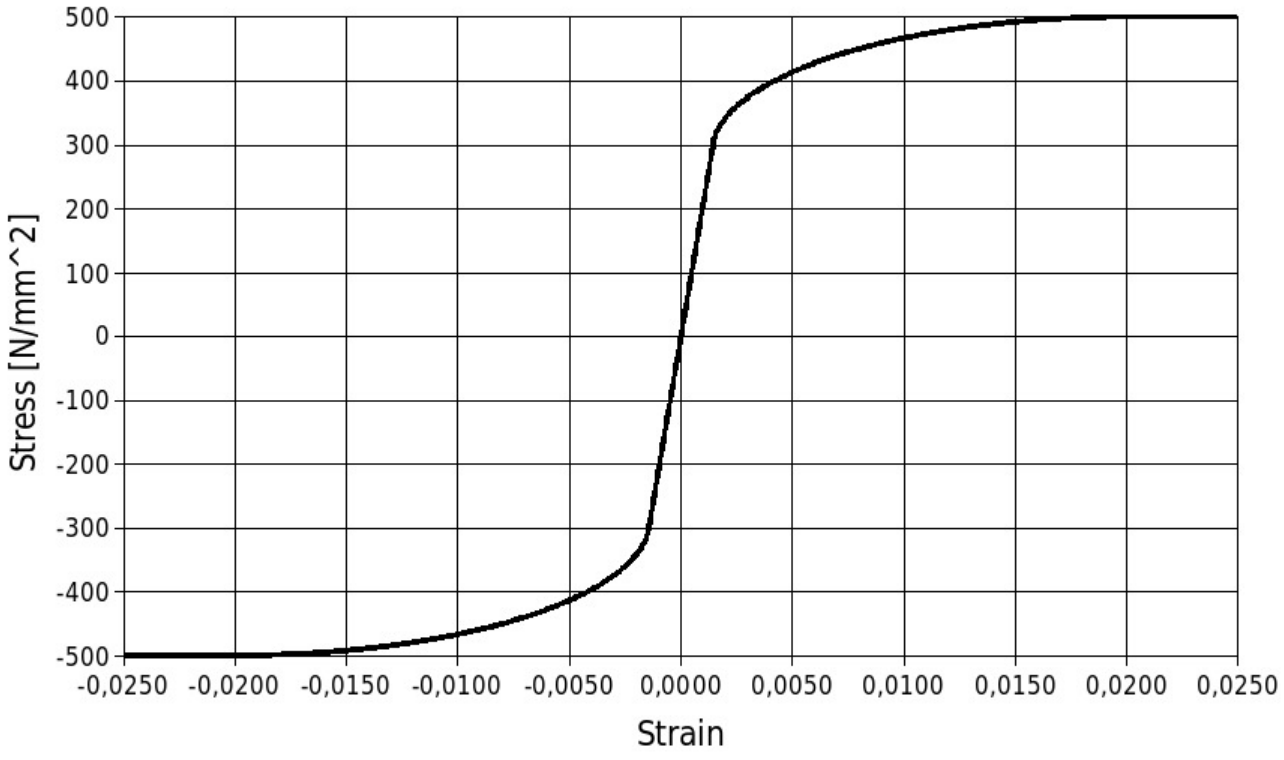

As with the concrete stress-strain relation, a derivative of zero gives problems with convergence, so these domains are replaced with a very small descent of 1×10^{-12} N/mm^2. For the compressive domain the same curve applies, but then, of course, inverted.

The remaining external parameters are:

σ_{sy} σ_{sp} E ε_{sy}

In accordance with the Eurocode, for the fourth value a constant value of $\varepsilon_{sy}=0.02$ will be used, but the other three will be temperature dependent, using a temperature factor that is redirected to a table in the data file (which can be modified for different types of steel). Graphs in this report were created using the values for hot rolled class N steel.

$\sigma_{sy}=k_{sy}\sigma_{sy,ref}$
$\sigma_{sp}=k_{sp}\sigma_{sp,ref}$
$E=k_E E_{ref}$

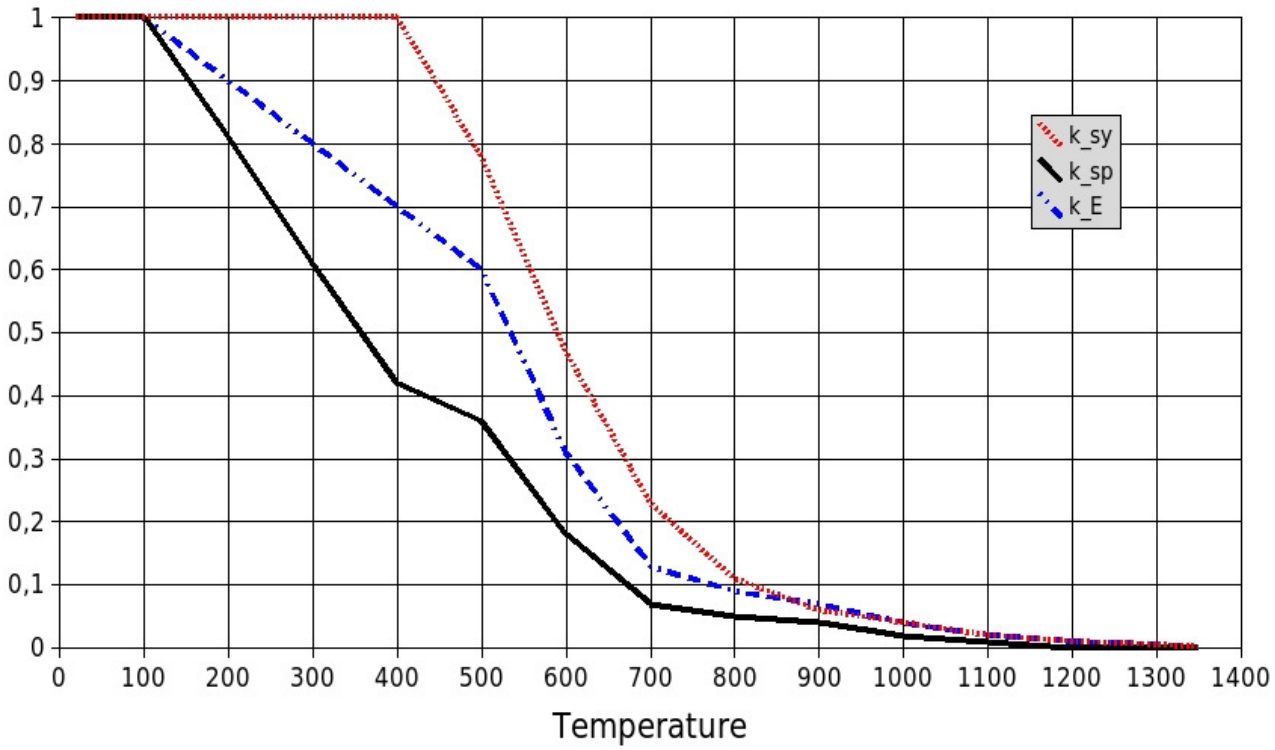

The degradation of the yield stress (dotted line), proportional limit (continuous line) and Young's modulus (dash-dotted line) with temperature.

This means that the following values should be input in the DIANA data file:

Constant material properties	Temperature dependent material properties
• $\sigma_{sy,ref}$ [force/area] • $\sigma_{sp,ref}$ [force/area] • E_{ref} [force/area] • ε_{sy} [-]	• $k_{sy}(T)$ [-] • $k_{sp}(T)$ [-] • $k_E(T)$ [-] • $\alpha(T)$ [1/temperature]

If the cooling down phase is to be simulated, a separate unloading branch should also be added. As with concrete, this can be done using either secant or elastic unloading. Since stresses and strain occur in only one direction, and it is highly unlikely that steel that has yielded in one direction will subsequently yield in the other, neither should present particular problems.

2.5 Results

Now that the complete material model is set up, results can be produced. For this purpose, a fictitious tunnel cross section is used with a constant wall thickness of 1250 mm, a reinforcement area of 2094 mm^2/m (ø20-150 mm) for the outer reinforcement and the middle wall, and an area of 3272 mm^2/m (ø25-150 mm) for the inner reinforcement. Both tunnel tubes have an area of 10,000×5000 mm.

The compressive strength of the concrete is taken to be 35 N/mm^2 (at 20 ºC), its tensile strength 2 N/mm^2. The value of p_t is taken equal to 0.9. The steel strength is assumed to be 500 N/mm^2, with the proportionality limit $\sigma_{sp,ref}$ being 300 N/mm^2. The Young's modulus of the reinforcing steel is taken to be 2.1×10^{11} N/mm^2. The temperature dependence of all these values is as shown in section 2.4.2.2 and 2.4.2.3; values for the thermal analysis are as mentioned in section 2.4.1.

The concrete is loaded by its dead weight (calculated from a temperature independent density of 2400 kg/m^3) and by soil and water pressure. Although technically the tunnel is not 'fixed' in any direction but only kept in place by equilibrium between its weight and external forces, a finite element simulation has problems with such free constructions and needs a point of reference.

Therefore the entire underside of the tunnel is modelled as being vertically fixed. Since the asphalt in a tunnel would provide some isolation, the bending (and therefore, possible cracking) of the underside is always less than that of the roof, the deformations here are not a point of interest, so this can be safely done. By consequence, no boundary elements (that provide the temperature-time relation) are applied to the underside either. The roof of the tunnel is loaded with a constant line load of 200 kN/m.

In the horizontal direction a fixed constraint at a single point in the centre of the middle wall has been applied, so that the external forces on the side walls are at least properly modelled. Technically these would be triangular line loads, but for this purpose they are simplified to constant line loads of 350 kN/m. The loads are applied using simple continuous face loads; a few simulations have been performed with non-linear springs, but this gives huge problems with stabilising the displacement field, without producing fundamentally different results.

This is also the reason why the horizontal pressure is simplified to a constant line load; another option would have been to use a constraint line instead of a constraint point (i.e. fix the entire middle wall in the horizontal direction), but this would probably have a greater impact on the value of the model, because it would prevent the connection between the middle wall and the roof from turning.

For the softening parameters the original intention was to take the values advised by Hordijk ($c_1=3$, $c_2=6.93$ and $w_c=160\mu m$), as well as a realistic value for the fracture energy under compression, such as $G_c=800N/mm^2$ (although estimations of the fracture energy of concrete vary significantly between different researchers). However, as there are three integration points per element, yet the entire element length L_{el} is used during calculation, both w_c and G_c should be multiplied by three. Unfortunately this would cause the calculations to diverge as soon as plasticity starts on the heated side.

The obvious solution to this is of course to increase the value of the fracture energy under compression, which indeed improves the performance of the simulation, but convergence problems persist for all remotely realistic values of G_c. Therefore this value is set to $G_c = \infty$ instead, i.e. ideal plasticity. This is of course not realistic, but since the stresses on the heated side are not the primary interest (the concrete might have spalled off here already), this simplification should not present a major problem (although the strains on the heated side *are* the driving force behind the phenomenon).

Unfortunately this does not completely solve the convergence issue. The initial phase during which plasticity occurs on the heated side is simulated without problem, but the calculation then diverges as soon as plasticity occurs on the unheated side. This means that the fracture energy in tension should also be increased, with significantly better results being obtained for $w_c = 16\,\mu m$, although this often still leads to divergence at a later stage in the calculation, when the cracks are expanding. It is only with $w_c = 1.6\,\mu m$ that the calculation can be run completely and stable under a normal variation of different parameters (see also chapter 5 - sensitivity analysis), yet this is of course a significant loss of accuracy.

Contrary to what one might expect, convergence is actually better with the linear stiffness model than with Newton-Raphson. Refining the mesh also reduces convergence, probably because multiple elements close together all reach the yield point at once. A cruder mesh, on the other hand, improves convergence (only one element is yielding), but, of course, at the expense of accuracy. It should therefore be concluded that convergence of the simulation is an important boundary condition that should not be ignored when designing a material model.

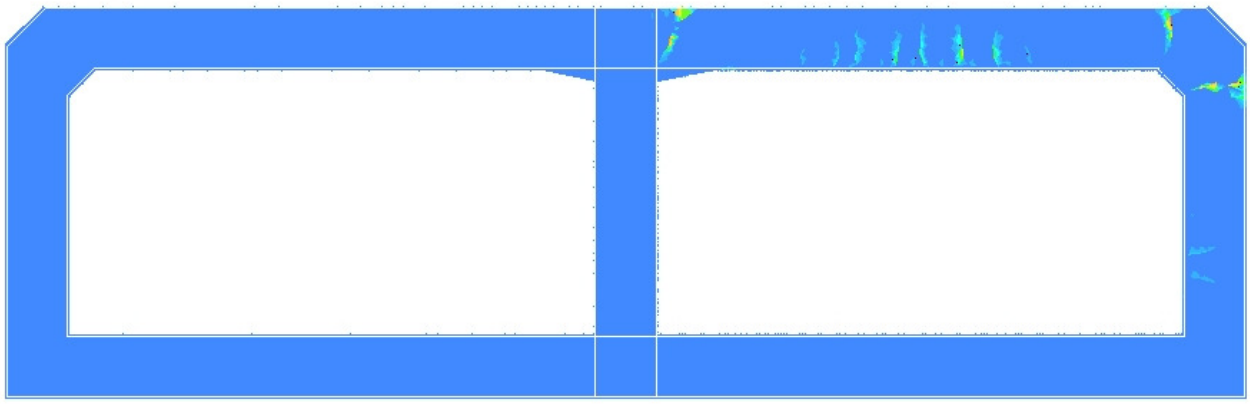

Above is a screen shot of the results obtained with the material model. Plotted here is the value *w*, which has the advantage that it is independent of direction (only the direction with the largest value of *w* is used), and the resulting images is not cluttered with information on plastic strains in compression. As can be easily seen, there are three major cracks, two in the roof, adjacent to the middle and the side wall (the former being the larger of the two), and one in the side wall, just underneath the roof. In addition, there are several normal bending cracks, both in the roof and in the side wall. The spatial relations between the cracks are best understood by plotting the deformations in the same graph (needless to say, the deformations here are greatly exaggerated). The sag of the roof in the middle of the span is equal to 10 mm.

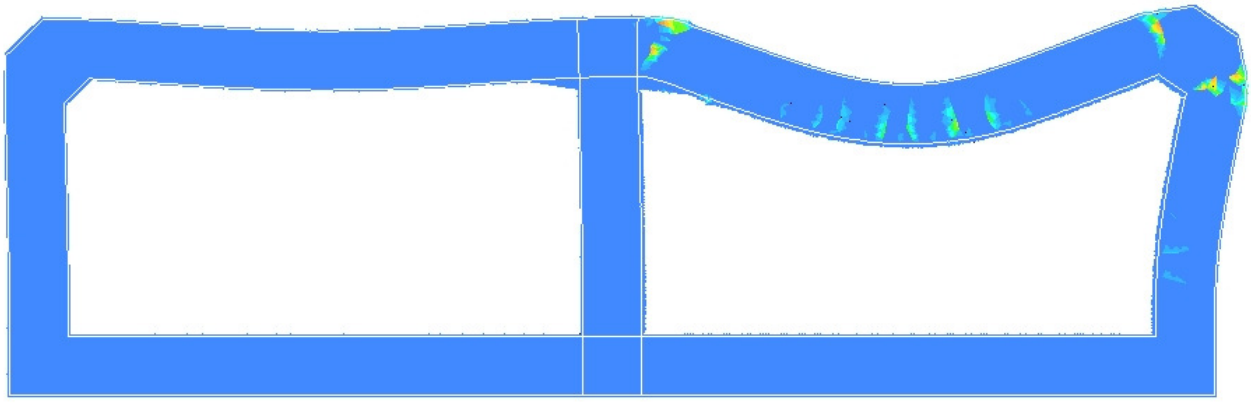

These plots were obtained using a value of $w_c = 16\,\mu m$, which gives divergence before completing the entire Rijkswaterstaat curve. These plots therefore pertain to the last step before divergence, which corresponds to 41 minutes of heating. With $w_c = 1.6\,\mu m$ the entire two-hour curve can be quickly calculated, but then the cracks are smeared out over many elements and not as concentrated. The total crack width can then still be found through summation of the crack widths per element, but $w_c = 16\,\mu m$ (with concentrated cracks) produces a clearer picture, which is why this value is chosen for this chapter. Note how limited the temperature ingress in the cross section is at this point.

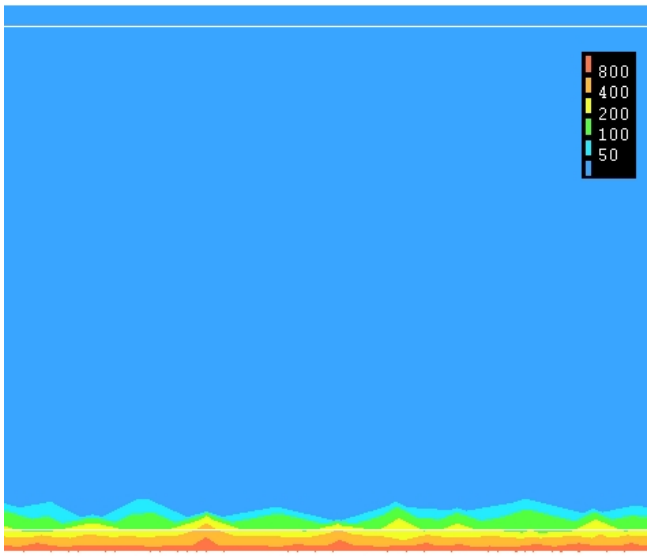

Temperature distribution over the cross section after 41 minutes of heating. Shown is a fragment of the tunnel roof, with a height of 1250 mm; the white lines represent the reinforcement.

It is also of interest to plot the stress distribution for tensile stresses. In the graph on the next page, the stresses in the largest principal direction (σ_1) are plotted. In the middle of the span, there are compressive stresses on both the underside (because of thermal expansion) and the top side of the roof (because of the bending), with a tension band in between. The same occurs in the side wall, but at the corners this tension band moves towards the outside edge, which is why the cracks appear there (but note that in this graph the actual crack locations are marked by a lower stress level, because some softening has already taken place).

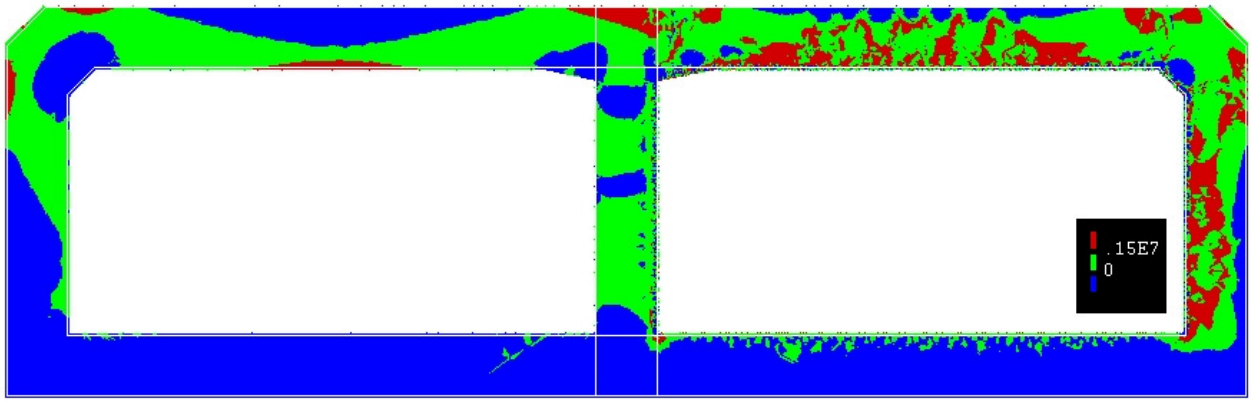

Stress distribution in the cross section after 41 minutes of heating, showing the largest principal value, i.e. tension. The scale is in N/m^2, so the limits used here are 0 and 1.5 N/mm^2 (for a concrete with a reference maximum tensile strength of 2 N/mm^2)

The graph below shows the (tensile) stresses in the reinforcement. As was to be expected, the stress locations coincide with the crack locations, with a peak value of 420 N/mm^2. The stress area hardly extends beyond the crack location because embedded reinforcements have been used, which presupposes perfect bond. The reinforcement on the underside of the roof is in compression, because it is affected by thermal expansion just as the concrete surrounding it is. This means that this reinforcement does not help to reduce the bending.

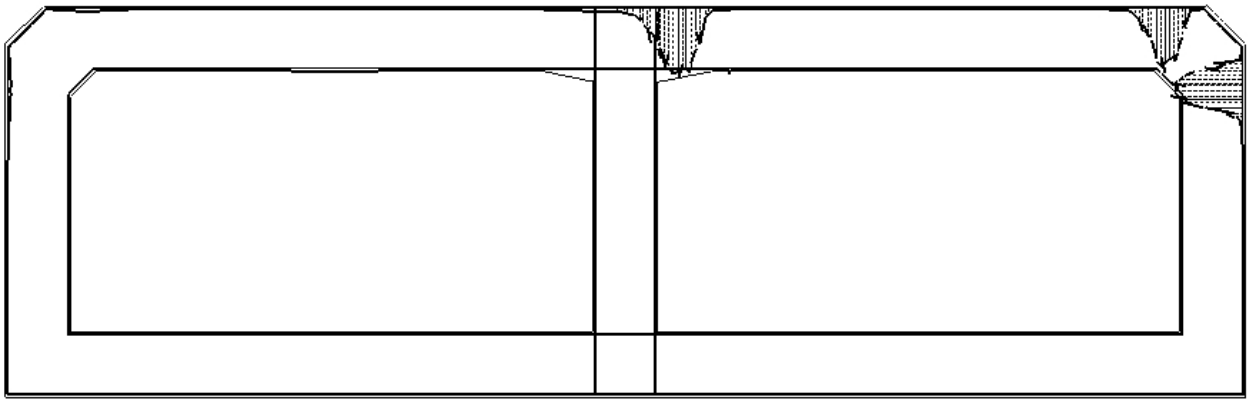

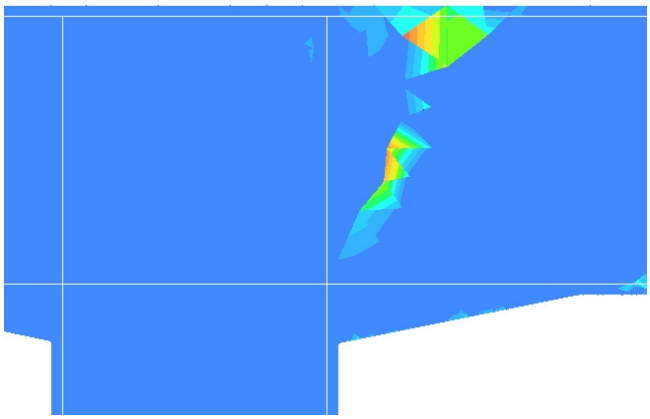

On the left hand side is a closeup of the the crack adjacent to the middle wall, which is the largest of the cracks. The triangular shapes seen here are caused by the shape of the mesh, but it can be clearly seen that the crack is curved, starting somewhat to the right of the middle wall, but moving toward it gradually. At the top side, the smeared crack is essentially two elements wide (with some very small values of *w* in adjacent elements), which means that the crack behaviour can be described by two crack width-time relations, shown on the next page.

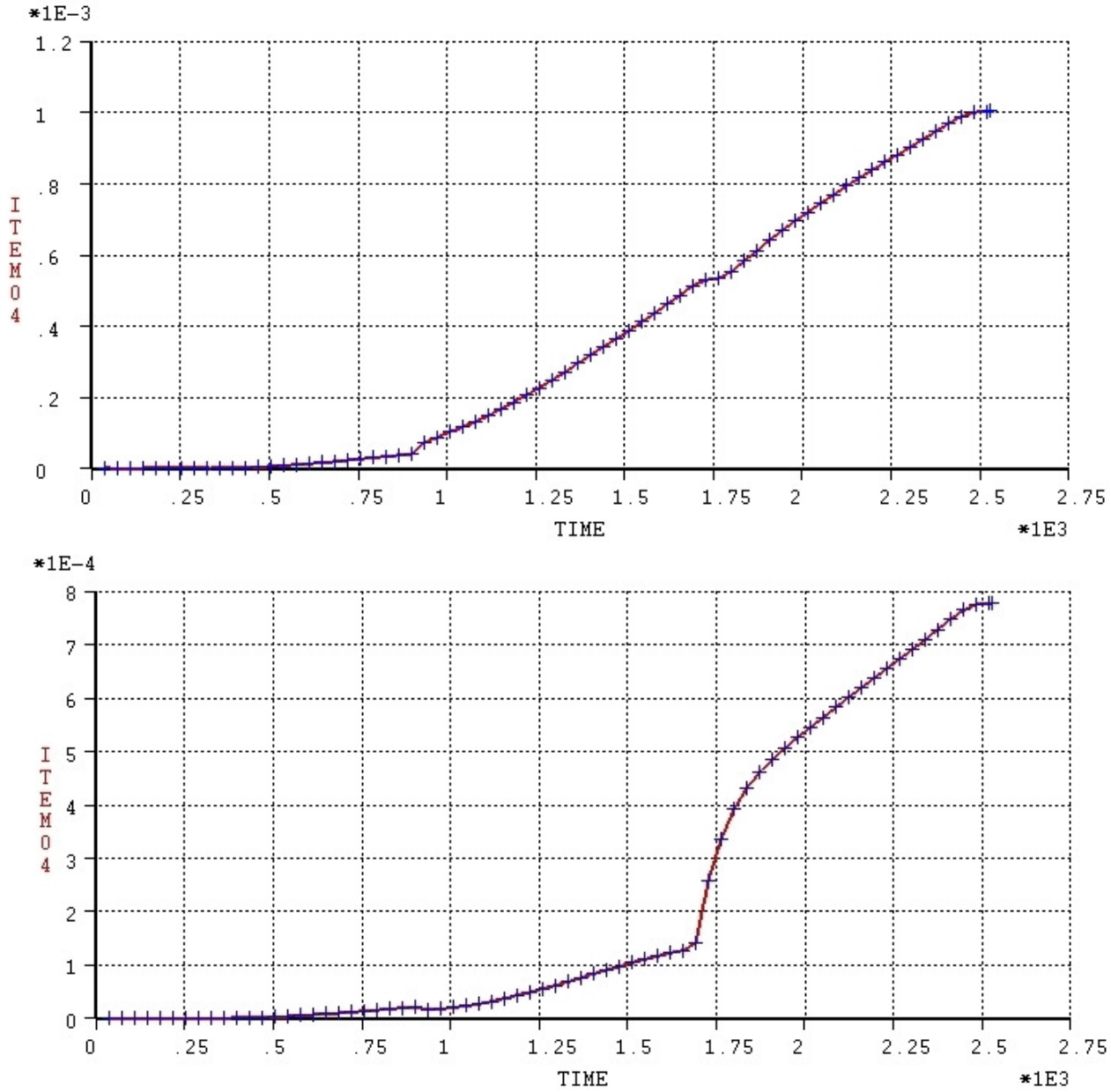

Two crack width-time relationships for two adjacent elements in the crack in the roof adjacent to the middle wall.

Apparently the crack appeared after roughly fifteen minutes (with only very small values of *w* preceding it), with the second element becoming active only after 28 minutes. Note the brief horizontal section at the corresponding location in the graph of the first element. There is again a brief horizontal section in both graphs at 41 minutes, i.e. immediately before divergence. This suggests that at this point a third element will join the crack. It is possible that this is, in fact, the cause of the divergence in this example, but that does not necessarily follow from these graphs.

As mentioned in section 2.4.2.3, values for *w* are computed by multiplying the crack strain by the element length (for each integration point). Because the graphs show the mean value of *w* per element, the total crack width can be found by summating these values, without having to correct for the number of integration points. The total crack width after 41 minutes is found to be:

$1 \cdot 10^{-3} + 8 \cdot 10^{-4} = 0.0018\,m = 1.8\,mm$.

On the right hand side a closeup of the corner of the tunnel is shown, where the two other cracks are. As can be clearly seen, both cracks are slightly curved as well, point towards the inside corners of the element. The crack in the roof reaches a total crack width of roughly 0.6 mm, whereas the crack in the side wall reaches a value of roughly 1.0 mm, summated over the various elements at the surface.

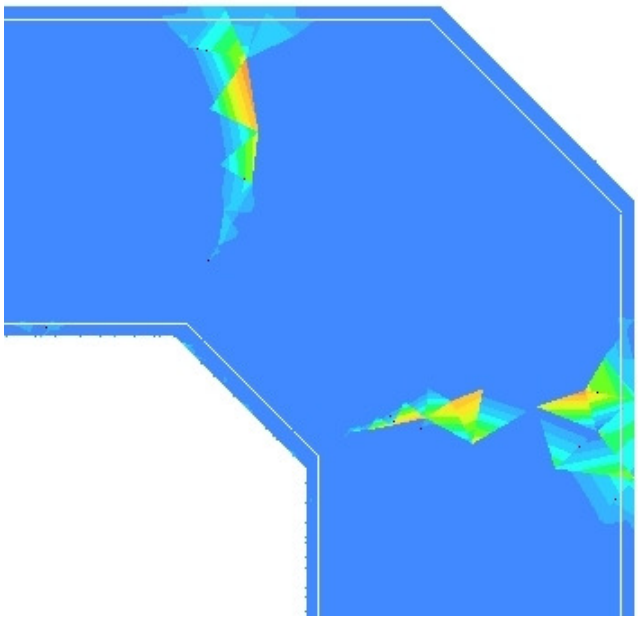

A particular remark should be placed here with regards to the shear capacity of the cross section. In reality, cracks cannot transmit shear stresses, which means that the shear force would have to be transmitted by the (smaller) remaining area, but in the model, this property is not implemented. This is of particular interest, because the cracks occur at the connection between the roof and the walls, where coincides with the locations of the largest shear force.

The actual shear stresses occurring cannot be properly assessed in the current model. A proper model would require assumptions with regard to the speed with which the shear stiffness decreases: obviously, it does not abruptly drop to zero (nor would that be practical to implement, as it would cause an important discontinuity between the steps, see section 2.2). However, a quick calculation can be made to estimate the size of the shear stresses: if the roof thickness adjacent to the middle wall is reduced to 20% of its original value, and the shear stiffness of the other 80% has been completely reduced to zero, the shear stress at this point would be equal to:

$$\sigma_{xy} = \frac{\frac{1}{2} L_{span} \left(\rho h_{original} + q_{external} \right)}{h_{remaining} + h_{chamfer}} = \frac{\frac{1}{2} 10 \left(2400 \cdot 1.25 + 200 \cdot 10^3 \right)}{0.25 + 0.1} = 2.9 \cdot 10^6 N/m^2 = 2.9 N/mm^2$$

If the chamfer is also reduced in height (due to explosive spalling), a very small cross section might be remaining, which could lead to collapse at this point. However, in reality tunnels are never completely unprotected: if PP fibres are applied, explosive spalling should not take place, and if fire-resistant plates are applied, the crack will not be this deep. Therefore, this value can be seen as a reasonable approximation.

This shows that it is necessary to apply shear reinforcement at these locations, and to base the calculation of this reinforcement, as well as the design of the chamfer, to the possibility of a crack occurring on the unheated side. As it happens that most immersed tunnels do have shear reinforcement at these locations, it is likely that this is not a major problem for existing tunnels, but nonetheless, it would be wise to incorporate this knowledge into future designs. It should also be noted that the shear reinforcement should be adequately protected from high temperatures, as its properties will decrease with temperature similar to the reinforcing steel.

3. The lattice model

After an estimation of the location of the cracks using smeared cracking in a finite element analysis, the original idea was to 'zoom in' on a crack, and further analyse its shape, width and depth, as well as the development with time of these aspects. This was to be done using a lattice analysis, where the concrete is modelled by a lattice of one-dimensional elements.

In this case, the crack widths would not have to be calculated from summation of the fictitious crack widths, which means that it would not be as problematic to take a low value for, for example, w_c, which would cause the cracks to be smeared out over many elements rather than localised in one chain. This way, the convergence problems addressed in the previous chapter would have been largely avoided.

In a standard lattice analysis, an external load is applied and increased until the first lattice element yields. This element is then removed from the system, after which the the load is increased again until the second element yields. The process continues until either all elements have been removed, or the load cannot be further increased. The load, in this context, can be either a force or a prescribed displacement.

If the lattice analysis is to be applied to the problem at hand, however, the parameter time needs to be introduced. This can be done by making the external load (force or displacement) time-dependent, and introducing discrete time steps. In each time steps a different number of elements may fail to accommodate the load change, which may also mean that at a particular time step no elements fail at all. It is always necessary to calculate the redistribution of forces after one element has failed, which means that multiple lattice calculations will have to be performed within one time step.

The initial idea was therefore to use the output of the finite element analysis as input for the lattice analysis. If, for example, the size of the entire lattice analysis is taken to be equal to one or two triangular elements in the FEM analysis, then the stress-time relationship (or strain-time relationship) of the Gauss points surrounding these elements can be used as boundary conditions for the lattice analysis.

This reasoning, however, suffers from the important flaw that DIANA already assumes the behaviour of the element to be scrutinised during the finite element analysis, and any results obtained from a lattice analysis will be pre-determined by the assumptions during the FEM analysis. For example, if the strain-time relation as pictured on the next page is taken for the boundary condition, then without doubt the crack will start after 900 seconds, and the eventual crack strain will be equal to 5.5×10^{-3}. The problem is not solved by using a wider portion of the FEM analysis, because the resulting curves would still be dominated by the time at which cracking start, and the subsequent increase of strain.

The same problem would arise if one would take the stress-time relation: the onset of stress decrease occurs exactly where DIANA assumes the crack to start, and the rate with which the stress decreases afterwards is governed by the softening assumptions in the material model. In this case the lattice analysis cannot possibly add anything to existing FEM analysis (aside from producing a visual representation of the assumed crack), whereas the aim is higher accuracy and more detail. This means that the finite element analysis and the lattice analysis cannot be decoupled.

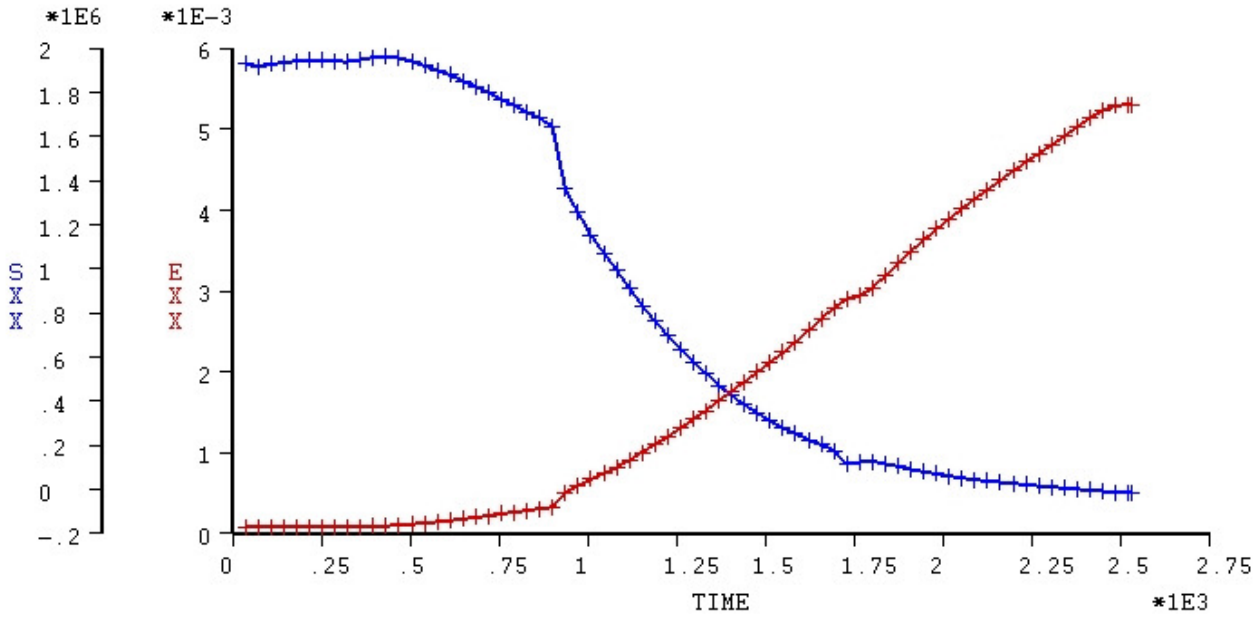

Stress (decreasing) and strain (increasing) development in a crack, as predicted by DIANA.

The solution is therefore to somehow integrate the lattice analysis into the finite element analysis. DIANA has a built-in lattice module, but its application is rather limited, since it only allows for a linear static analysis (which means it cannot be combined with the existing non-linear time-dependent analysis). Nonetheless, the lattice analysis can just be re-created in DIANA, if the basic principles are observed:

1. A lattice is built of regular beam elements
2. The beams are somehow connected to the two-dimensional continuum elements
3. The lattice beams have a linear elastic stress-strain relation
4. A beam that reaches yield stress should be removed from the system
5. Time steps are chosen in such a way that only one elements can yield per step

There are no automatic meshing options for dividing a field into lattice elements in DIANA, but by copying elements using relative translations, a regular mesh can easily be created. If this mesh consists of regular triangles with corners of 60º, the shape of the crack is only marginally influenced by the shape of the mesh (see Schlangen & Garboczi, 1997).

DIANA offers three types of beam elements, numbered class-I, class-II and class-III. The latter contains curved beam elements, which are not applicable here. In addition to beam elements there are also truss elements, which cannot bend and transfer no moments. Since Schlangen (1993) asserts that the moments are important to properly describe the fracture process, trusses should not be used here.

The primary difference between class-I and class-II elements lies in their shape functions, the class-II beams having an extra term in the shape function for displacement in the direction of the beam length. This allows the strain to vary linearly over this length, whereas class-I beams can only have a constant strain.

This also has consequences for the strain and stress vectors: in a class-I beam ε_{xx} is constant, so the strain vector can directly relate to the change in length and the curvature, whereas in a class-II beam ε_{xx} is the primary value of interest. There are then multiple integration points over the (fictitious) height of the beam, from which the curvature can be calculated by the user. The same applies for the stress vector: for class-I beams DIANA can directly calculate N and M at the two ends of the beam; in a class-II beam these need to be computed from the stress distribution over the beam height.

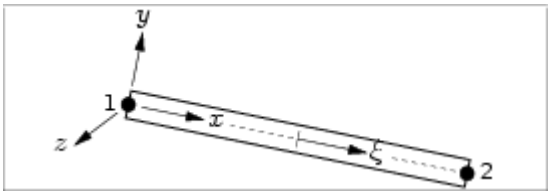

A beam element (L6BEN or L7BEN). Image taken from the DIANA manual (TNO DIANA, 2007)

	Class-I (L6BEN)	Class-II (L7BEN)
Shape functions	$u_x(\xi)=a_0+a_1\xi$ $u_y(\xi)=b_0+b_1\xi+b_2\xi^2+b_3\xi^3$	$u_x(\xi)=a_0+a_1\xi+a_2\xi^2$ $u_y(\xi)=b_0+b_1\xi+b_2\xi^2+b_3\xi^3$
Integration points	3×1	3×3
Strain vector	$\vec{\varepsilon}=\begin{bmatrix}\Delta u_x\\ \kappa_z\end{bmatrix}$	$\vec{\varepsilon}=\begin{bmatrix}\varepsilon_{xx}\end{bmatrix}$
Stress vector	$\vec{\sigma}=\begin{bmatrix}N_x\\ M_z\end{bmatrix}$	$\vec{\sigma}=\begin{bmatrix}\sigma_{xx}\end{bmatrix}$

It goes without saying that class-I beams are easier to use, and, for a standard lattice analysis, these should be enough to fulfil the required function. In the problem at hand, however, there is a spatial temperature distribution, which cannot be accommodated in beams with a constant strain. Secondly, these beams do not allow the use of a user-supplied material model, which will be needed to make the yielded beams disappear. For these two reasons, the class-II beams must be used for this particular problem.

If the lattice is assembled to create a large triangle (which will, of course, also have angles of 60º), this can be connected to the rest of the tunnel by 'cutting out' a triangle of the continuum elements at the location where the crack was observed in the first analysis (without lattice elements). The proper connection between the two types of elements is ensured by the use of tyings, which relate the degrees of freedom of different elements in a way that ordinary meshing does not.

The tyings can be used to connect lattice elements to the sides of continuum elements. Because the lattice elements are much smaller than the continuum elements, there will not be as many nodes on the continuum side; the tyings ensure that the (under normal circumstances) unconnected lattice nodes are connected to the nearest continuum nodes. But tyings are also necessary for connections where lattice elements and continuum elements meet in the same node, because by default the curvature of the beam would not be linked to the curvature of the continuum elements. The tyings here ensure a non-rotating connection.

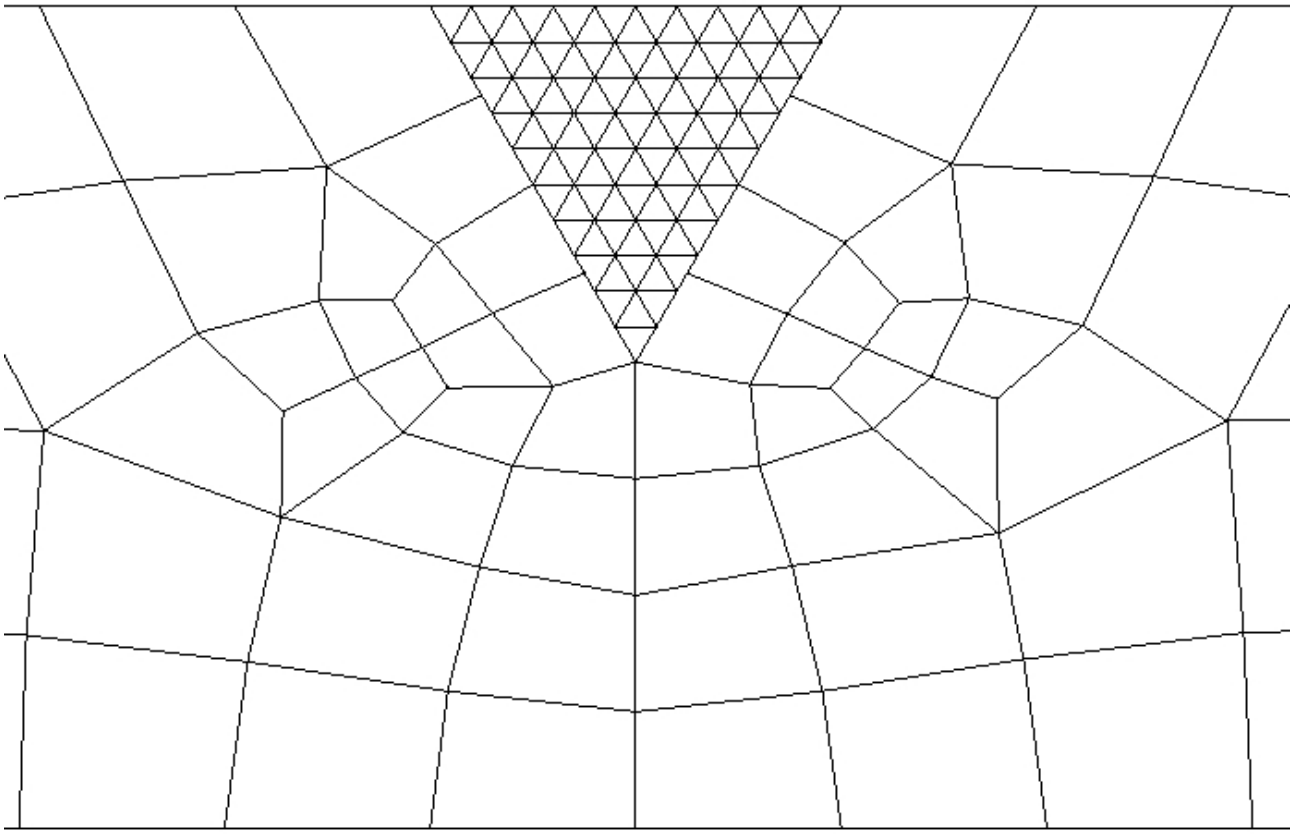

A (fictitious) cross section with a lattice part (regular triangular mesh) connected to a continuum mesh (consisting of quadrilaterals).

Although the built-in lattice module in DIANA was in itself of no use for the purposes required here, its automatic tyings generator AUTOTY can save a lot of work, with usually only minor changes being required to its output file (in this case, the use of triangular continuum elements instead of quadrilateral, which causes a minor renumbering of the nodes). Because AUTOTY is an executable command instead of a preprocessor option, this means running a demo file, and (after any necessary editing) copying the outputted tyings back into the real data file.

The standard embedded reinforcements do not work anymore for lattice elements, because they can only be embedded in continuum elements. This means that, instead, the reinforcement at this location should be modelled explicitly using beam elements, connected to the continuum elements using interface elements. Bond-slip behaviour is then defined for the interface elements, for example using the cubic function by Dörr (1980). The reinforcements can in no way be bonded to the lattice elements, but since this only a small length, this should not be a major problem.

The stress-strain relation of the lattice elements is best described using a user-supplied material model, which can also keep track of which elements have disappeared. The problem here is that normal lattice behaviour entails brittle failure of each of the elements, which is problematic for the convergence of the simulation (see section 2.2). To solve this problem, a hardening parabola and a softening curve should be added to the linear elastic branch (the same curve as used for the continuum elements; see section 2.4.2.3).

Adding a softening curve to a lattice analysis would only enhance the model, because softening is a realistic aspect of concrete. However, as part of the softening is already accounted for by the lattice model itself, only softening on a microlevel can still be described by an element itself. This means that a shorter softening curve should be used with a smaller fracture energy. The Hordijk curve can easily be adapted for this purpose by using a smaller w_c, although - again - convergence problems limits the values that can be taken for this parameter.

Any element that has yielded should be marked as having disappeared (even though it can still have stresses in its softening curve) to facilitate the plotting of the crack after the simulation is complete (although note that the crack width is the elongation of the elements having 'disappeared', not the open space in the plot). This can be done by creating a group which contains the element numbers of the remaining elements (including the continuum elements), which will then become available in the post-processor as a set which can be plotted (although an extra calculation command needs to be given after the actual calculation is over, to ensure that the group information is actually read).

The difficulty is now to ensure that only one beam element fails per time step, because the calculation cannot be restarted from beam #1 once it is found that, for example, beam #47 has yielded. It is not possible for the material model to give some feedback to the iteration mechanism, so the time step cannot be adjusted in the process. The only thing that can be done, therefore, is to take very small time steps throughout the simulation, but this is rather inefficient. However, as the error introduced by four or five elements failing at once is relatively small (especially when 'failing' entails they are still softening), accepting that multiple elements will fail at once is a more practical approach. There is a balance here, of course, between accuracy and efficiency.

The major problem of applying the lattice model in a normal finite element method lies in the combination of the softening curve (which is required to avoid brittle failure) and the class-II beam elements. As pointed out before, these beams do not simply have the normal force or the moment as its property, but the local stress σ_{xx} in different integration points over the height of the element. Of course, it is not difficult to calculate N and M from σ_{xx}, but the material model necessarily works integration point based, rather than element based.

Because of the nature of the problem, there are typically large moments in the lattice elements that will lead to ε_{xx} exceeding the set limit value. Because the material model evaluates the elements per integration point, it is quite possible that only the seventh integration point yields, whereas the first sixth points had lower strains (and, typically, a number of them compressive). This would theoretically lead to a local failure of an element, but that can, of course, not be accommodated by a single element (and meshing the beam elements into small continuum elements is not very efficient either).

If the whole element would have been assumed to disappear instantly, such a local failure would not have been a problem (it would automatically imply total failure of the element to which the integration point belongs). Yet, as has been pointed out before, brittle failure is not possible, because continuity between the time steps must be observed. The softening of only one integration point, however, leads to an alteration of the normal force and moment field, because the ratio between the stresses is altered (and the stresses calculated at previous integration points can not be retroactively changed to adapt the softening of an integration point encountered later in the calculation). If this alteration does not fit in the global calculations of the simulation, divergence results.

Of course, convergence is improved by taking larger values for w_c, i.e. lengthening the softening curve and increasing the fracture toughness. Besides this not being realistic, this also introduces a new problem: it means cracks will not localise. Because the lattice elements are typically very small, there are only small differences in stress between adjacent elements. This means that, after one element has failed, the other elements next to it will also fail.

This is not solved by taking smaller time steps, because the first element is still softening when the next elements are failing. This means that even when the time steps are taken so small that only one element fails per time step, still all elements in the first row (i.e. the one next to the surface) will fail (one by one), before the first element in the second row fails. Subsequent strains are spread out over the entire row of elements, which means that the result is in effect smeared cracking.

In order to force the crack to localise, one element was then removed in advance, creating a small notch. The first element to fail is then, of course, the element in the second row just beyond the notch. After this, however, the elements in the second row adjacent to the first element will start to yield, without anything happening in the third row. After a number of elements having yielded in the second row, the calculation diverges. Hence, this option only moves the problem, without solving it.

A second option tried is to randomly distribute the strengths of the lattice beams. If the bandwidth is not too large, this will actually lead to a localisation of the crack, starting in, for example the second row. From there, the crack grows inwards properly, with only one or two elements failing adjacent to the main path (which is not a problem; cracks are irregularly shaped after all). However, as the crack growth proceeds, the stresses also build up in the remaining element in the first row. At the point where this element is supposed to yield, the simulation diverges.

In reality, this would obviously have involved the moving of the stresses in the yielding element in row one to the first intact row, for example the fifth. However, this would imply a radically different stress field, which violates the principle of continuity between the steps, as described in section 2.2. Different functions for the strength distribution give different results, but this problem always persists. Therefore randomly distributing the strengths is not a solution either.

This therefore leads to the fundamental problem of integrating the lattice analysis with the rest of the finite element analysis: it is not possible to find a value of w_c (or, indeed, any softening curve) that will lead to usable results. If the value is too small the calculation will diverge because of the stress situation within an element; if the value is too large the crack will not localise. Since there is also a range of values for which cracks fail to localise *and* the simulation eventually diverges, it is likely that there is not a single applicable value of w_c. It should therefore be concluded that a lattice analysis cannot be integrated in a non-linear time dependent finite element analysis.

Perhaps the solution would be to integrate the entire lattice model within a single (continuum) element. Then DIANA could treat it like any normal continuum element, but when the calculation reaches this element, the user-supplied material model would initiate a complete lattice analysis with all elements being fictitious, iteratively increasing the load (a factor times the strain vector) until the actual value of this vector is reached. The resulting stresses would then be returned to DIANA as the stress vector.

However, it is doubtful what the convergence behaviour of a calculation involving such an element would be, especially if multiple of these 'lattice model elements' are used adjacently. And how would one calculate the derivative of the stress vector in the tangent stiffness modulus, required to stabilise the calculation? This would probably require performing multiple analyses subsequently with a slightly modified strain vector, calculating the derivatives from the differences in response, which is not very efficient.

A completely different approach to assessing crack width and depth would be to use discrete crack elements. The length is initially equal to zero, and can only grow once the yield stress has been reached (at which point opening can start abruptly or using a softening curve, the second probably being advisable). The downside is that one has to specify both the exact location and the shape of the crack in advance, which reduces the amount of information that can be obtained. Using multiple discrete crack elements next to each other and leaving it to the finite element analysis to open the appropriate one would avoid this, but this might lead to convergence problems.

4. Fire tests

4.1 Test setup

Concurrently with this master's thesis, actual fire tests were carried out at Efectis, aimed at finding the difference between unprotected tunnels, tunnels protected with fire-resistant plates and tunnels protected with fibres. The fire tests were planned before this master's thesis was started, which means that the test specimens were already designed and ordered beforehand, but during further planning and execution there was a close cooperation. Performing actual fire tests is an important opportunity to assess how realistic the outcome of the model is.

Because an actual size tunnel would not fit in the oven, the decision was made to scale the tunnel to a size 1:10, meaning the resulting specimen has two tubes of 1000x500 mm and a consistent wall thickness of 125 mm. To make casting the specimens easier, all corners were made straight instead of chamfered. Because scaling the reinforcement is rather difficult, two nets of ø12 - 150 mm were used, with 35 mm cover on both. This means the reinforcement is relatively heavy, but also relatively farther from the edge.

The scaling of the wall thickness is problematic, because the phenomenon of cracking on the unheated side is governed by the relation between the thermal conductivity and the wall thickness. As the thermal conductivity cannot be scaled, this means that the 'heated region' of the wall (the region that reaches temperatures in excess of, for example 100 ºC) will be relatively large compared to the 'cold region' (where such temperatures are not reached), a fundamental difference from an actual tunnel.

This could have been compensated by also scaling the time scale, i.e. also increasing the rate of temperature increase with a factor ten, but this is beyond the capacity of the oven. In addition to this, the resistance of the wall to bending will be decreased because of its smaller height, which may lead to larger cracks than in a real tunnel (in a relative sense). Also, the moisture system is different, because moisture from the heated zone can reach the unheated side quicker. Performing the tests is still valuable, however, because it does provide feedback to the FEM simulation, as long as these differences are kept in mind.

For the testing nine different specimens were cast: three specimens without fibres, three with fibres 18 µm in diameter, and three with fibres 32 µm in diameter. All fibres were 12 mm in length. Due to a miscommunication, three additional specimens were produced with fibres 32 µm in diameter and 6 mm in length. The specimens were cast in February and March 2008. The specimens were all supposed to be B35, but the resulting strengths varied strongly.

In March 2008 a preliminary test was performed on a discarded specimen (whose surface was deemed too rough). This test primarily functioned to assess the capabilities of the oven, and to see whether developing cracks could be clearly observed. The test was not intended to test the fire characteristics of the particular specimen, therefore it was not a problem that the specimen was discarded and only one month old at the time of testing.

The specimen had an arbitrary length of 2000 mm, whereas the oven was 3000 mm in width. Gas burners were present in the oven on the opposite walls, so extra constructions of autoclaved aerated concrete (AAC) blocks were used to build extra walls between the tube to be heated and the oven wall. These extra sections were then covered by a fire-resistant plate, so that the fire could not escape here. A fire-resistant plate was also placed on the bottom of the specimen, to represent the asphalt. A skew wall of AAC blocks were also placed before the gas burners, to improve air circulation, rather than having the gas burners blow directly towards each other.

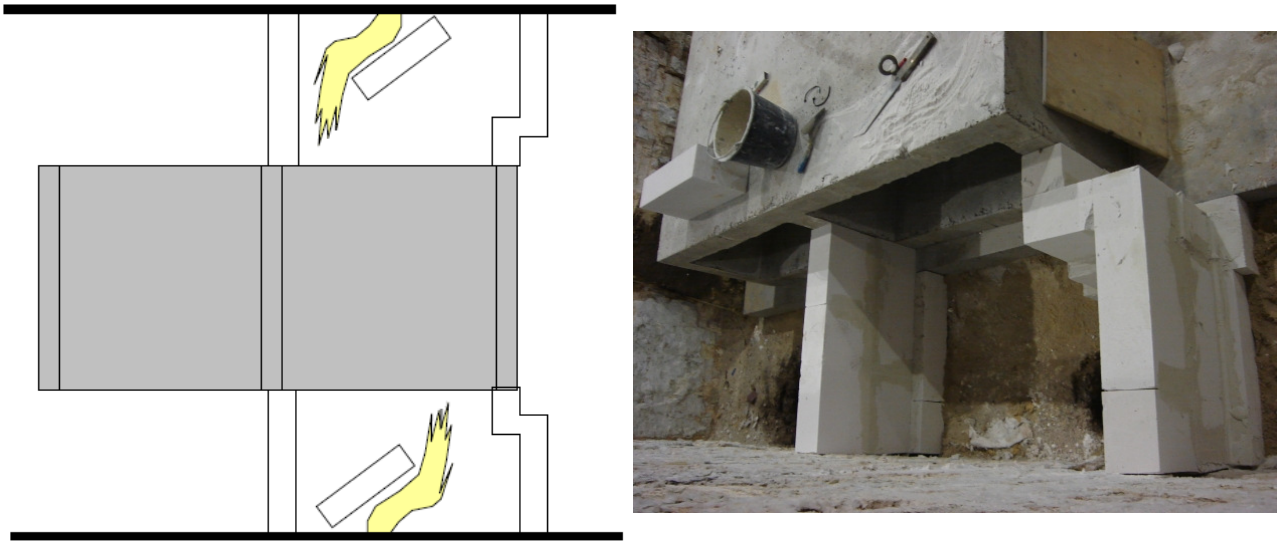

A schematic of the test setup with the specimen in grey, as well as a photograph taken during the building phase. The skew wall was not yet placed here. Schematic and photograph by Efectis.

As can be seen in the diagram, there is a slight corner in the AAC walls, because the ventilation holes (in the oven floor) would otherwise be exactly underneath the walls. The ventilation system was turned on during the tests, to avoid pressure building up in the tubes (which is a different effect that should not be tested at once with the temperature). Thermocouples were placed between the walls and the specimen, to measure the temperature in front of and inside the tube (the specimen itself was not bored). Additional thermocouples were placed on the unheated side of the roof.

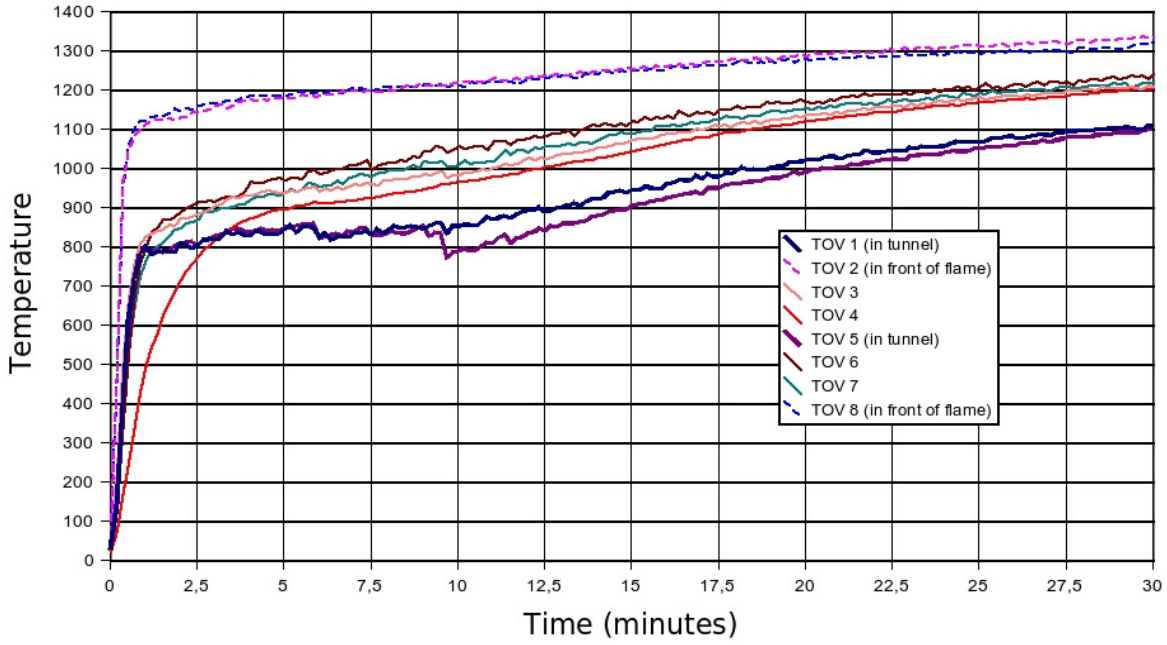

Throughout the preliminary test, the specimen was heated using two gas burners at maximum rate. The resulting temperature curve, shown on the previous page, is lower than a standard Rijkswaterstaat curve, probably due to the size of the open space in the tube combined with the ventilation system. It can also be seen that the temperature in front of the flame is significantly higher than the temperature next to it, suggesting that air circulation is not optimal. The temperature curves inside the tunnel show a horizontal section at 850 degrees, most likely corresponding to explosive spalling (this also corresponds to sounds heard during that period).

The specimen after eight minutes of heating. Notice the radial crack pattern on both sides of the specimen (with moisture emerging). With some difficulty, the dry crack adjacent to the middle wall can already be seen here, where the arrow points.

The first cracks on the unheated side were observed after roughly five minutes, appearing in a radial pattern at the sides where the gas burners were located. A lot of moisture emerged from these cracks. After ten minutes, a longitudinal crack exactly adjacent to the middle wall was observed (this relative position could be determined because the width of the tube was marked on the exterior). No moisture emerged from this crack, which made it difficult to see (and therefore, possible that it had existed for several minutes before being noticed).

The specimen after 14 minutes of heating.

Between ten and fifteen minutes after the start of the test, equidistant horizontal cracks (i.e. perpendicular to the middle wall) appeared over the entire length of the specimen, from which a lot of moisture emerged. During this period cracks also appeared in the side wall of the specimen, running over the entire length. After twenty minutes, the top of the specimen was completely moist, which limited the view on the exact location of the cracks. However, it could clearly be seen that the longitudinal crack adjacent to the middle wall had grown to a significant size, estimated to be between 0.5 and 1.0 millimetre.

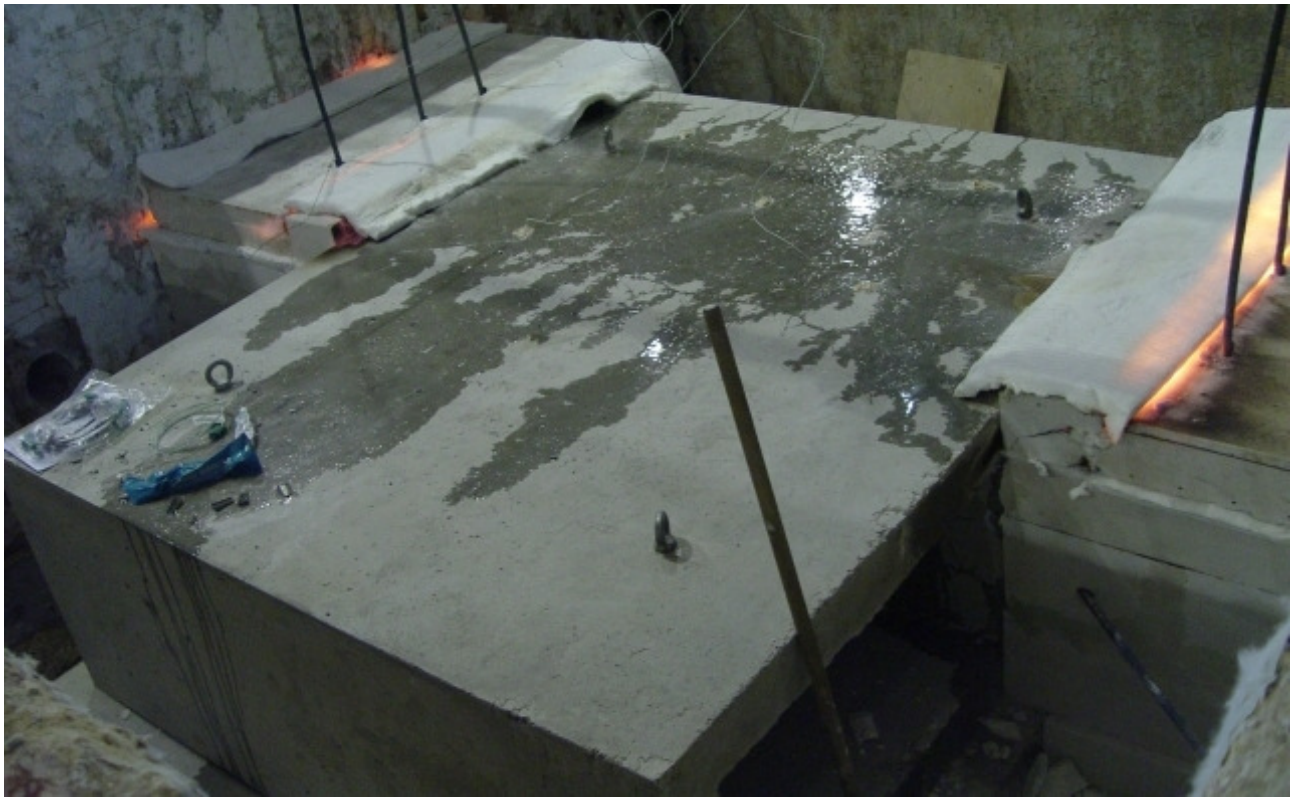

The specimen after 20 minutes of heating. The amount of water emerging from the cracks has become so large that it is now flowing toward the unheated side, even though no cracks appear here.

A photograph from the reverse angle showing the side wall of the picture after 20 minutes of heating.

The second largest crack at this point was a longitudinal crack in the side wall, located exactly beneath the height of the roof. A radial pattern also appeared at the two sides of the specimen (where the burners were), from which a lot of water emerged (relatively little water emerged from the large crack). After thirty minutes the test was stopped.

The specimen after 30 minutes of heating, when the water on top of the specimen is boiling. Notice how clearly the crack adjacent to the middle wall stands out now.

Water emerging from the middle wall after 30 minutes of heating. The photograph is taken from the unheated tunnel tube.

During cooling down, the water dried up again, leaving dark marks where the cracks had been. At this point it could be observed that several longitudinal cracks had developed on the roof parallel to the main longitudinal crack, although these cracks do not run over the entire length of the specimen. The distance between the cracks appeared to be equal to the distance between the perpendicular cracks, which suggests some relation with the reinforcement net, which also had equidistant bars.

The specimen during cooling down.

A photograph from a reverse angle showing the side wall during cooling down. It can now clearly be seen that beside the radial pattern, a single longitudinal crack dominates.

The temperatures on the unheated side were also measured, but these temperatures appear to be mainly influenced by the presence or absence of water at the particular location of the thermocouple. After 25 minutes the water on top of the specimen was boiling, explaining the plateau at exactly 100 ºC. The dashed line represents the air temperature of the surroundings.

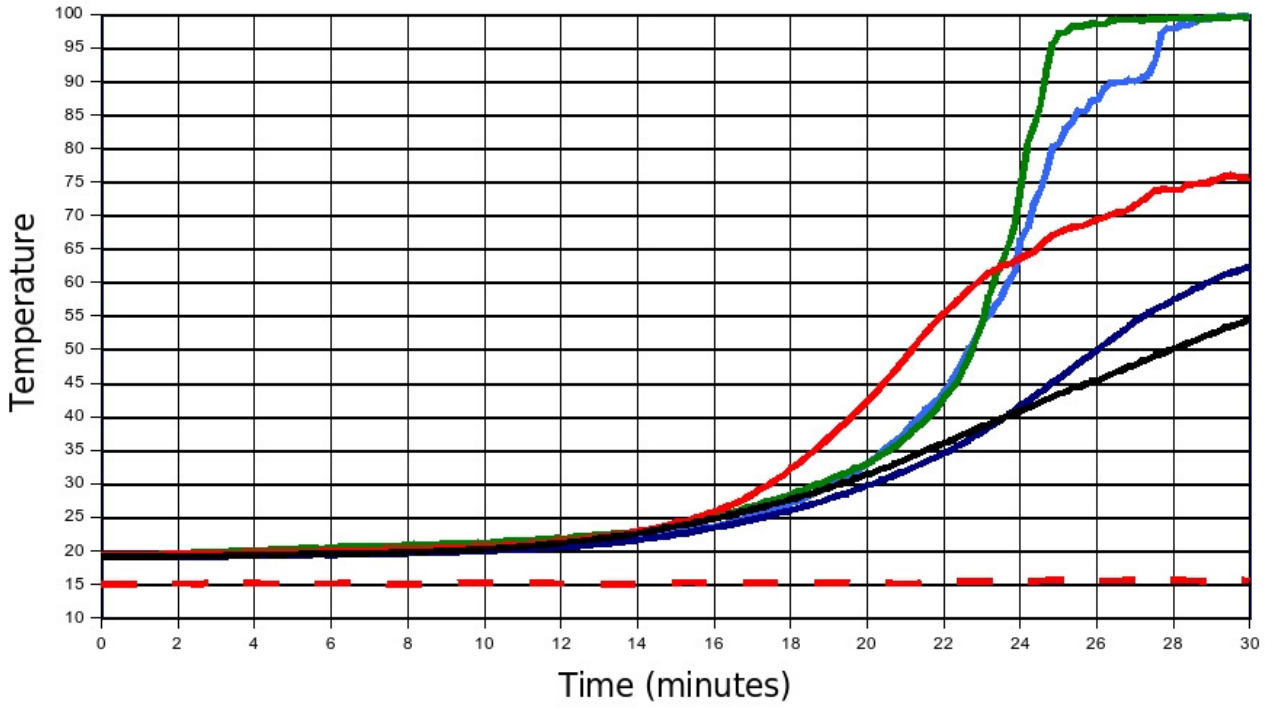

A few days after the test the specimen was removed from the oven, and the inside of the tube could be observed. As can be seen in the picture, noticeable spalling had taken place.

The inside of the heated tunnel tube a few days after testing, showing that the reinforcement has been laid bare.

4.2 Adapted finite element simulation

Because tunnels specimens used in the fire tests are fundamentally different from actual tunnels, the previously described mesh (see section 2.3) cannot be used to predict the behaviour of these specimens. Therefore a special mesh has been created that properly describes the dimensions of the scaled tunnel elements. If the model can accurately predict the behaviour of the specimens using this adapted mesh, then it seems reasonable to assume that its prediction of the behaviour of an actual tunnel using the original mesh would also be accurate (although this is an extrapolation).

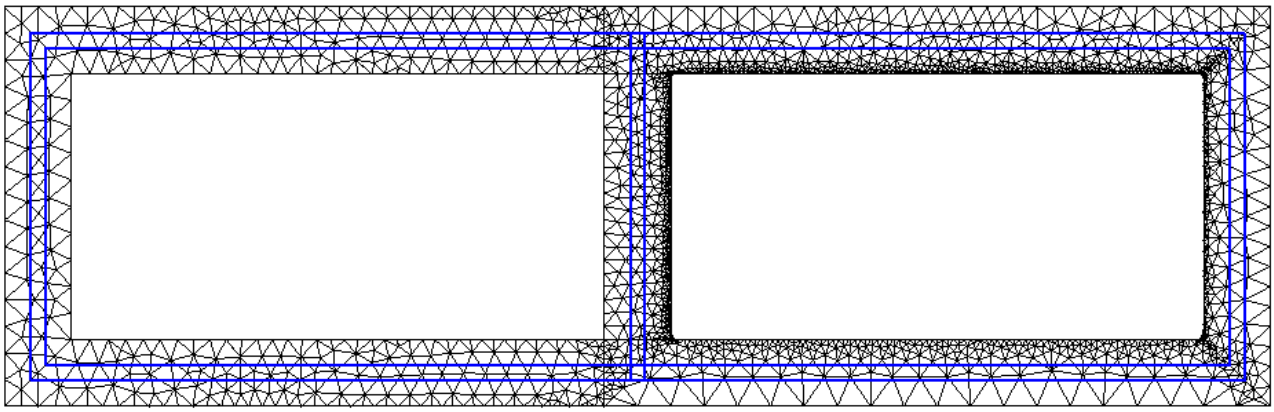

The adapted mesh used for to model the test specimens. The continuous lines in the middle of the cross section represent the reinforcement.

Of course, the fact that the mesh is a factor ten smaller than the mesh shown in section 2.3 does not show in the above picture, because it is stretched to fill the width of this page, but that does result in the more central placement of the reinforcement, as well as in the individual elements appearing larger (although in actual size they are smaller). The specimen is not loaded except by its own weight.

If the unheated side of the tunnel reaches higher temperatures, it will be cooled by the outside air, which will still be room temperature. Therefore additional boundary elements should be added to this side (as well as to the unheated tunnel tube), otherwise this would constitute an adiabatic boundary. The properties of the boundary elements are identical to the boundary elements described in section 2.4.1, but the air temperature-time relation is set to be constant at 20 ºC.

It is known from the preliminary test that moisture will emerge on top of the specimen during the test, which will over time reach boiling temperature. This will of course affect the surface temperature, but this cannot be modelled, because this water may not emerge in every test, or at least not at the same rate (and indeed this varied noticeably between the subsequent tests). For the heated side, the curve used in the preliminary test was used (instead of the Rijkswaterstaat curve), because this curve would be used for all further tests.

The concrete strength was found to be 47.4 N/mm^2 in a standard compressive cube test. The actual compressive strength that can be input into the model can therefore be assumed to be roughly $0.72 \cdot 47.4 = 34\, N/mm^2$. However, as these tests were performed 28 days after casting, but the actual fire test was performed 133 days after casting (19 weeks), the concrete strength should be assumed to be higher by this point. Therefore, a compressive strength of 40 N/mm^2 was assumed.

Unfortunately, the moisture content of the specimens was not measured, and variations between the specimens may have resulted from different storage conditions (outside and inside). As the moisture content is not a model parameter, this does not directly influence the results (although general assumptions have been made, as explained in section 2.4), but a possible variation may be problematic because it influences the comparison.

A summary of the material properties used is given in the table below.

Concrete properties	
Conductivity	See graph in section 2.4.1
Volumetric specific heat	See graph in section 2.4.1
Density	2400 kg/m^3
Coefficient of thermal expansion	See graph in section 2.4.2.2
Tensile strength (at 20ºC)	2 N/mm^2
Compressive strength (at 20ºC)	40 N/mm^2
Decrease of strength with temperature	See graph in section 2.4.2.3
c_1 (Hordijk parameter)	3
c_2 (Hordijk parameter)	6.93
w_c (Hordijk paramater)	16 µm
Relative height of parabola (p_t)	0.1
Compressive fracture energy	1×10^{50} (i.e. infinity)
Load induced thermal strain (LITS) factor	2
Reinforcing steel properties	
Coefficient of thermal expansion	See graph in section 2.5
Tensile and compressive strength (at 20ºC)	500 N/mm^2
Proportionality limit (at 20ºC)	300 N/mm^2
Young's modulus (at 20ºC)	2.1×10^{11} N/mm^2
Decrease of strength, proportionality limit and Young's modulus with temperature	See graph in section 2.5
Strain at peak stress	0.02
Boundary element properties	
Convection factor	25
Emissivity	0.7

In the first analysis run with this mesh and these parameters, the deformations of the tunnel were completely different from those observed in the preliminary test, with the roof bending upwards rather than downwards, as shown in the picture on the next page. This is of course not realistic: it could never happen in a real tunnel (because of soil and water pressure), and clearly did not happen during the preliminary test either. The error might have been caused by an underestimation of the thermal strains perpendicular to a load (see section 2.4.2.2) at the underside of the roof (where the 'load' is caused by the build-up of thermal expansion in the horizontal direction).

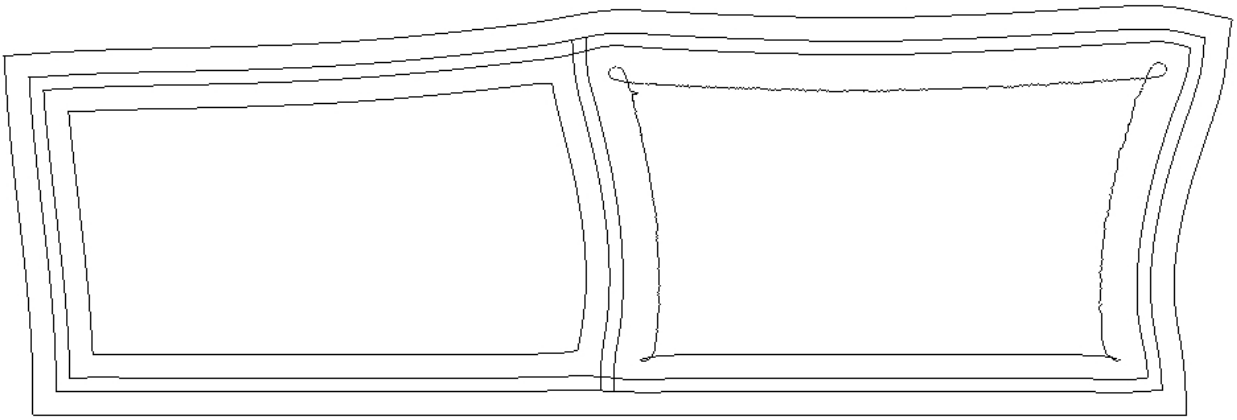

The incorrectly predicted deformations when no load is applied except for dead weight.

In subsequent analyses a small vertical load of 0.1 N/mm^2 has been added to the roof of the tunnel. Given the strength of the tunnel it is not to be expected that this will make a difference to the stress and strain distribution in the tunnel, but evidently it is enough to cause the proper failure mechanism to occur. The result is shown below for a concrete heated 30 minutes using the test curve described in the previous section.

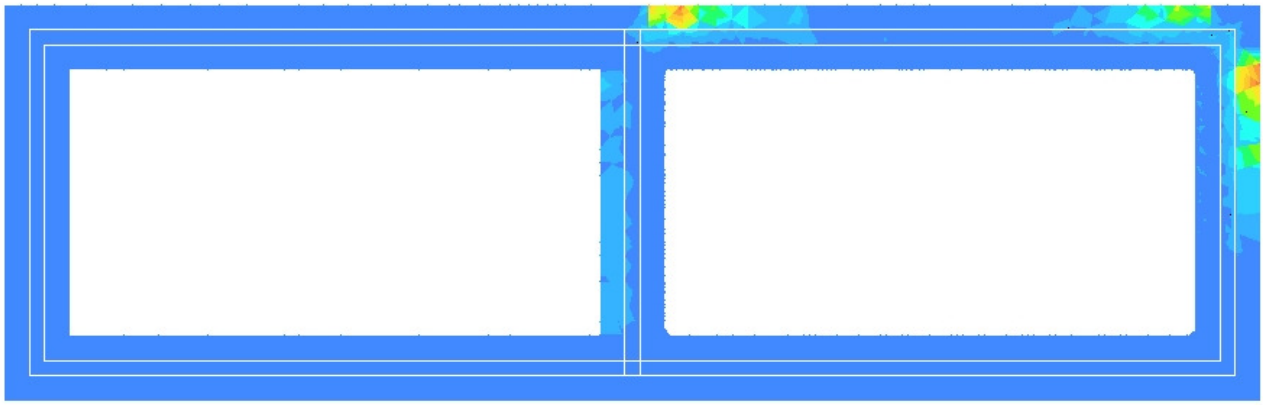

The fictitious crack widths w *after 30 minutes of heating, as predicted by the adapted model.*

As can be seen from the picture, the cracks are not localised as they were in the analysis shown in section 2.5, which makes the plot somewhat less clear, but the essential information can still be derived from it. There are still three main cracks, two in the roof and one in the side wall, with the crack in the roof adjacent to the side wall being noticeably smaller than the other two. Bending cracks on the inside of the element are absent here, probably due to the smaller wall thickness, but this might also be caused by the (relative) temperature ingress being larger, which facilitates bending. The sag in the middle of the roof equals 2.4 mm.

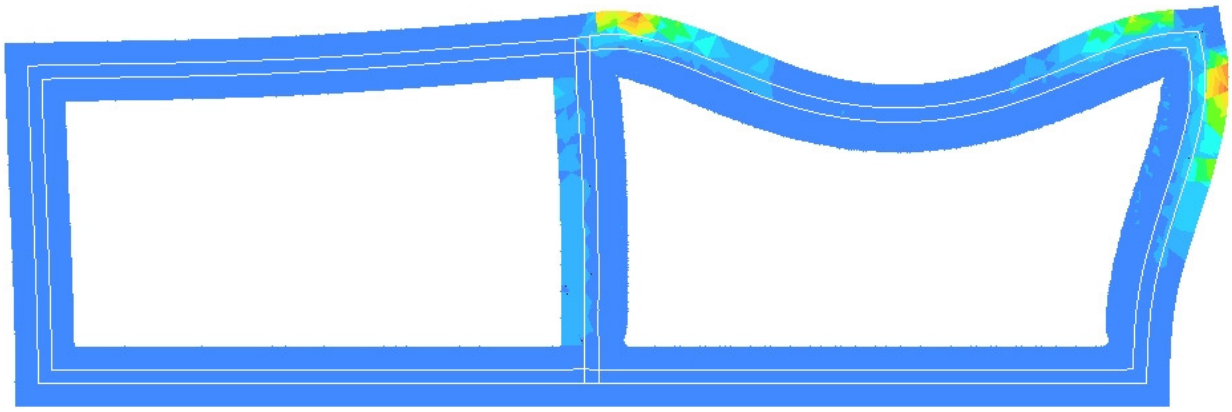

The same fictitious crack widths, with the deformations plotted in the same image.

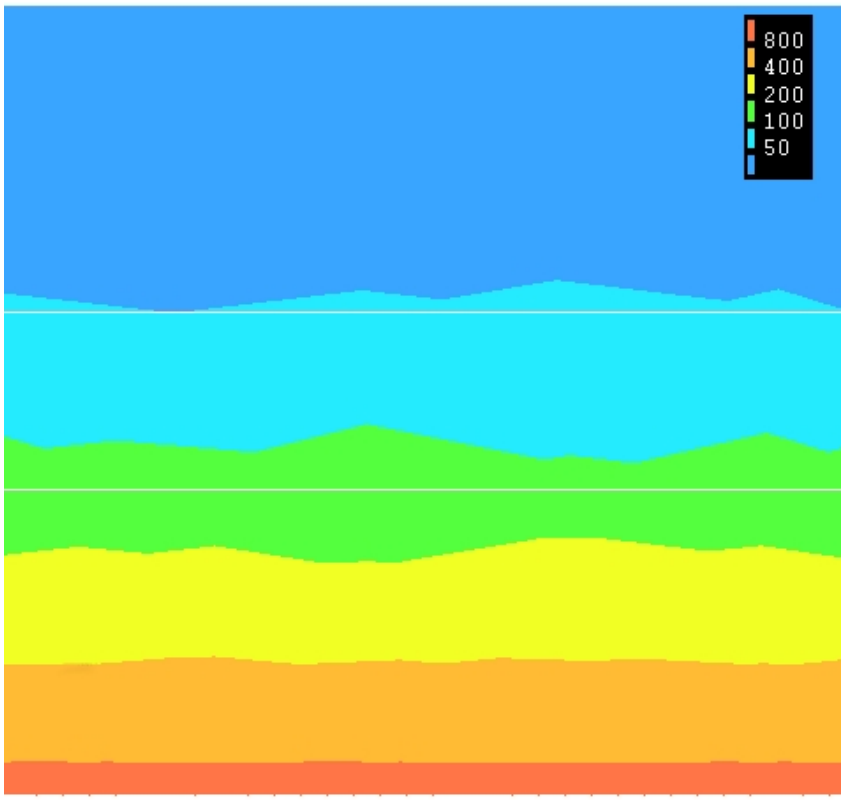

The temperature distribution over the cross section after 30 minutes of heating. The continuous lines represent the reinforcement. The height of the roof is 125 mm.

This means that the tension zone is located (relatively) higher in the cross section, because tensile stresses only develop when an element does not expand enough thermally to facilitate the overall deformation of the roof. When higher temperatures are reached up to a (relatively) higher point in the cross section, it follows that tensile stresses also only start at a (relatively) higher point. The overall shape of the tension band is still the same, although it is more difficult to see because of the shifted location and because softening has taken place in a wider region.

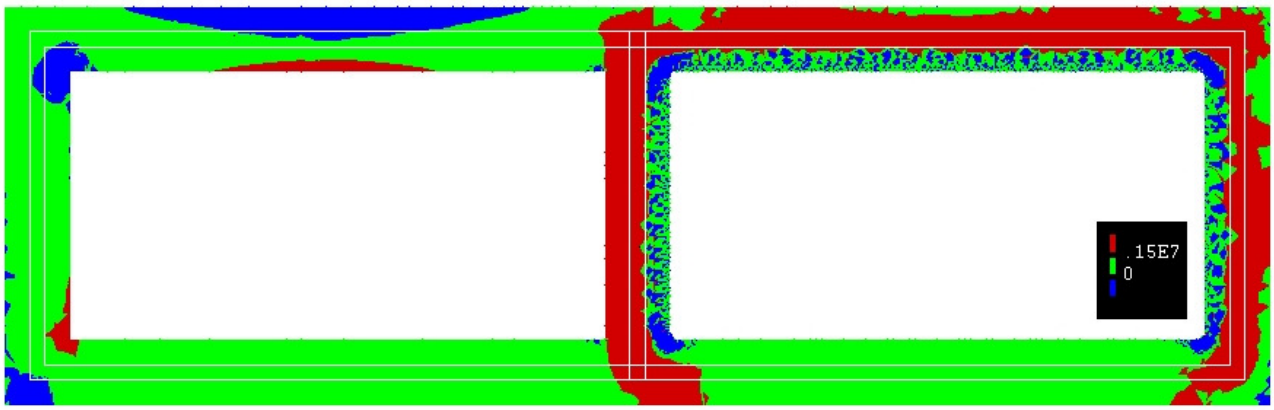

The stress distribution over the cross section after 30 minutes of heating, showing the largest principal value, i.e. tension. The scale is in N/m^2, so the limits used here are 0 and 1.5 N/mm^2 (for a concrete with a reference maximum tensile strength of 2 N/mm^2).

The fact that the reinforcement is located more inwardly compared to an actual size tunnel means that now both the inner and the outer reinforcement develop tensile stresses at the crack locations, with the outer reinforcements reaching the larger values (although this may be difficult to see in the plot), up to 320 N/mm^2.

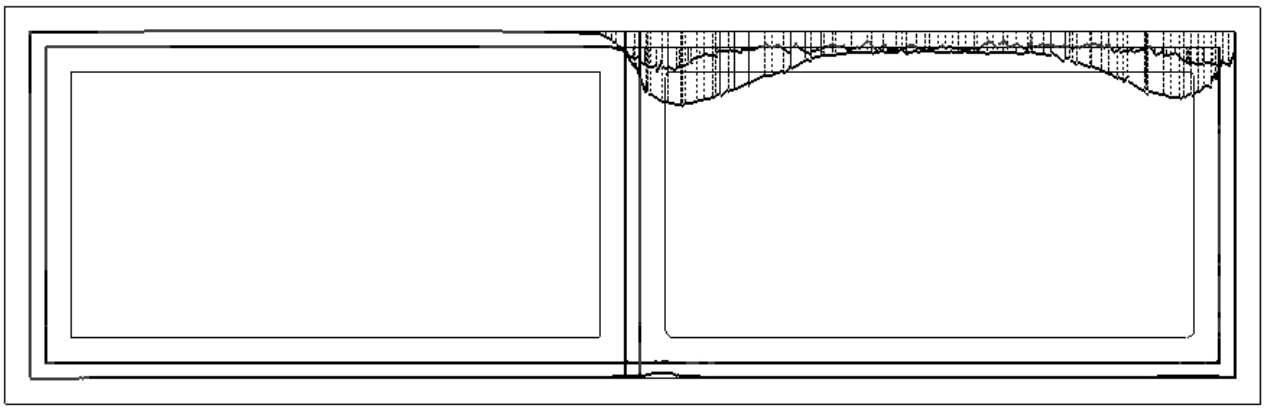

Tensile stresses in the reinforcement after 30 minutes of heating.

In order to assess the crack width it is necessary to summate the fictitious crack widths over the entire width, which gives a graph such as displayed on the next page. The total crack width for the crack in the roof adjacent to the middle wall is then found to be equal to 0.9 mm. It cannot be determined whether this represents a single crack or multiple cracks with some distance in between (a question that would have been answered by the lattice model), but based on experience with the preliminary test, allotting the entire crack width to a single crack seems a reasonable assumption.

Note that these fictitious crack widths are computed using an equivalent element length, which is the diameter of the circumscribed circle of the triangular elements. This relates only to the size of the elements, and not to its orientation. Some elements have a side adjacent to the surface, whereas others only have a tip touching the surface. It can safely be assumed that the principal direction with the largest strain is parallel to the surface in all elements, which means that the crack widths are now effectively summated at various distances from the element surface. This a general problem with smeared cracking that would have been solved if a lattice analysis had been used, but unfortunately that turned out not to be possible, as explained in chapter 3.

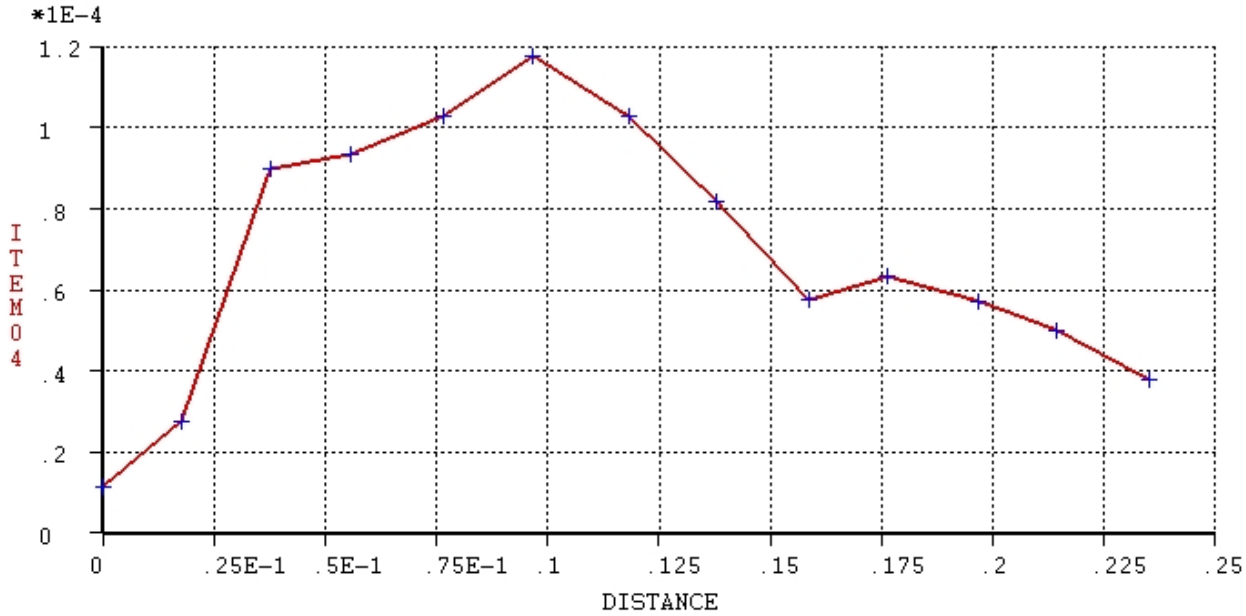

The spatial variation of the fictitious crack width w *in the crack in the roof adjacent to the middle wall, after 30 minutes of heating. These values have to be summated to calculate the total crack width.*

Another problem is that it is now more difficult to plot the relation between crack width and time, because then the crack widths would have to be summated manually at every time step (this cannot be done automatically by DIANA). Plotting the crack width-time relations of every independent element in the same graph is not very enlightening, therefore it is easiest to only plot the width-time curve for the element with the largest resulting value of *w*, although this is not necessarily the element where the crack first developed. The curve for the crack width for the crack in the roof adjacent to the middle wall is then displayed below. Apparently, the crack emerges before completion of the first time step, i.e. within the first 1.5 minutes of heating.

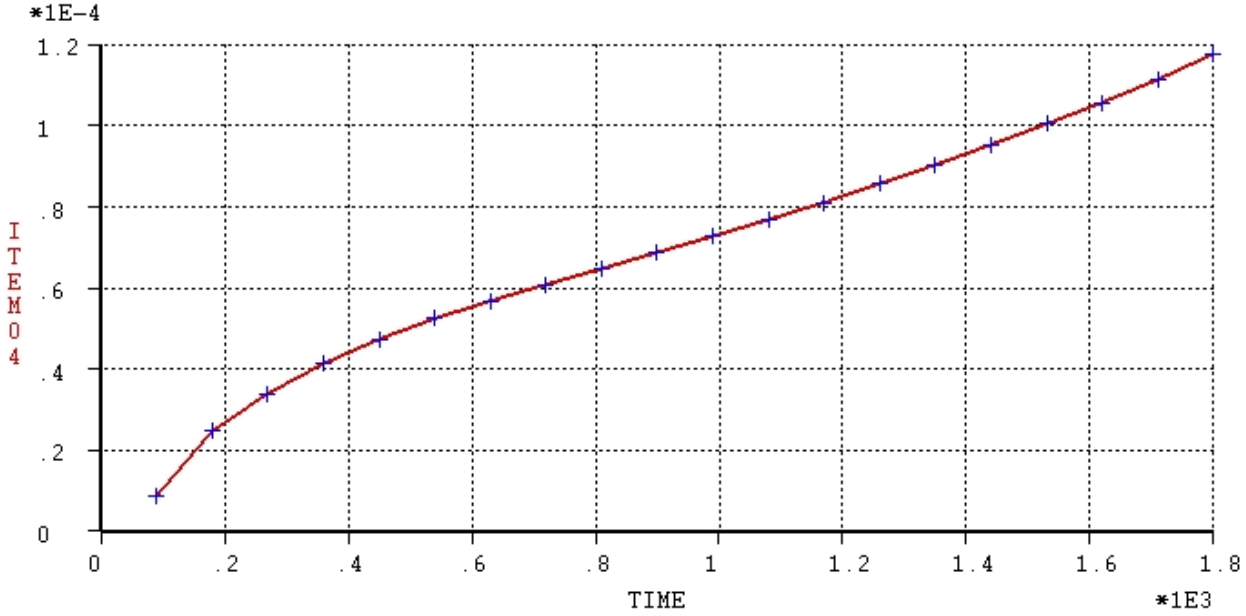

The variation of the fictitious crack width w *with time in one of the elements that constitute the crack in the roof adjacent to the middle wall.*

The same can be done for the two other cracks. The crack in the roof adjacent to the side wall appears somewhat later, but still within the first 3 minutes. This crack reaches a total crack width of 0.7 mm after 30 minutes of heating. The crack in the side wall appears within the first 3 minutes as well; the summated crack width after 30 minutes equals 0.9 mm (similar to the crack in the roof adjacent to the middle wall), but it is possible that this value represents two separate cracks, as there seems to be an additional peak in the graph. In that case, the main crack would only reach a value of 0.7 mm.

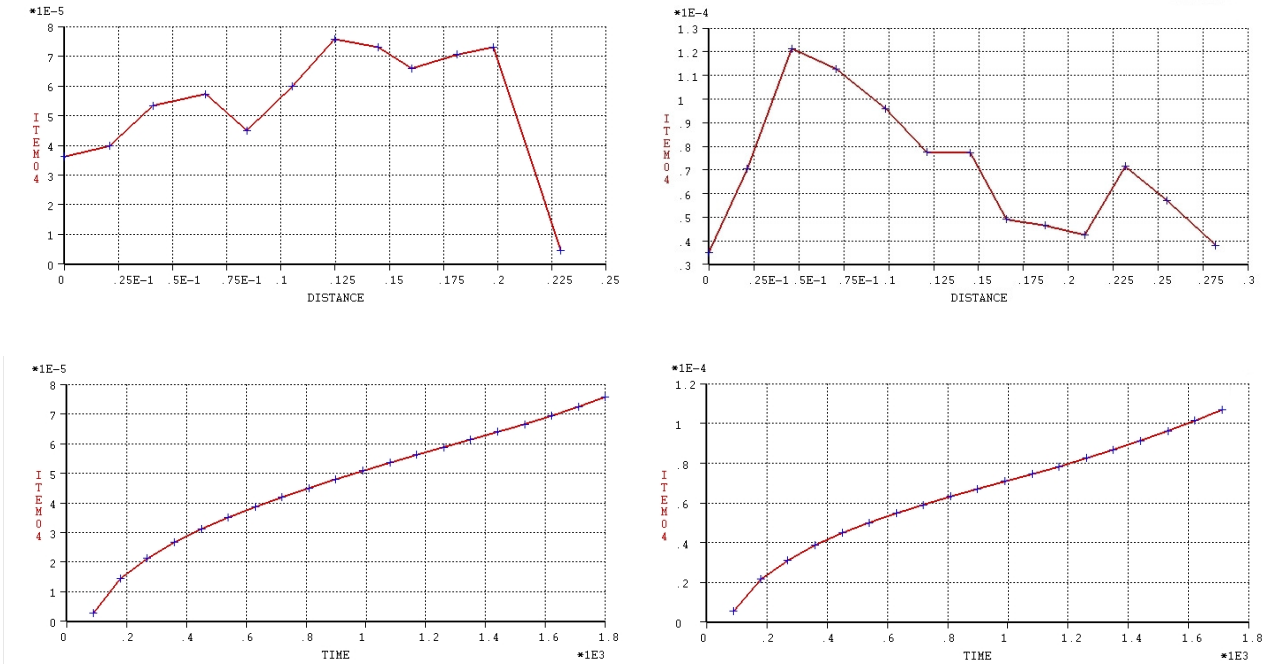

Graphs for the variation of the fictitious crack width w *in space (top) and in time (bottom), for both the crack in the roof adjacent to the side wall (left) and the crack in the side wall just below the roof (right).*

In a number of fire tests fire resistant plates were used, of the type Promatect-H. In an earlier research carried out by Efectis (2007), a computer program was developed that could calculate the interface temperatures between a Promatect plate and concrete based on any external temperature-time relation and plate thickness. The results of this program were used as input for the boundary elements to model the protected tunnels; the fire resistant plates themselves were not modelled explicitly. The actual fire curves used cannot be reprinted in this report because of confidentiality.

Because the calculated temperatures pertained to interface temperatures and not to air temperatures, the convection factor of the boundary elements was set to infinity, and the emission coefficient to unity. With these settings calculations for various plate thicknesses have been made. Because these calculations had to be made in an early stage of the master's thesis, they used an early, limited version of the model. The results are shown on the next page.

The graph shows the approximate predicted time until a crack adjacent to the middle wall will develop. Because the aim was to make a quantitative comparison between the different tests, it was deemed necessary that cracking occurred in all cases, and preferably within a limited time (to reduce the duration of the test). At the same time, the longer the time until cracking, the easier it is to observe variations. As a compromise, a duration of thirty minutes was decided upon, leading to a choice of a plate thickness of 15 millimetre.

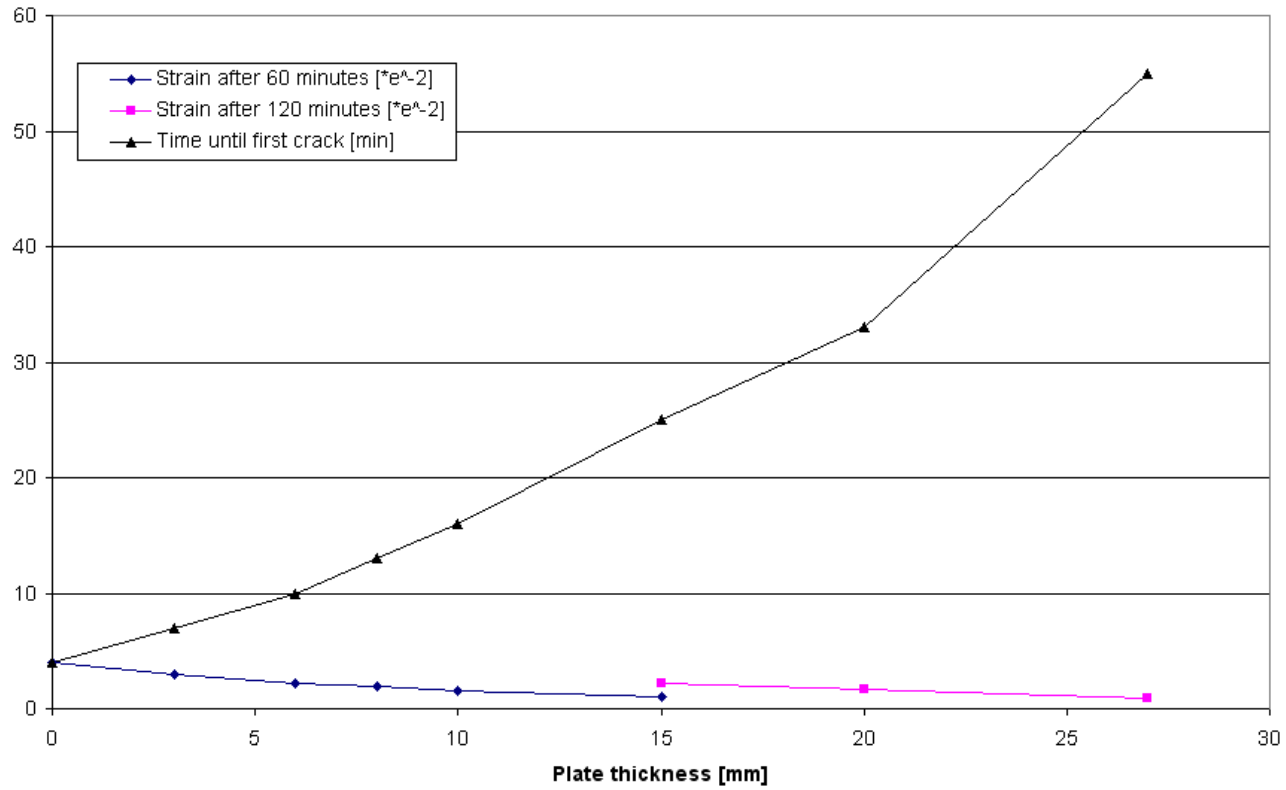

Predictions for the specimen behaviour for various thicknesses of the fire-resistant plates. Because this graph had to be made at an early stage, it shows crack strains (for the crack in the roof adjacent to the middle wall) rather than crack widths, as the latter was not yet implemented.

For the same reason (easy observation of variations), it was decided that the same fire resistant plates should also be applied to the different fibre concretes, although at least one test of a concrete with fibres without a fire resistant plate should be performed for reference. The fibres themselves were assumed not to influence to cracking, therefore no special provisions were taken in the model to account for any effect of fibres (they would, of course, influence spalling, but this is not part of the model).

As the standard screw anchors that would be used for this thickness Promatect plate were deemed to be too long compared to the overall thickness of the tunnel roof, a shorter type of screw was used. To ensure a proper connection, a small hole was made in the plate with a depth of roughly 7 mm, so that the anchor screw had to cover only half the plate thickness. The holes were subsequently filled with a fire-resistant filler (T-compound). Both the roof of the tunnel and the upper 15 cm of the tunnel walls were covered with Promatect-H plates, as would have been done in a real tunnel.

The concrete strength was found to be 37.6 N/mm^2 in a standard compressive cube test. The actual compressive strength that can be input into the model can therefore be assumed to be roughly $0.72 \cdot 37.6 = 27\,N/mm^2$. However, as these tests were performed 28 days after casting, but the actual fire test was performed 100 days after casting (14 weeks), the concrete strength should be assumed to be higher by this point. Therefore, a compressive strength of 30 N/mm^2 was assumed.

As mentioned before, the values used for the temperature curve relate to the surface temperature, rather than to the air temperature. Therefore, the boundary elements on the heated side are made inactive by assuming infinite convection and full emissivity. The boundary elements on the unheated side remain unchanged. The change parameters are summarised in the table on the next page; all other values are identical to the values used in the simulation without fire-resistant plates, as listed at the start of this section.

Concrete properties	
Compressive strength	30 N/mm^2
Boundary element properties (heated side)	
Convection factor	1×10^9 (i.e. infinity)
Emissivity	1

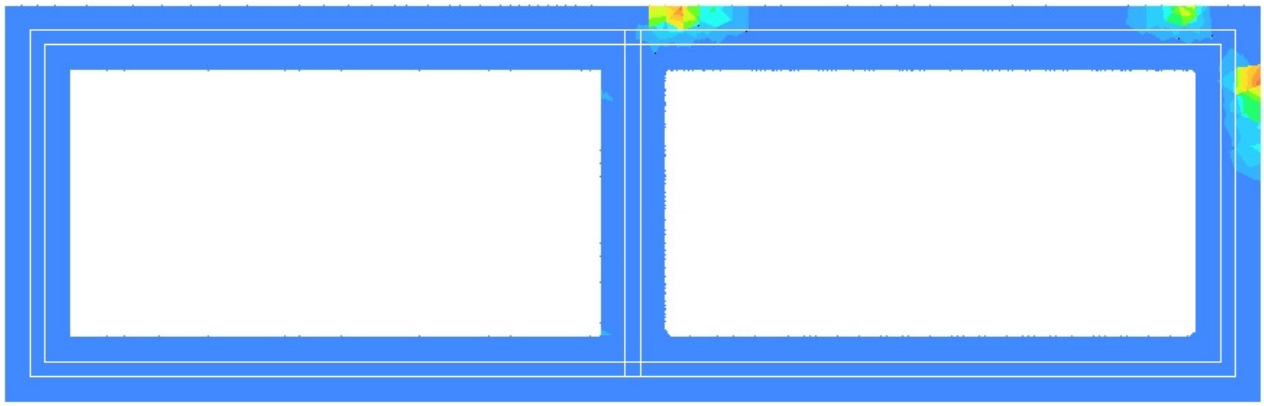

Predicted values for w *after 30 minutes of heating with 15 mm fire-resistant plates.*

The results of the simulation with 15 mm Promatect-H plates are shown in the above plot. As can be seen, the cracks are more localised now, but the summated crack width is smaller (which is, of course, an expected consequence of applying fire-resistant plates). This cannot be seen in the above picture (because the scale has been redefined), but only in a plot of the fictitious crack widths *w* in space and time. The sag is smaller as well, equalling only 0.4 mm.

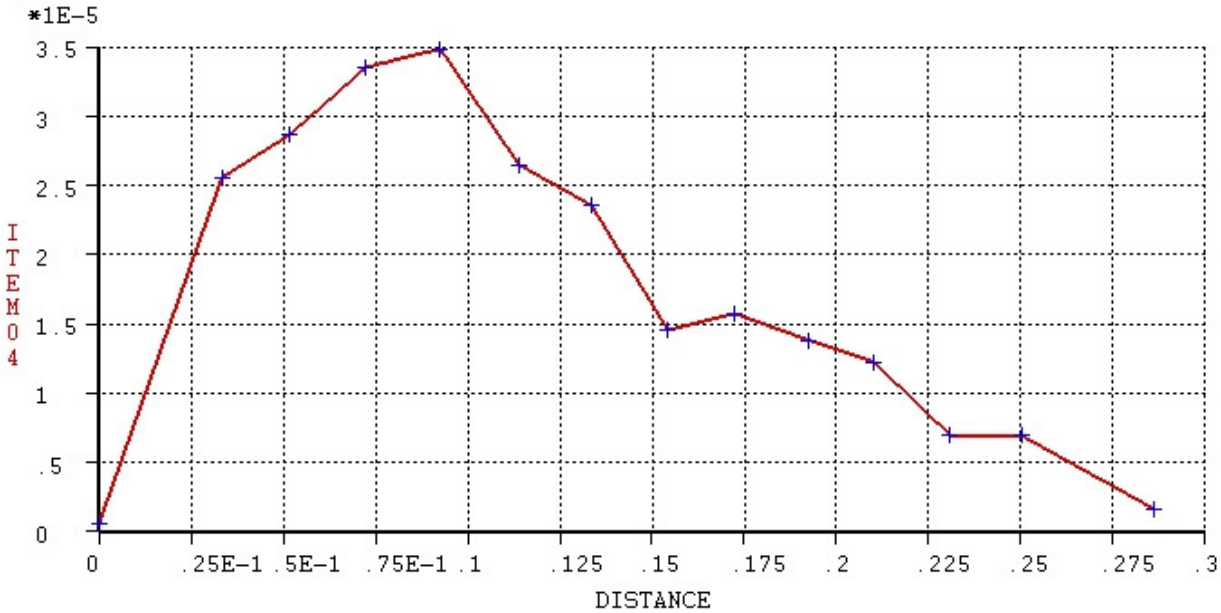

The spatial variation of the fictitious crack width w *for the crack in the roof adjacent to the middle wall after 30 minutes of heating with 15 mm fire-resistant plates.*

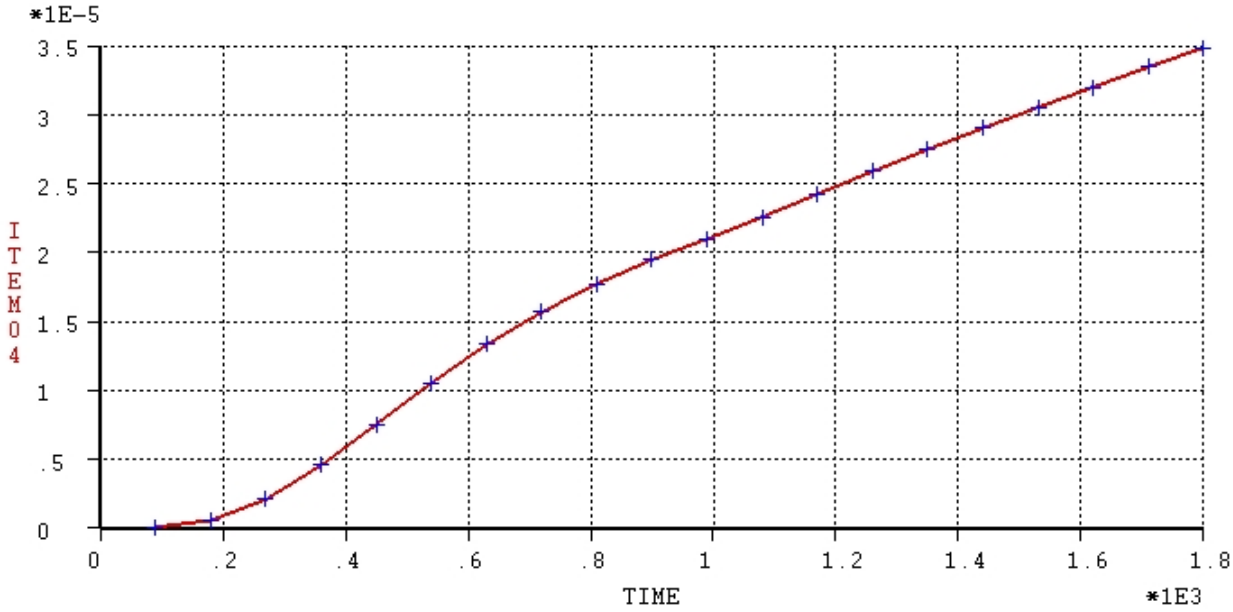

The development of the fictitious crack width w *in one element with time for the crack in the roof adjacent to the middle wall for a simulation with 15 mm fire-resistant plates.*

As can be seen from these graphs, the crack emerges after roughly three minutes. After 30 minutes of heating, it reaches an eventual crack width of 0.2 mm (compared to 0.9 minutes for an unprotected specimen). Note that this value is only valid if it is assumed that these fictitious crack widths all pertain to the same actual crack (rather than to two parallel cracks), an assumption that does not necessarily follow from the preliminary test.

4.3 Test results

Although in total twelve specimens were cast, it was decided to use only a limited number of these for an initial series of tests. Afterwards, an evaluation would be done which further tests would be necessary, after which a second series of tests could be performed. The remaining specimens could also be used as spares in case unforeseen problems arise during a test in the initial series. Unfortunately, any second series would take place at too late a time to be incorporated into this master's thesis, so this section will be limited to the initial series.

The preliminary test was 'repeated' as part of the full test series, so that is was performed on an actual specimen (the specimen in the preliminary test being discarded and being only one month old), but the result was largely identical (suggesting that maturity between one and three months as a negligible influence). Cracking occurred after five minutes in the form of a crack on top adjacent to the middle wall, running over the entire length of the specimen. This crack eventually reached a width of 0.9 mm (after thirty minutes of heating). A crack adjacent to the side wall emerged simultaneously, but this crack would only reach a width of 0.5 mm.

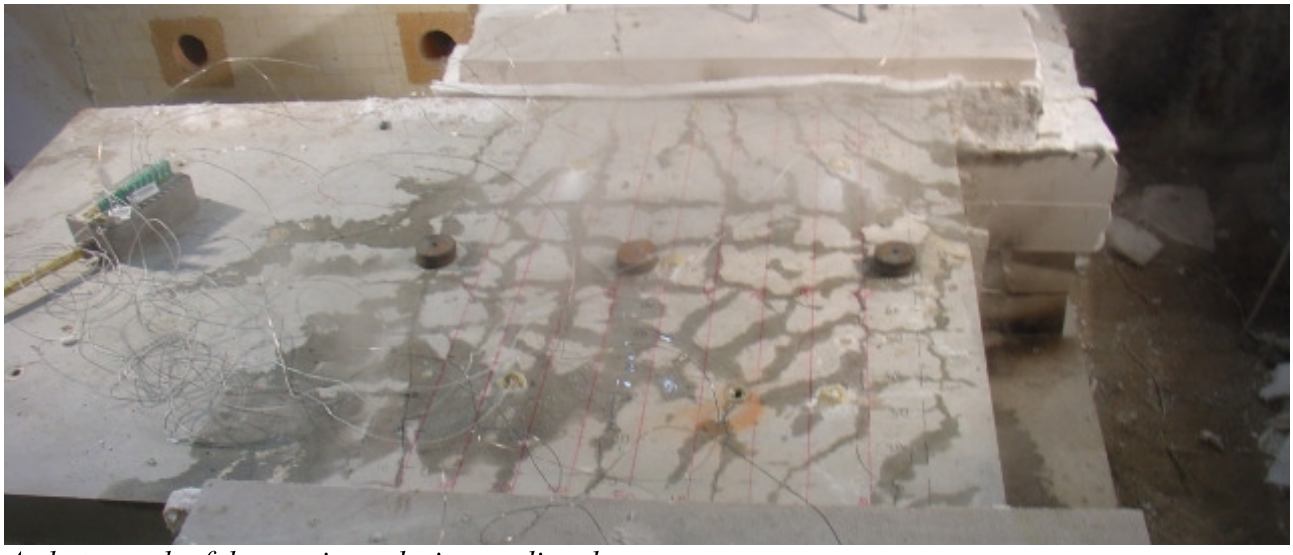

A photograph of the specimen during cooling down.

The horizontal crack pattern on top emerged after eight minutes, with water emerging from these cracks after roughly ten minutes. A crack on the side wall of the specimen, about 10 cm below the top, was observed only after nineteen minutes; this crack eventually reached a size of 0.7 mm (after thirty minutes). Deformation measurements showed that the connection between the roof and the middle wall (point A) has moved upwards 3.1 mm at that point, and the connection between the roof and the side wall (point C) 3.7 mm, both due to elongation of the walls, but on one side restrained by the unheated tube. Halfway the span (point B) the upward movement is 1.5 mm, which means a net sag of 1.9 mm.

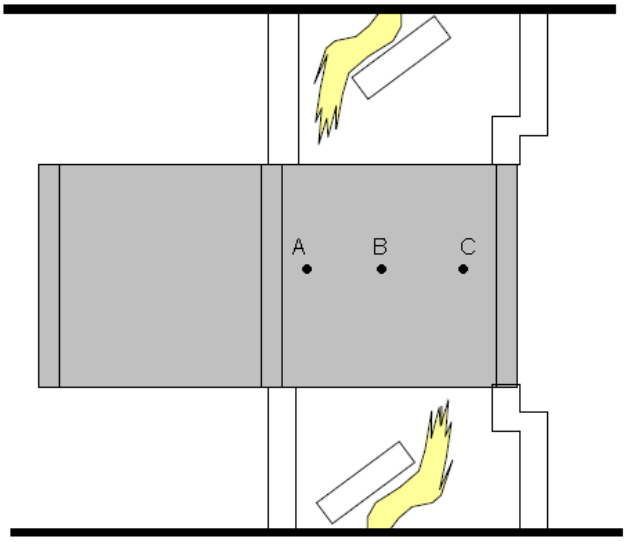

A schematic showing the location of displacement measurers A, B and C.

This test was then repeated for a concrete with fibres of 18 µm in diameter and 12 mm in length (the most often used type of fibre). Although it was expected that would not influence the cracking on the unheated side, cracks were actually found to be smaller than in the previous test. The crack on top adjacent to the middle wall reached a size of only 0.4 mm after thirty minutes of heating. The crack was first observed after six minutes, suggesting that the time until cracking was not or hardly influenced. A smaller crack adjacent to the side wall appeared after 17 minutes.

The specimen with fibres 18 µm in diameter and 12 mm in length after 30 minutes of heating. Note the relative scarcity of water compared to the test without fibres.

A major difference when compared to the first test was that initially hardly any water emerged from the cracks, probably because the voids and channels left by the fibres upon melting created a room where the water could temporarily be stored. Moisture first appeared after 11 minutes on equidistant cracks perpendicular to the middle and side walls, but the amount was far less than in the first test. Upon further heating, the water reached boiling temperature as it did in the first test, but even in this stage the amount of moisture was limited compared to the first test.

The elongation of the walls was found to be smaller than in the previous test, with a displacement of 2.1 mm upwards being found for both points A and C. Point B underwent an upwards displacement of 0.5 mm, which corresponds to a relative sag of 1.6 mm, roughly the same value as in the previous test. This is remarkable because the cracks are smaller, whereas one would expect a linear relationship between sag and crack width.

A third test was carried out with a concrete with fibres 18 µm in diameter and 6 mm in length, protected by a 15 mm Prometect-H plate. Unfortunately, this test showed an 'incorrect' mechanism of the roof bending upwards rather than downwards, with point B showing the highest upwards displacement of 2.3 mm, compared to 1.4 mm in point A and 2.0 mm in point C (after thirty minutes of heating). Apparently this mechanism was made possible by the small thermal gradient (because of the fire-resistant plate) in combination with the small thickness.

This is, of course, the same mechanism that was predicted in the initial attempts with the finite element model (see section 4.2), but was discarded because it did not correspond to the preliminary test results (nor to any subsequent test without fire-resistant plates), but apparently it is the occurring scenario in this specific test. This is problematic because very little can be learned from this mechanism: there are hardly any cracks (only equidistant bending cracks, but they are very small), and the situation does in no way correspond to an actual tunnel (even with a very thick fire-resistant plate, the large thickness of the walls will always cause inwards bending).

The solution to this, by analogy to the simulation, would be to put an actual loading on the specimen, so that downward bending is forced. Therefore, a number of street tiles was placed on the specimen during the next fire test (a different specimen with fibres 32 µm in diameter and 12 mm in length), but this did cause a change in mechanism. Because the FEM simulation already predicted upwards bending for the unprotected specimens (which was not the case in the experiments), the model cannot be used to accurately predict the necessary load, although the of 0,1 N/mm^2 might at best be an overestimation.

That said, a value in that range might be low when compared to concrete strength, but it is quite high when it has to be achieved using dead weight alone, especially when the dead weight has to be concentrated rather than spread out, in order to keep the crucial parts of the specimen uncovered, so that cracks could still be observed here. After numerous considerations, an elaborate construction consisting of eight stacked leftover concrete blocks was decided upon, totalling 7560 kg and being two meters in height.

The blocks were laid perpendicularly to the tunnel side and middle walls, which meant that they would lose contact with the span of the roof as soon as it would start to sag, being supported only by the walls. Because the elongation of the roof would cause any bending to continue (whether it be an upwards of downwards bending), this should be enough to ensure the proper mechanism taking place. The measured deformations are then the 'true' deformations related to the temperature, and no longer influenced by the loading. To avoid wasting another specimen, the specimen from the second test was recycled. It was rotated 180 degrees so that the (damaged) roof became the bottom, and the previously unheated tube could be heated.

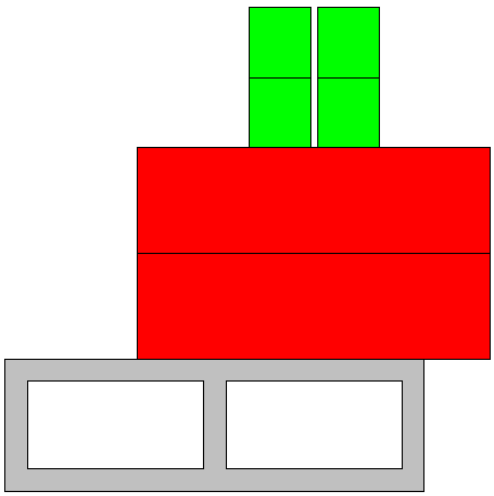

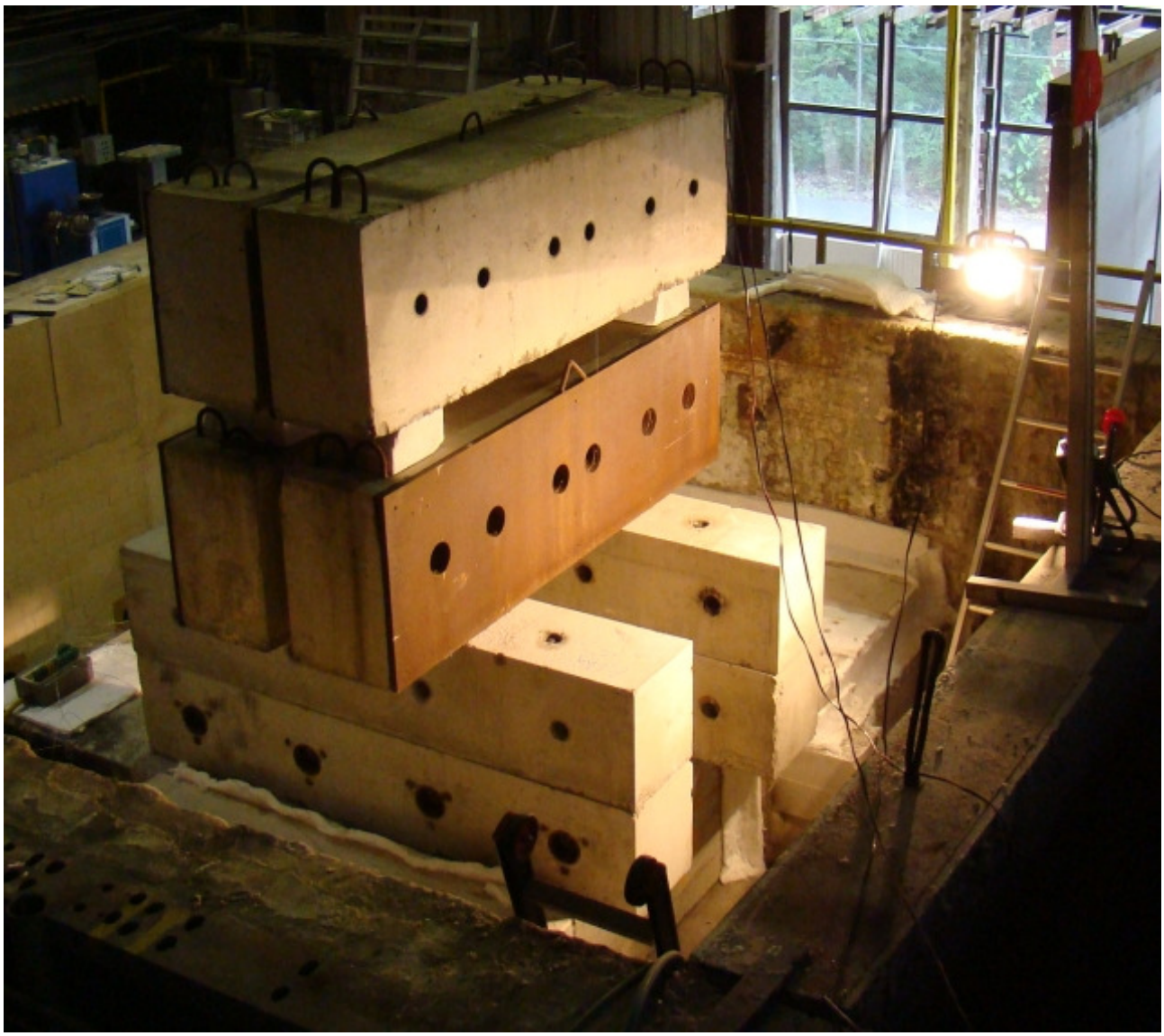

The construction of blocks used to put load on the specimen. The specimen itself is somewhere below all this.

Unsurprisingly, this specimen showed smaller deformations, with points A and C moving 0.9 mm upwards, and point B moving 0.5 mm, a relative sag of 0.4 mm after thirty minutes of heating. After 100 minutes, the upwards movement of all points has increased to 2.0 mm in A, 1.9 mm in C and 1.5 mm in B, a relative sag of 0.45 mm, hardly an increase.

It was difficult to observe cracks during this test, partly because the blocks blocked over half of the surface area of the roof, and partly because the instability of the towering construction meant that the specimen could not be approached. This formed an impractical combination with the fact that this (recycled) specimen contained fibres, which meant that cracks would be largely dry. Only after 30 minutes were moist cracks seen on the side wall, and only after 35 minutes a dry crack appeared on top adjacent to the middle wall. After 57 minutes, moisture appeared from under the blocks, but it was not until 76 minutes after the start of the test that moisture emerged from the crack adjacent to the middle wall.

Only the small surface area between the blocks remained free for assessing crack widths.

By that time, several other cracks had formed on top. After 61 minutes a crack perpendicular to the side and middle walls appeared, running the length of the span. The concentration into one central crack in this direction is most likely related to the loading blocks being placed on either side of it, whereas in previous (unloaded) tests there were 'spread out' equidistant cracks in this direction. After 64 minutes a longitudinal crack formed adjacent to the side wall. All cracks were very small throughout the test, probably never widening beyond 0.2 mm (although no cracks were measured, because the specimen could not be approached).

The observed phenomena correspond well to the expectations from the FEM simulation and the general functionality of fire-resistant plates, the only exception being the perpendicular crack which is now concentrated due to the load placement, but this direction is not considered (in reality, it would make a difference whether the fire would break out in the middle of a tunnel section, or exactly beneath a connection between two sections, the latter probably allowing a rotation without bending of either of the sections).

Although the test was, in this respect, successful, it was not repeated because building and removing the loads was thought to be too time consuming to fit in the original time schedule, and the cracks were very difficult to observe (an important objection if visual inspection is to be the prime means of gathering information during a test). It is as yet unknown whether further tests will be undertaken in a second test series, and if so, how they would be organised, but either way it would not be possible to incorporate them into this master's thesis. This is unfortunate because at least a test on a concrete with fire-resistant plates but without fibres should be carried out for a proper comparison.

4.4 Interpretation

Because of the large difference between an actual size tunnel and a scaled specimen, particularly for an effect that is caused by the thickness of the roof, the results of the fire tests should not directly be translated to real tunnels, but can only be used for validation of the finite element simulation. In this respect, the results of the fire tests should be seen as very positive, as they show a good correlation with the predicted results. For the unprotected specimen, a comparison is shown below.

Time	**Crack width**			
Roof, adjacent to middle wall		**Roof, adj. to side wall**	**Side wall, below roof**	
<1.5 minutes	0.9 mm	0.7 mm	0.9 mm	**Predicted**
~5 minutes	0.9 mm	0.5 mm	0.7 mm	**Observed**

As can be seen, the predictions for the crack widths are in general very close to the observed values. Only the time until cracking is an important underestimation, but this may be caused by the fact that it is very difficult to observe a (dry) crack until it has reached a certain size (theoretically, the crack starts as a microcrack, which cannot be observed yet). This means that it is quite possible that the predicted time until cracking is actually very close to the actual value, but the observed value is an overestimation.

It is also of interest to compare the deformations in the points A, B and C (see schematic in section 4.3). As can be seen from the table, the general upward movement of the specimen is greatly underestimated, but the prediction for the net sag (which most closely relates to the crack width) is reasonably accurate. The underestimation of the upwards movement might be related to the incorrect modelling of the biaxiality of LITS, as explained in section 2.4.2.2, as well as to the added 0,1 N/mm^2 load that was used to correct the initial incorrect prediction. The boundary conditions may also have an influence here.

Point A	**Point B**	**Point C**	**Net sag**	
+0.8 mm	-1.5 mm	+1.0 mm	2.4 mm	**Predicted**
+3.1 mm	+1.5 mm	+3.7 mm	1.9 mm	**Observed**

Contrary to the expectations, the fire test has shown that PP fibres have a significant influence on the crack width, reducing it from 0.9 mm to 0.4 mm (for the crack in the roof adjacent to the middle wall). The reason for this unclear; it might be related to the smaller pore pressures, but then the model (which ignores moisture transport and pore pressure) should match with the specimen with PP fibres rather than with the unprotected specimen, which it clearly does not. In addition, the sag of the roof seems hardly influenced by the addition of PP fibres, suggesting that only the crack size is influenced, and not the deformations.

Most likely, the difference in crack size is caused by a different moisture content, which cannot be explained by the model because the moisture content is not a parameter there (although implicit assumptions have been made, as explained in section 2.4). Apparently the assumed moisture content matches the actual moisture content in the unprotected specimen (although this value was not measured), but deviates from the moisture content of the specimen protected with PP fibres. If this influence is to be analysed, a different kind of model would be required.

It is noteworthy that there is significantly less water emerging from the specimen with PP fibres. In the unprotected specimen, water inside the concrete will expand upon heating and evaporate, and subsequently move away from the heated region because there is not enough room in the concrete. The vapour will condensate again at some distance from the heated region, because by that point temperatures will have dropped sufficiently. This moisture transport will eventually involve emergence of water on the unheated surface. In the specimens with PP fibres, there are voids and channels created upon melting of the fibres, where the water vapour can move instead.

For the specimen with fire-resistant plates, it is very difficult to compare values between the fire test and the FEM model, because the specimen could not be approached. The crack in the roof adjacent to the middle wall was only observed after 35 minutes, whereas it should have emerged after only 3 minutes according to the model, but it is very likely that the crack had been present for a long time before it was observed. Further problems arise from the blocks themselves blocking part of the roof surface (if the crack did not start in the middle, it would not have been observed), and from the fact that the specimen also contained PP fibres, which clearly has an influence as well. That said, the predicted value of 0.2 mm crack width after 30 minutes of heating seems to match the (eventually) observed crack width for the crack in the roof adjacent to the middle wall.

Compared to the crack properties, the deformations can be compared with relative ease. Again, the general upward movement of the specimen is underestimated, but the prediction of the net sag appears to be very accurate. As the latter value is the most influential on the crack, this should be seen as a good approximation. During testing, it was observed that the unheated tube also moved upwards, becoming loose from the floor. This is not possible in the FEM model because of the boundary conditions, creating an additional restraint that most likely causes the difference in predicted upward movement.

Point A	**Point B**	**Point C**	**Net sag**	
+0.1 mm	-0.3 mm	+0.2 mm	0.5 mm	**Predicted**
+0.9 mm	+0.5 mm	+0.9 mm	0.4 mm	**Observed**

In conclusion, it would seem that the model has a good predictive value for behaviour of the specimen, although the deviation caused by the addition of PP fibres cannot be explained (nor can this be expected of the model, as no function of these fibres is implemented). From a statistical standpoint, it would be desirable to perform more test to assess the reproducibility of these values, but based on the information presently available, the model seems adequately accurate. It would therefore be reasonable to assume that the model is also adequately accurate for an actual size tunnel, although this is an extrapolation.

5. Sensitivity analysis

Because the result of any computer simulation is of course highly dependent on its input values, it is necessary to analyse the sensitivity of the the result to a variation in a specific parameter. However, it would be impractical to test the influence of all parameters, because a number of parameters are input as curves or tables, which cannot be expressed as a single parameter. This sensitivity analysis will therefore be limited to a number of well-defined parameters, which are expected to be of great influence. All results pertain to the model described in chapter 2 (the mesh representing an actual size tunnel).

For the purpose of this sensitivity analysis, a single output parameter has been chosen to be compared, rather than showing and analysing plots of different parameters in space and time for each variation of the input parameters. While it might at first seem that the (largest) resulting crack width would be the obvious choice for such a parameter, this is not the case, as this value can often not be easily determined from the DIANA output. For some (smaller) values of input parameters, the output clearly shows two parallel cracks in the roof adjacent to the middle wall, whereas others show only one crack.

A large number of simulations, however, show only a large region over which the fictitious crack widths are spread out (see for example the figure on page 61, although that pertains to a different mesh), making it unclear whether the summated crack width should be divided over two separate cracks, or be understood to relate to only a single crack. Although the crack spacing can be estimated from the reinforcement ratio and diameter, this is difficult to apply because the crack widths are not evenly distributed over a fixed width (rather, there is often a bell curve), which makes results obtained this way particularly inexact.

In addition to this, the resulting crack width is influenced by more parameters, including the problematic value of w_c, for which larger values than what would be realistic have to be used to ensure stability. This means that the resulting crack width cannot be unequivocally assessed, and therefore it is not a suitable parameter for comparison in a sensitivity analysis. Of course, the actual crack width was intended to be determined using the lattice analysis, but, as explained in chapter 3, this turned out not to be possible.

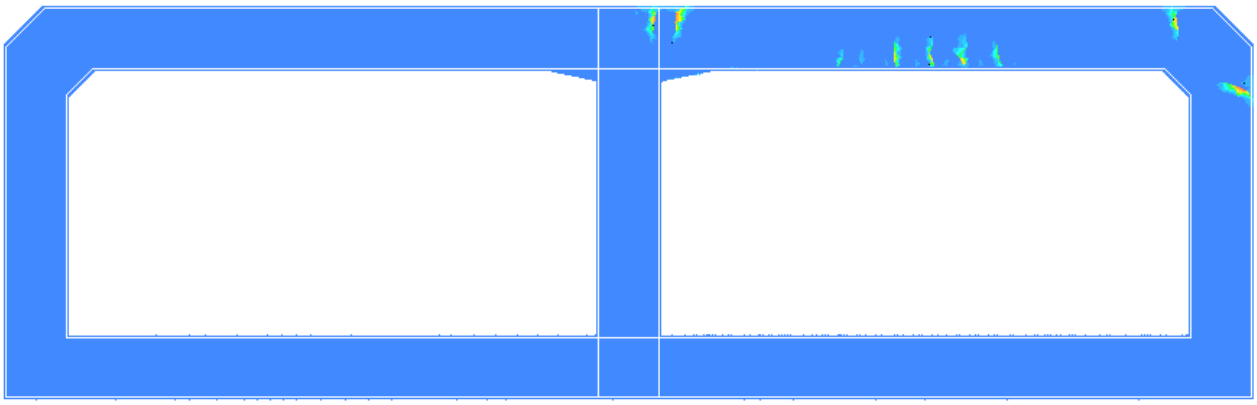

A plot of the fictitious crack width w clearly showing two parallel cracks in the roof adjacent to the middle wall. This plot has been obtained for a compressive strength reduced to 15 N/mm^2.

It should also be pointed out that while the Rijkswaterstaat curve has an arbitrary length of two hours (although sometimes a three-hour version is used as well, created simply by keeping the temperature constant for another hour), a natural fire in an actual tunnel might continue for a longer time. Therefore, the crack width after two hours is not necessarily the maximum crack width occurring during a fire (and, in addition to that, the resulting crack width is also modified by the behaviour during unloading, which is currently not implemented in the model).

Instead, the time until the first crack appears in the specimen has been chosen (in particular, the crack in the roof adjacent to the middle wall, which was always the first crack in all simulations). This value can easily and unequivocally be determined from the analyses, and is an indirect measure of the resulting crack width (if it takes longer before the first crack appears, the resulting crack width at a fixed point in time will always be smaller). It is not influenced by uncertain parameters such as w_c, making its values more usable for comparison. Specific variations in the resulting crack width will still be mentioned for the particular comparisons, but they are not plotted in the graphs.

Values obtained from the analyses performed for this sensitivity study are marked with diamond symbols in the graphs. The straight lines connecting them are only added to aid the user in reading the graphs, and are not intended to establish a definitive relationship.

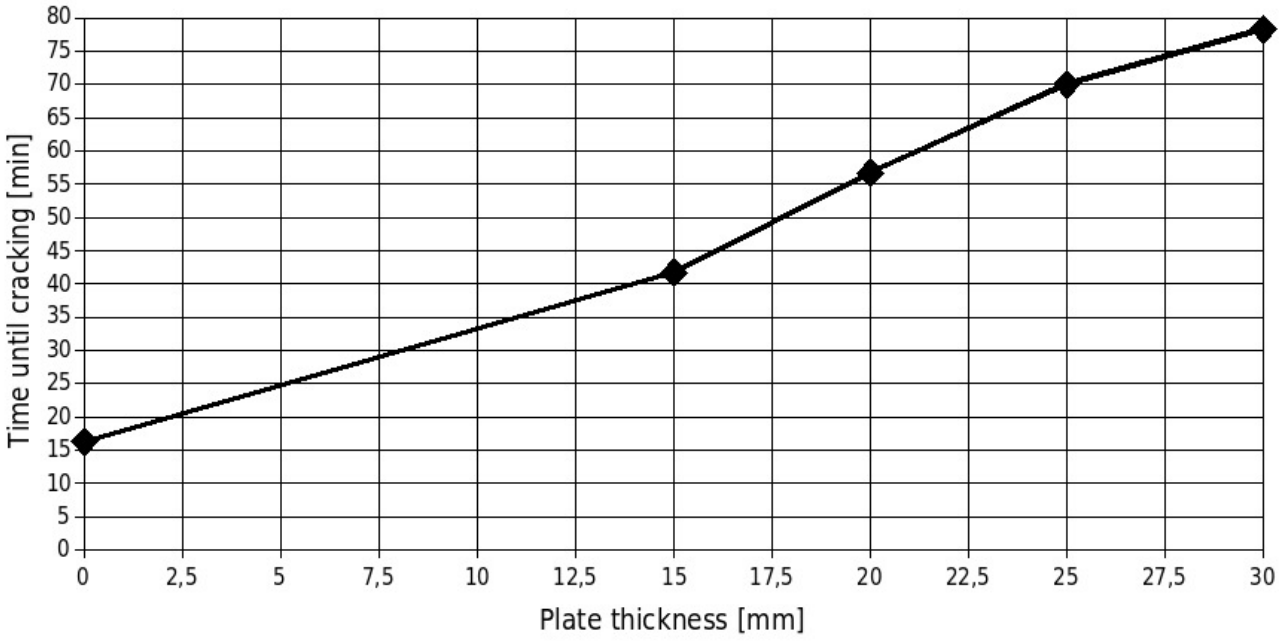

As was to be expected, the thickness of the fire-resistant plates has a large influence on the time until cracking occurs, easily delaying the crack onset until 70 to 80 minutes after the fire has started (27 mm being the most commonly used thickness). It will be clear that this also means that the resulting crack width after, for example, 120 minutes will be far lower for higher plate thicknesses, although the rate with which the crack widens seems to be slightly higher for thicker plates. For other analyses in this sensitivity study, an absence of fire-resistant plates has been assumed.

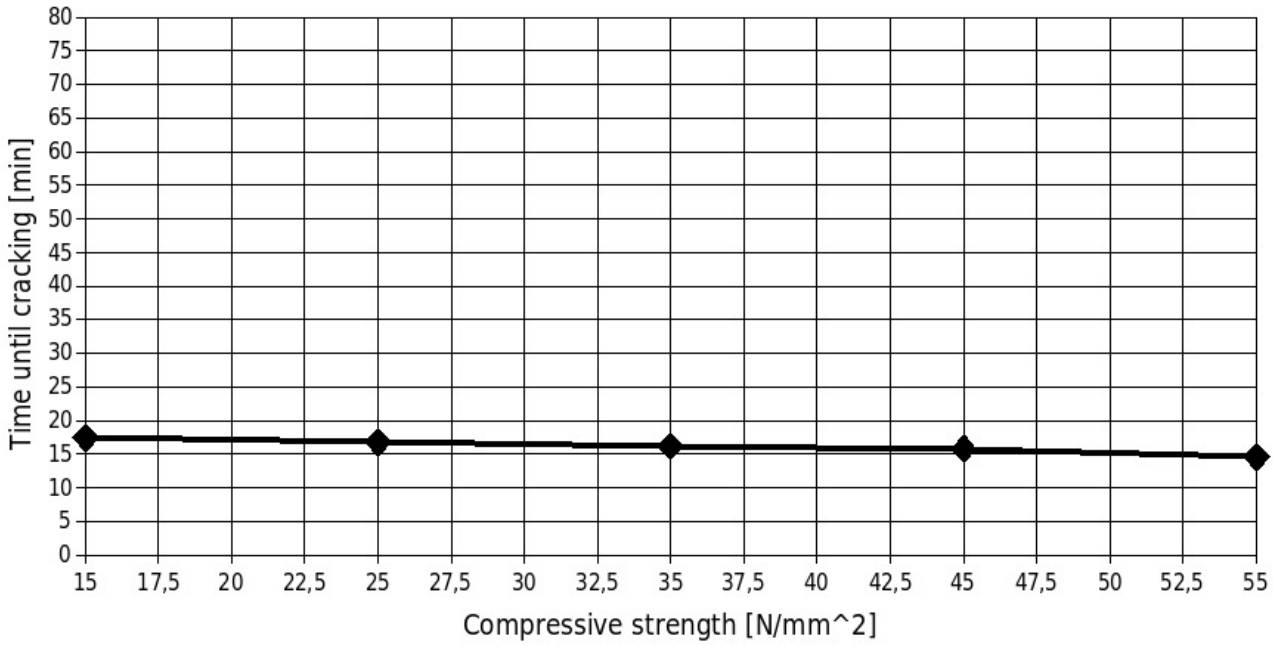

As can be seen in the above graph, the reference compressive strength of the concrete has a minor influence, with larger strengths leading to slightly earlier cracking. The inverse proportionality is probably caused by the fact that a smaller compressive strength causes an earlier onset of the softening phase, which can compensate for the thermal expansions. The subsequent rate of crack widening seems hardly influenced.

It should also be noted that, if tensile strength and compressive strength are treated as separate variables (in reality they are typically linked), an increase in compressive strength means a decrease in the strain at peak stress in tension (because the Young's modulus decreases but the maximum compressive strength remains constant). This means that larger tensile strains can be accommodated before a crack emerges, which is also a possible explanation of the observed inverse proportionality. Note that this graph only pertains to the compressive strength at 20 ºC; the relative decrease of this parameter with temperature is kept constant (as described in section 2.4.2.3). For the other analyses in this sensitivity study, a compressive strength of 35 N/mm^2 was assumed.

In contrast to the compressive strength, the reference tensile strength clearly has a large influence on the time until cracking (in reality these parameters are typically linked, but for the purpose of this sensitivity analysis, they are considered separately). It is, of course, easy to see why: a crack will only develop once the tensile strength has been exceeded, so the higher the tensile strength, the longer it will take before the crack emerges. For a tensile strength of 5 N/mm^2, no crack will develop within the first two hours of heating. The rate with which a subsequent crack widens seems hardly influenced. For the other analyses in this sensitivity study, a tensile strength of 2 N/mm^2 has been assumed.

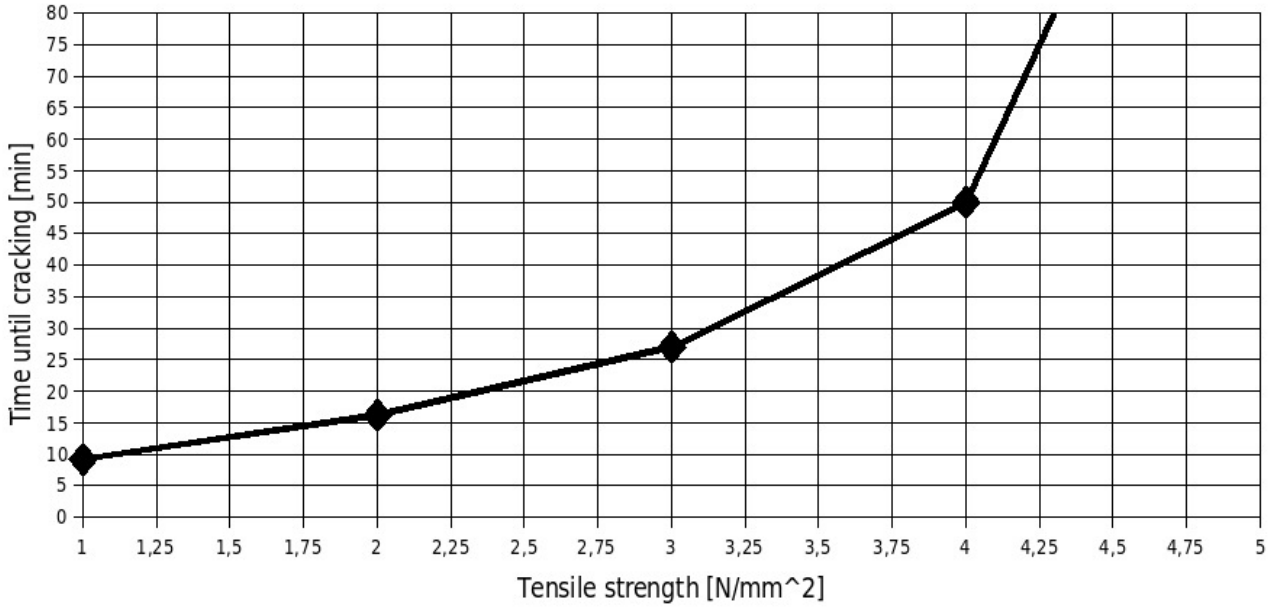

The cross sectional area of the inner reinforcement (i.e. the reinforcement close to tubes) seems to have a minor influence on the time until cracking, with larger values leading to slightly earlier cracking. Because this reinforcement is in compression during heating (as explained in section 2.5), it does not limit the deformation of the expanding concrete. In fact, because the thermal expansion of steel is slightly higher than the thermal expansion of concrete (for most temperatures), the presence of the reinforcing steel would seem to increase the deformation of the tunnel roof and walls. This is probably the cause of the observed inverse proportionality. The rate with which the crack widens appears to be uninfluenced by this parameter. For the other analyses in this sensitivity study, an inner reinforcement area of 3272 mm^2 has been assumed (corresponding to ø25-150 mm).

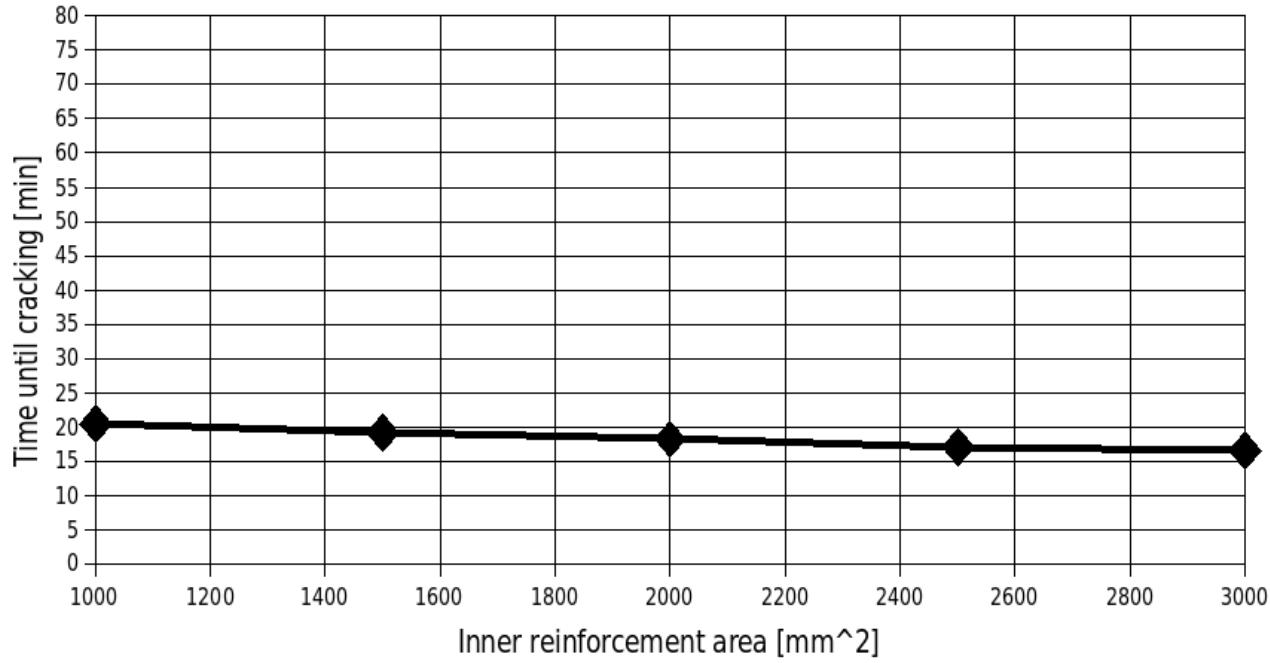

The cross sectional area of the outer reinforcement (i.e. the reinforcement close to the tunnel surface) also seems to have a minor influence on the time until cracking, but with the time until cracking increasing for increasing areas. However, the outer reinforcement area clearly has a very large influence on the subsequent rate with which the crack widens, and therefore on the resulting crack width. This is, of course, a well-known and extensively described effect of reinforcement that hardly needs elaboration here (and, because the reinforcement is located near the tunnel surface, it is uninfluenced by temperature effects).

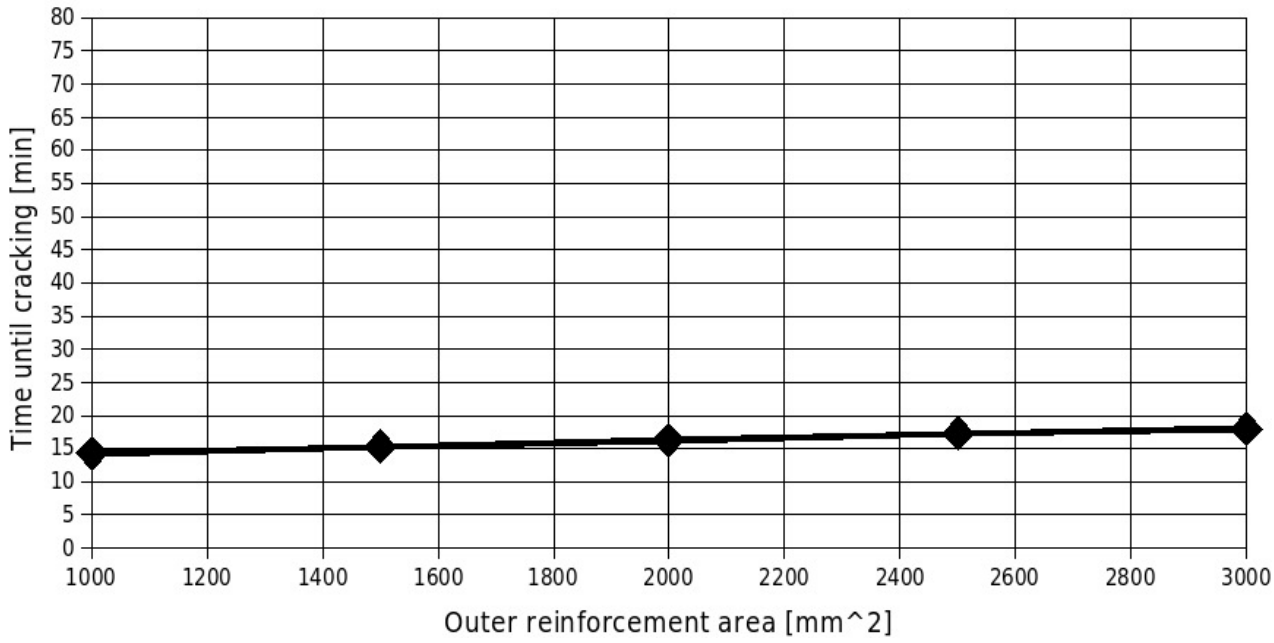

In can therefore be concluded that there are three properties that have a large influence on the resulting crack width: the thickness of the fire-resistant plates (if present), the tensile strength of the concrete (both merely delaying the crack initiation), and the cross sectional area of the outer reinforcement (limiting the rate with which the crack widens once it has opened). For actual purposes, of course, the tensile strength seems a less feasible parameter to select for improvement, leaving the outer reinforcement area and the plate thickness.

6. Conclusions and recommendations

6.1 Conclusions

If a fire breaks out in an immersed tunnel, its walls and roof will warm up as well. Since the thermal conductivity of concrete is very low (and tunnel walls are relatively thick), the heated side of a tunnel wall can easily reach temperatures well in excess of 700 ºC, while the unheated side can still be 20 or 30 ºC. This thermal gradient over the thickness causes a very large difference in thermal expansion, which can only be accommodated by the inwards bending of the walls and roof, which would lead to cracks on the unheated side. In this master's thesis, a finite element simulation has been made to assess this risk.

Calculations using this finite element simulation show that cracking on the unheated side is a realistic phenomenon that may manifest itself during a fire in an immersed tunnel. Although certain simplifications have been made while modelling, a comparison with fire tests carried out at Efectis shows that the model has a good predictive value for the behaviour of these specimens. Although only a limited number of tests were performed, it seems reasonable to assume that the model also has a good predictive value for an actual size tunnel.

This means that serious crack widths on the unheated side will be reached during a fire, up to 1.8 mm after 40 minutes for an unprotected tunnel. As natural fires will typically have a longer duration, the resulting crack widths will evidently be even larger. In addition to a large crack in the roof adjacent to the middle wall, there will also be smaller cracks in the roof adjacent to the side wall (of the heated tube), and in the side wall just below the roof.

There are, in general, two ways of avoiding these cracks. Firstly, the crack initiation can be delayed by applying fire-resistant plates (which reduces the temperatures to which the concrete is exposed), or by increasing the tensile strength (although that is a less feasible option for actual tunnels). Secondly, one can accept that cracks will develop, but keep their size within acceptable limits, which can be achieved using reinforcement: similar to any other concrete construction, the size of cracks can be limited by increasing the reinforcement area on the side of the cracks. As this pertains to the unheated side, there are no temperature effects here.

However, the realisation that cracking may occur on the unheated side if this is not actively prevented is only a partial conclusion, as long as the question how damaging such a crack might be is not yet addressed. The structural integrity of the tunnel is not directly threatened by the occurrence of the cracks; even with crack widths as large as 1.8 mm the sag will be limited to 10 mm in the middle of the span, which is well within acceptable limits.

The durability of the heated region of the tunnel will be reduced during the crack, as the strength and stiffness of both the concrete and the reinforcing steel will decrease due to the high temperatures, and will not return upon cooling. However, this is a general risk associated with fire that has already been extensively described in other studies, and not a consequence of the cracks on the unheated side that are the focus of this master's thesis.

However, one particular structural aspect that is noticeably influenced by these cracks is the shear capacity at the location of the cracks. As cracks cannot transmit shear stresses, the shear capacity is reduced at the locations of the cracks, which coincide with the locations of the largest shear stresses. If shear reinforcement is applied this is not likely to become a problem, but it is important to keep the possibility of cracking on the unheated side in mind when designing shear reinforcement and chamfers in an immersed tunnel.

Beside this, it would seem that the main danger stemming from these cracks is a long-term one: the risk of corrosion of the reinforcement. How imminent this risk is, however, would be difficult to predict, as long as the cooling down phase is not analysed. The standard material models in DIANA do not facilitate the modelling of the cooling down phase, but with a user-supplied material model, this problem has been circumvented. The material model described in this master's thesis has therefore cleared the way to a proper modelling of the cooling down phase.

6.2 Recommendations

If the cooling down phase is added to the current material model, it would be possible to make an accurate prediction of the remaining crack width after a complete temperature cycle. As this is required to assess the risk of corrosion of the reinforcement, this seems the most logical next step. Since the user-supplied material model has been coded in such a way that it allow for this expansion, this can now be done with relative ease.

That is not to say that all prerequisite knowledge on concrete behaviour is present, because numerous assumptions and simplifications still have to be made in the absence of research on this topic. In particular, more research on the influence of a decreasing temperature on the stress-strain relation is needed, especially with respect to unloading, softening and biaxiality. In addition, data is needed on the behaviour of concrete heated to temperatures above 800 ºC, as well as to concrete cooling down after reaching such temperatures.

In addition to this, there is the problem that it is difficult to assess crack widths with a smeared cracking model, as the crack widths are spread out over a large area, due to which it is often unclear whether the the summated crack width should be understood to pertain to a single crack or to multiple parallel cracks. This was supposed to be analysed in a separate lattice model, but then the problem remains that some assumptions regarding crack behaviour will already have to made in DIANA, and whichever assumption is made here will determine the eventual outcome.

Integrating the lattice model in DIANA would have avoided this, but this turned out not to be possible within the continuity requirements that have to be observed between the time steps in DIANA. Using discrete crack elements to assess crack widths might be the best option in subsequent analyses, despite their obvious drawbacks: the crack shape and location have to be predefined, and using multiple parallel crack elements might lead to convergence problems.

It would also be worthwhile to investigate the shear stress at the crack locations in more detail. The decrease of shear capacity in a crack would have to be modelled to accurately predict the increase of shear stress in the remaining cross section. The influence of shear reinforcement and chamfer dimensions can then be analysed, while implementing the temperature influence on the shear reinforcement.

Another aspect that could be implemented into the model, if the cooling down phase is to be modelled, is the influence of the surrounding soil on the crack. When crack widths of nearly 2 mm are reached, it is possible that water and sand would fall into the crack, creating a resistance against closing. The magnitude of such a resistance might be difficult to predict, but could have an important bearing on the result. In addition, it might be worthwhile to assess the reduced water tightness of the tunnel roof due to cracks, but a different type of model would be required for that.

The material model itself can also always be expanded and refined. In particular, the current assumption of a Rankine yield contour with two independent axes is rather crude; a Drucker-Prager criterion would be more realistic at this point, preferably with a correct modelling of the Poisson's ratio, and the temperature influence thereupon, implemented. A proper modelling of the biaxiality of the load induced thermal strains (LITS) as investigated by Ehm (1985) would also improve the prediction of the deformations.

At the same time, it should be remembered that the convergence of the simulation is an important boundary condition, and the current model appears to have a good predictive value for the fire tests already. Therefore, from a theoretical viewpoint, it might be more sensible to first perform additional tests, to assess the validity of the current model on a larger variety of specimens, for example with thicker walls. It is important that the moisture content is kept identical between the different test specimens, and measured before the test.

A further test series should not be combined with tests on specimens with PP fibres, because the influence of these fibres cannot be modelled using the current material model. If one wants to investigate their workings further, a different kind of model would be required, that would explicitly take into account moisture content and flow. This is perhaps more easily done in a multi-scale approach than by integration in the current model design.

References

ANDERBERG, Y. & THELANDERSSON, S. (1976) *Stress and Deformation Characteristics of Concrete at High Temperatures - part 2: Experimental Investigation and Material Behaviour Model*. Lund, Lund Institute of Technology. Division of Structural Mechanics and Concrete Construction, bulletin 54

BATHE, K. (1996) *Finite Element Procedures*. Prentice-Hall, Upper Saddle River

BAŽANT, Z. *et al.* (2004) Temperature Effect on Concrete Creep Modeled by Microprestress-Solidification Theory. *J. Eng. Mech., A.S.C.E.*, 130 (6), 691-699

BAŽANT, Z. & CHERN, J. (1987) Stress-induced Thermal and Shrinkage Strains in Concrete. *J. Eng. Mech., A.S.C.E.*, 113 (10), 1493-1511

DÖRR, K. (1980) *Ein Beitrag zur Berechnung von Stahlbetonscheiben unter besonderer Berücksichtigung des Verbundverhaltens*. Darmstadt, Technischen Hochschule Darmstadt. Dissertation (in German)

EFECTIS (2007) Report 2007-Efectis-R0458 (in Dutch; confidential)

EHM, C. (1985) *Versuche zur Festigkeit und Verformung von Beton unter zweiaxialer Beanspruchung und hohen Temperaturen*. Braunschweig, Technische Universität Carolo-Wilhelmina. Dissertation (in German)

CEN (2004) *Eurocode 2: Design of Concrete Structures - part 1-2: General Rules - Structural Fire Design* (EN 1992-1-2). Brussels, European Committee for Standardization (CEN)

FEENSTRA, P. (1993) *Computational Aspects of Biaxial Stress in Plain and Reinforced Concrete*. Delft, Delft University Press. Doctoral thesis for TU Delft

FELLINGER, J. (2004) *Shear and Anchorage Behaviour of Fire Exposed Hollow Core Slabs*. Delft, Delft University Press. Doctoral thesis for TU Delft

FISCHER, R. (1967) *Über das Verhalten von Zementmörtel und Beton bei höheren Temperaturen*. Darmstadt, Technische Hochschule Darmstadt. Dissertation (in German)

HORDIJK, D. (1991) *Local Approach to Fatigue of Concrete*. Delft, Meinema. Doctoral thesis for TU Delft

JAMET, P. *et al.* (1984) Triaxial Behaviour of a Microconcrete - Complete Stress-Strain Curves for Confining Pressures Ranging from 0 to 100 MPa. *Proceedings of RILEM-CEB Symposium on Concrete under Multiaxial Conditions, INSA Toulouse, session 4, experimental results*, 1, 133-140

KHOURY, G. *et al.* (1985) Strains of Concrete during First Heating to 600ºC under Load. *Mag. Concr. Res.*, 37 (133), 195-215

KHOURY, G. *et al.* (1986) Strains of Concrete during First Cooling from 1-600ºC under Load. *Mag. Concr. Res.*, 38 (134), 3-12

KUPFER, H. & GERSTLE, K. (1973) Behavior of Concrete under Biaxial Stresses. *J. Eng. Mech. Div., A.S.C.E.*, 99 (4), 853-866

MALHOTRA, H. (1956) The Effect of Temperature on the Compressive Strength of Concrete. *Mag. Concr. Res.*, 23 (8), 85-94

SCHLANGEN, E. (1993) *Experimental and Numerical Analysis of Fracture Processes in Concrete*. Delft, Technische Universiteit Delft. Doctoral thesis

ROTS, J. (1988) *Computational Modeling of Concrete Fracture.* Delft, TU Delft. Doctoral thesis.

SCHLANGEN, E. & GARBOCZI, E. (1997) Fracture Simulations of Concrete using Lattice Models: Computational Aspects. *Eng. Fract. Mech.*, 57 (2/3), 319-332

SCHNEIDER, U. (1982) *Verhalten von Beton bei hohen Temperaturen / Behaviour of Concrete at High Temperatures*. Berlin/Munich, Wilhelm Ernst & Sohn. Deutscher Ausschuß für Stahlbeton, Heft 337 (in German and English)

SCHNEIDER, U. (1988) Concrete at High Temperatures - A General Review. *Fire Safety Journal*, 13, 55-68

THELANDERSSON, S. (1972) *Effect of High Temperatures on Tensile Strength of Concrete*. Lund, Lund Institute of Technology. Division of Structural Mechanics and Concrete Construction, bulletin 26. Reprinted from Nordisk Betong, 2, 1972.

TNO (2004) *Repareerbaarheid van afgezonken tunnels na blootstelling aan de RWS brandkromme*. Report 2004-CVB-R0362 (in Dutch)

TNO DIANA (2007) *DIANA Finite Element Analysis - User's Manual, release 9.2*. Multi-part HTML archive supplied with DIANA software.

ZHANG, B. (2007) The Effect of High Temperatures on the Fracture Energy of High-Performance *Concrete*, 41 (1), 36-37

ZIENKIEWICZ, O. & TAYLOR, R. (1989) *The Finite Element Method, Vol. 1 - Basic Formulation and Linear Problems*. London, McGraw-Hill

ZIENKIEWICZ, O. & TAYLOR, R. (1991) *The Finite Element Method, Vol. 2 - Solid and Fluid Mechanics, Dynamics and Non-linearity*. London, McGraw-Hill

Summary

If a fire breaks out in an immersed tunnel, its walls and roof will warm up as well. Like most materials, concrete expands upon heating (until it reaches temperatures over 700 ºC). However, since the thermal conductivity of concrete is very low (and tunnel walls are relatively thick), the heated side of a tunnel wall can easily reach temperatures well in excess of 700 ºC, while the unheated side can still be 20 or 30 ºC.

This thermal gradient over the thickness causes a very large difference in thermal expansion, which can only be accommodated by the bending of the walls and roof (inwards, so that the heated side can elongate more than the unheated side). This, however, presents a problem for the corners of the structure, which cannot possibly accommodate the inward bending of both walls and roof. The consequence of this is that cracks will develop here, from the unheated side, in case of a fire.

This is potentially very dangerous, because such a crack can be neither seen nor repaired when assessing damage from the inside of the tunnel. It is possible that tunnels are declared to be 'repaired' after a fire, while in fact a crack remains open on the unheated side, causing slow corrosion of the reinforcement. In order to check whether this is actually the case, and if so, to what extent, a computer simulation has been created in the finite element program DIANA.

However, because the standard material models in DIANA do not facilitate the modelling of hysteresial effects with respect to temperature, a user-supplied material model has been created, which computes the stress vector based on a strain vector. However, this also means that several simplifications had to be made, especially with respect to the biaxial aspects of concrete behaviour. A simple Rankine yield criterion was used instead, the influence of the Poisson's ratio was ignored, and the load induced thermal strain (LITS) was applied as if it were a uniaxial effect.

The results of the simulation show that cracking on the unheated side is a realistic phenomenon, that may manifest itself during a fire. This can be avoided by applying fire-resistant plates or improving the tensile strength, both of which delay the crack initiation, or by increasing the reinforcement cross sectional area on the unheated side. In the latter case one accepts that cracks will develop, but prevents them from widening beyond an acceptable level.

Fire tests on scaled tunnel specimens (1:10) were run at Efectis for comparison. To this extent, an adapted mesh was created to match the size and shape of the tunnel specimen. The results of the simulations with this mesh are in good correspondence to the results of the fire tests. Although only a limited number of simulations were performed, this suggests a good accuracy of the model.

The realisation that cracking may occur on the unheated side is only a partial conclusion, however, as long as the question how damaging such a crack might be is not yet addressed. The reduction of the shear capacity might pose a problem, and it would be advisable to take this into account when designing shear reinforcement and chamfers. Other than this, the structural integrity of the tunnel is not directly threatened by the appearance of the crack, so that the main danger is the long-term risk of corrosion of the reinforcement.

Although the material model has opened the way to a proper modelling of the cooling down phase in DIANA, the actual implementation of this phase is beyond the scope of this master's thesis, which means that the crack width after cooling down cannot be determined at present. A further expansion of the FEM simulation to include the cooling down phase is therefore the logical next step, so that an estimation can be made regarding the magnitude of this risk.

Appendix: USRMAT code

Below is the actual USRMAT code used in the simulations. Some programmer's comments (preceded by C . .) are included to facilitate later expansion of the model, but for an full explanation, please refer to chapter 2 of this thesis.

```
      SUBROUTINE USRMAT( EPS0, DEPS, NS, TIME0, DTIME, TEMP0,
     $                   DTEMP, ELEMEN, INTPT, COORD, SE, ITER,
     $                   USRMOD, USRVAL, NUV, USRSTA, NUS,
     $                   USRIND, NUI, SIG, STIFF )

c..   in    DBL eps0(ns)    Strain vector at start of step
c..   in    DBL deps(ns)    Total strain increment
c..   in    INT ns          Number of stress components
c..   in    DBL age0        Age of element
c..   in    DBL dtime       Total time increment
c..   in    DBL temp0       Temperature
c..   in    DBL dtemp       Total temperature increment
c..   in    INT elemen      Current element number
c..   in    INT intpt       Current integration point number
c..   in    DBL coord(3)    Coordinates of integration point
c..   in    DBL se(ns,ns)   Elasticity matrix
c..   in    INT iter        Current iteration number
c..   in    CHA usrmod*6    User model name
c..   in    DBL usrval(nuv) User parameters
c..   in    INT nuv         Number of user parameters
c..   in/outDBL usrsta(nus) User state parameters
c..   in    INT nus         Number of user state parameters
c..   in/outINT usrind(nui) User indicators
c..   in    INT nui         Number of user indicators
c..   in/outDBL sig(ns)     Total stress
c..   in/outDBL stiff(ns,ns)Tangent stiffness

      PARAMETER         ( MTEMP = 20 )
      CHARACTER*6       USRMOD
      INTEGER           NS, NUV, NUS, NUI, ELEMEN, INTPT, ITER
      DOUBLE PRECISION EPS0(NS), DEPS(NS), TIME0, DTIME, TEMP0,
     $                  DTEMP, COORD(3), SE(NS,NS), USRVAL(NUV),
     $                  USRSTA(NUS), SIG(NS), STIFF(NS,NS)

      INTEGER           NTEMP, ELMIDX(2), I, XLOS, XELEM, MATNO,
     $                  NWSCHR, X, XRIJ
      LOGICAL           ISGESC
      DOUBLE PRECISION WC, C1, C2, PARFCT, TEMP(MTEMP), KT(MTEMP),
     $                  YOUNG, FCT20, EPS(NS), KTT, DUM, TE, FMAXT,
     $                  FPROPT, PARLEN, PARVAR, PHLEN, DHOR,
     $                  FHORT, EPROPT, EMAXT, EHORT, EULTT, W, ELLEN,
     $                  TEST(4), EPAR, KAPPA, S(2), E(2),
     $                  RDS, ES1, ES2, EE1, EE2, COSR, SINR, ETMP(3,7)
      DOUBLE PRECISION STMP(3,2), SIGTMP(2), EMAXC, FMAXC, EULTC,
     $                  EULTCA, FULTCA, LODLVL, FCC20, KC(MTEMP), KCT,
     $                  GFC, ESOFC, FSOFC, SOFYNG, VORSIG(2), EPST0(3),
     $                  DEPST(3), EPST1(3), EPSLIN, ALFAT, EPSLTS(3),
     $                  ALFA(MTEMP)
```

```
      DOUBLE PRECISION FSM20, FSP20, YNGS20, KFSM(MTEMP), KFSP(MTEMP),
     $                 KYNG(MTEMP), ALFS(MTEMP), KFSMT, KFSPT, KYNGT,
     $                 ALFAST, FMAXS, FPROPS, YOUNGS, EMAXS, EPROPS,
     $                 FUNCA, FUNCB, FUNCC, DEPSTS, EPST0S, EPST1S,
     $                 EPSABS, KLITS


      IF (USRMOD .EQ. 'STEEL') THEN

C..   ------------------------------------------------------------------
C..   -------------------------- REINFORCING STEEL ---------------------
C..   ------------------------------------------------------------------

      XLOS = 4
      XRIJ = 5
      FSM20    = USRVAL(1)
      FSP20    = USRVAL(2)
      YNGS20   = USRVAL(3)
      EMAXS    = USRVAL(4)

      NTEMP = (NUV - XLOS) / XRIJ
      IF (NTEMP .GT. MTEMP) CALL PRGERR ('MTEMP', 1)
      do 5, I=1, NTEMP
           TEMP(I) = USRVAL( XLOS + (I-1)*XRIJ + 1 )
           KFSM(I) = USRVAL( XLOS + (I-1)*XRIJ + 2 )
           KFSP(I) = USRVAL( XLOS + (I-1)*XRIJ + 3 )
           KYNG(I) = USRVAL( XLOS + (I-1)*XRIJ + 4 )
           ALFS(I) = USRVAL( XLOS + (I-1)*XRIJ + 5 )
 5    continue

      ELMIDX(1) = ELEMEN
      ELMIDX(2) = INTPT
      TE = TEMP0 + DTEMP

      IF (NUS .NE. 1) CALL PRGERR('NUS', 61)

C..   Calculate thermal strain

      CALL INTER1( TE, TEMP, ALFS, NTEMP, ALFAST, DUM )
      DEPSTS = ALFAST * DTEMP
      EPST0S = USRSTA(1)
      EPST1S = EPST0S + DEPSTS
      USRSTA(1) = EPST1S

      IF (NS .NE. 1) CALL PRGERR('USRMAT', 61)

      EPS(1) = EPS0(1) + DEPS(1) - EPST1S

      CALL INTER1( TE, TEMP, KFSM, NTEMP, KFSMT, DUM )
      CALL INTER1( TE, TEMP, KFSP, NTEMP, KFSPT, DUM )
      CALL INTER1( TE, TEMP, KYNG, NTEMP, KYNGT, DUM )

      FMAXS = FSM20 * KFSMT
      FPROPS = FSP20 * KFSPT
      YOUNGS = YNGS20 * KYNGT

      EPROPS = FPROPS / YOUNGS
```

```
      FUNCC = (FMAXS - FPROPS)**2 /
     $        ( (EMAXS - EPROPS)*YOUNGS - 2*(FMAXS - FPROPS) )
      FUNCB = sqrt( FUNCC * (EMAXS - EPROPS)*YOUNGS + FUNCC**2 )
      FUNCA = sqrt( (EMAXS - EPROPS) * (EMAXS - EPROPS + C / YOUNGS ) )

      EPSABS = ABS(EPS(1))

      IF (EPSABS .LT. EPROPS) THEN
           SIG(1) = EPSABS * YOUNGS
           STIFF(1,1) = YOUNGS
      ELSE IF (EPS(1) .LT. EMAXS) THEN
           SIG(1) = FPROPS - FUNCC + (FUNCB / FUNCA) *
     $              SQRT(FUNCA**2 - (EMAXS - EPSABS)**2)
           STIFF(1,1) = FUNCB * (EMAXS - EPSABS) /
     $                  ( FUNCA*SQRT(FUNCA**2 - (EPSABS - EMAXS)**2) )
      ELSE
           SIG(1) = FMAXS - 1.E-12 * (EPSABS - EMAXS)
           STIFF(1,1) = -1.E-12
      END IF

      IF (EPS(1) .LT. 0.D0) SIG(1) = -SIG(1)

C..   ------------------------------------------------------------------
C..   -------------------  CONCRETE  ---------------------------------
C..   ------------------------------------------------------------------


      ELSE IF (USRMOD .EQ. 'CONC') THEN

      XLOS = 8
      XRIJ = 4
      FCT20    = USRVAL(1)
      FCC20    = USRVAL(2)
      C1       = USRVAL(3)
      C2       = USRVAL(4)
      WC       = USRVAL(5)
      PARFCT   = USRVAL(6)
      GFC      = USRVAL(7)
      KLITS    = USRVAL(8)

      NTEMP = (NUV - XLOS) / XRIJ
      IF (NTEMP .GT. MTEMP) CALL PRGERR ('MTEMP', 1)
      do 19, I=1, NTEMP
           TEMP(I) = USRVAL( XLOS + (I-1)*XRIJ + 1 )
           KC(I) = USRVAL( XLOS + (I-1)*XRIJ + 2 )
           KT(I) = USRVAL( XLOS + (I-1)*XRIJ + 3 )
           ALFA(I) = USRVAL( XLOS + (I-1)*XRIJ + 4 )
 19    continue

      ELMIDX(1) = ELEMEN
      ELMIDX(2) = INTPT
      TE = TEMP0 + DTEMP

      IF (NUS .NE. 4) CALL PRGERR('NUS', 1)
```

```
C..   Determine thermal strain (incl. LITS)

      CALL INTER1( TE, TEMP, ALFA, NTEMP, ALFAT, DUM )
      EPSLIN = ALFAT * DTEMP
      DO 3, X=1, 2
           EPST0(X) = USRSTA(X)
           IF (SIG(X) .LT. 0.D0 .AND. DTEMP .GT. 0.D0) THEN
                EPSLTS(X) = KLITS * SIG(X) / FCC20 * ALFAT * DTEMP
           ELSE
                EPSLTS(X) = 0
           END IF
           DEPST(X) = EPSLIN + EPSLTS(X)
3     CONTINUE
      EPST1 = EPST0 + DEPST

      DO 4, X=1, 3
           USRSTA(X) = EPST1(X)
4     CONTINUE

      XELEM = INQ('/ELEMEN','DIM')
      CALL GTXC('/ELEMEN/HCRAC', ELMIDX(1), ELLEN, 1)

      IF (NS .NE. 3) CALL PRGERR('USRMAT', 1)

      EPS = EPS0 + DEPS - EPST1

      EE1 = EPS(2) + EPS(1)
      EE2 = EPS(2) - EPS(1)
      RDS = SQRT(EE2**2+EPS(3)**2)
      E(1) = 0.5 * (EE1 + RDS)
      E(2) = 0.5 * (EE1 - RDS)
      IF (RDS .EQ. 0) THEN
           COSR = 1.
           SINR = 0.
      ELSE
           COSR = EE2 / RDS
           SINR = EPS(3) / RDS
      END IF

c..   Calculate derivatives
      ETMP(1,1) = 1
      ETMP(1,2) = -1
      ETMP(2,1) = 1
      ETMP(2,2) = 1
      IF (RDS .NE. 0) THEN
           ETMP(1,3) = ( 2*EPS(1) - EPS(2) ) / (2 * RDS)
           ETMP(2,3) = ( 2*EPS(2) - EPS(1) ) / (2 * RDS)
           ETMP(3,3) = EPS(3) / RDS
      END IF

DO 10, X=1, 3
           ETMP(X,4) = 0.5 * (ETMP(X,1) + ETMP(X,3))
           ETMP(X,5) = 0.5 * (ETMP(X,1) - ETMP(X,3))
           IF (RDS .NE. 0) THEN
                ETMP(X,6) = (ETMP(X,2)*RDS - ETMP(X,3)*EE2) / (RDS**2)
                ETMP(X,7) = -ETMP(X,3)*EPS(3) / (RDS**2)
                ETMP(3,7) = (RDS - ETMP(X,3)*EPS(3)) / (RDS**2)
           END IF
10    CONTINUE
```

```
      VORSIG(1) = 0.5*(SIG(2) + SIG(1) + RDS)
      VORSIG(2) = 0.5*(SIG(2) + SIG(1) - RDS)

      DO 11, X=1, 2

C..         Calculate load level from stresses of the previous step
            IF (VORSIG(X) .GE. 0.D0) THEN
                 LODLVL = 0
            ELSE
                 LODLVL = - VORSIG(X) / FCC20
            END IF
            IF (LODLVL .GT. 0.3) LODLVL = 0.3

            EMAXC = - ( 2.2D0 + TE/140.D0 - TE/100.D0 * LODLVL**0.3 )
     $              * 1.D-3
            CALL INTER1( TE, TEMP, KC, NTEMP, KCT, DUM )
            FMAXC = - FCC20 * KCT

            YOUNG = 2 * FMAXC / EMAXC

            EULTC = 2 * GFC / (FMAXC * ELLEN) + EMAXC
c..         SOFYNG is calculated from FMAXC instead of FSOFC to avoid the need
c..         for iteration
            SOFYNG = - FMAXC / (EULTC - EMAXC)

            ESOFC = EMAXC * (1 - SOFYNG / YOUNG)
            FSOFC = FMAXC * (1 - (SOFYNG / YOUNG)**2)

            EULTCA = -FSOFC / SOFYNG + ESOFC
            FULTCA = SOFYNG * (EULTCA - ESOFC) + FSOFC

            CALL INTER1( TE, TEMP, KT, NTEMP, KTT, DUM )
            FMAXT = FCT20 * KTT
            FPROPT = (1 - PARFCT) * FMAXT
            EPROPT = FPROPT / YOUNG

c..   DHOR is the derivative of the Hordijk curve at w = 0 (calculated from
c..   FMAXT instead of FHORT to avoid iterating). The parabola y=ax^2 (with top
c..   at EMAXT) is characterized by a single parameter a = PARVAR. The length of
c..   the parabola on the left side of the top (hardening) equals PARLEN, the
c..   length of on the right side of the top equals PHLEN. The lengths are
c..   determined from the requirement that the derivatives equal YOUNG and DHOR
c..   respectively, and the height at the start of the parabola equals
c..   PARFCT * FMAXT.

            DHOR = (-1 * C2 -1*(1+C1**3) * EXP(-1*C2)) * FMAXT/(WC/ELLEN)
            PARLEN = 2 * PARFCT * FMAXT / YOUNG
            PARVAR = -1 * YOUNG**2 / (4 * PARFCT * FMAXT)
            PHLEN = -2 * PARFCT * FMAXT * DHOR / (YOUNG**2)


            EMAXT = EPROPT + PARLEN
            FHORT = FMAXT - PARFCT * FMAXT * DHOR**2 / (YOUNG**2)
            EHORT = EMAXT + PHLEN
            EULTT = EHORT + WC / ELLEN
```

```
      w = 0
      IF (E(X) .LT. EULTCA) THEN
           S(X) = - 1.E-12 * (E(X) - EULTC)
           SIGTMP(X) = -1.E-12
      ELSE IF (E(X) .LT. ESOFC) THEN
           S(X) = SOFYNG * (E(X) - ESOFC) + FSOFC
           SIGTMP(X) = SOFYNG
      ELSE IF (E(X) .LT. 0.D0) THEN
           S(X) = FMAXC * E(X) / EMAXC * ( 2 - E(X) / EMAXC )
           SIGTMP(X) = 2 * FMAXC / EMAXC * (1 - E(X) / EMAXC)
      ELSE IF (E(X) .LT. EPROPT) THEN
           S(X) = E(X) * YOUNG
           SIGTMP(X) = YOUNG
      ELSE IF (E(X) .LT. EHORT) THEN
           EPAR = E(X) - EMAXT
           S(X) = FMAXT + PARVAR * EPAR**2
           SIGTMP(X) = 2 * PARVAR * EPAR
     ELSE IF (E(X) .LT. EULTT) THEN
           W = (E(X) - EHORT) * ELLEN
           S(X)=( (1+(C1*W/WC)**3)*EXP(-1*C2*W/WC)-
$                W/WC*(1+C1**3)*EXP(-1*C2) ) * FHORT
           SIGTMP(X)=(((3-C2*W/WC)*C1**3*(W/WC)**2-C2)
$               *EXP(-1*C2*W/WC)-(1+C1**3)*EXP(-1*C2)) * FHORT/WC
      ELSE
           S(X) = 1. - 1.E-12 * (E(X) - EULTT)
           SIGTMP(X) = - 1.E-12
      END IF

      IF (S(X) .EQ. 0.D0 .AND. E(X) .NE. 0.D0) THEN
           CALL PRGERR('USRMAT', 11)
      END IF

      IF (X .EQ. 1) USRSTA(4) = W
11    CONTINUE

      ES1 = 0.5 * (S(1) + S(2))
      ES2 = 0.5 * (S(1) - S(2))
      SIG(1) = ES1 - ES2 * COSR
      SIG(2) = ES1 + ES2 * COSR
      SIG(3) = ES2 * SINR

      do 12, X=1, 3
         STMP(X,1) = 0.5 * (SIGTMP(1)*ETMP(X,4) + SIGTMP(2)*ETMP(X,5))
         STMP(X,2) = 0.5 * (SIGTMP(1)*ETMP(X,4) - SIGTMP(2)*ETMP(X,5))
12    CONTINUE

      do 13, X=1, 3
           STIFF(1,X) = STMP(X,1) - STMP(X,2)*COSR - ETMP(X,6)*ES2
           STIFF(2,X) = STMP(X,1) + STMP(X,2)*COSR + ETMP(X,6)*ES2
           STIFF(3,X) = STMP(X,2)*SINR + ETMP(X,7)*ES2
13    CONTINUE

      END IF
      RETURN
      END
```

In the DIANA data file (*.dat), the user-supplied material model can then be invoked by adding the following code. The values shown here are, of course, an example.

```
     USRMAT   STEEL
     USRVAL   500.E6 300.E6 2.1E11 0.02
:              TEMP      KfMAX   KfPROP  KYNG    ALPHA
              -2000.     1.      1.      1.      1.2216E-5
                 20.     1.      1.      1.      1.2216E-5
                100.     1.      1.      1.      1.280E-5
                200.     1.      0.81    0.90    1.36E-5
                300.     1.      0.61    0.80    1.44E-5
                400.     1.      0.42    0.70    1.52E-5
                500.     0.78    0.36    0.60    1.60E-5
                600.     0.47    0.18    0.31    1.68E-5
                700.     0.23    0.07    0.13    1.76E-5
                749.     0.17    0.06    0.11    1.799E-5
                750.     0.17    0.06    0.11    0.
                800.     0.11    0.05    0.09    0.
                860.     0.085   0.045   0.08    0.
                861.     0.085   0.045   0.08    2.E-5
                900.     0.06    0.04    0.07    2.E-5
               1000.     0.04    0.02    0.04    2.E-5
               1100.     0.02    0.01    0.02    2.E-5
               2000.     1.E-12  1.E-12  1.E-12  2.E-5
     USRIND
     USRSTA   0.
```

Or, for concrete:

```
     USRMAT   CONC
     USRVAL   2.E6 35.E6 3. 6.93 160.E-4 0.1 1.e50 2.
:              TEMP    KC      KT      ALPHA
              -2000.   1.      1.      9.E-6
               20.     1.      1.      9.E-6
               100.    1.      1.      9.08E-6
               200.    0.8     0.8     9.31E-6
               300.    0.6     0.6     9.69E-6
               400.    0.4     0.4     1.02E-5
               500.    0.2     0.2     1.09E-5
               600.    0.15    0.15    1.18E-5
               700.    0.1     0.1     1.28E-5
               701.    0.1     0.1     0.
               800.    0.05    0.05    0.
               900.    0.04    0.04    0.
               1000.   0.02    0.02    0.
               1100.   0.01    0.01    0.
               2000.   1.E-12  1.E-12  0.
     USRIND
     USRSTA   0. 0. 0. 0.
```